

POLITECNICO
MILANO 1863

SCUOLA DI INGEGNERIA INDUSTRIALE
E DELL'INFORMAZIONE

Experimental and Computational Aerodynamics of Lilienthal's *Rundlaufapparat*

Master of Science Thesis in
Aeronautical Engineering – Ingegneria Aeronautica

Author: **Andrea Massinari**

Student ID: **249731**
Advisor: **Prof. Alex Zanotti**
Co-advisors: **Dr. Anthony D. Gardner**
Prof. Markus Raffel

Academic Year: **2024–2025**

Abstract

Otto Lilienthal's contribution to the history of aerodynamics and flight is well established, yet the experimental foundation of his aerodynamic work remains less systematically investigated than his glider achievements. Beyond his pioneering glides, Lilienthal performed systematic rotating-arm experiments using the *Rundlaufapparat*, producing quantitative results that foreshadowed modern aerodynamic practice. This project reconstructs and operates a faithful *Rundlaufapparat*, formalizes the measurement chain converting timings, masses, and readings from the counterbalanced lever into lift and drag, and makes explicit the reduction from forces to coefficients to clarify Lilienthal's methodology. Historical experiments are reproduced to reconstruct Lilienthal's Plates, published tables interpretable as early aerodynamic polars, and the resulting data are analyzed to assess how normalization choices and contemporary theory shaped the reported magnitudes and trends. Rotating-arm measurements are compared with tests in DLR's RTG open-jet wind tunnel and with two- and three-dimensional Reynolds-averaged Navier–Stokes (RANS) simulations under matched conditions. Findings show that the apparatus robustly resolves aerodynamic forces and captures trends, while systematic differences in coefficient magnitudes arise from normalization schemes, ranging from the Smeaton coefficient to normalization by the measured force at $\alpha = 90°$, and from kinematic differences between curved, accelerating *Rundlaufapparat* motion and rectilinear inflow in wind-tunnel and simulation setups. This study clarifies what Lilienthal's Plates represent in modern terms, explains coefficients derivation and alternative formulations, identifies regimes of highest reliability, contrasts historical reductions with contemporary techniques, and establishes a reproducible basis for future rotating-arm aerodynamics.

Keywords: Otto Lilienthal, Whirling-arm apparatus, Aerodynamic coefficients, Wind-tunnel testing, CFD

Abstract in lingua italiana

Il contributo di Otto Lilienthal alla storia dell'aerodinamica e del volo è ampiamente riconosciuto, eppure la base sperimentale del suo lavoro aerodinamico rimane indagata in modo meno sistematico rispetto ai suoi risultati con gli alianti. Oltre ai suoi voli planati pionieristici, Lilienthal condusse esperimenti sistematici con braccio rotante utilizzando il *Rundlaufapparat*, ottenendo risultati quantitativi che anticiparono la pratica aerodinamica moderna. Questo progetto ricostruisce e mette in opera una riproduzione fedele del *Rundlaufapparat*, formalizza la catena di misura che converte tempi, masse e letture della bilancia a leva in portanza e resistenza e rende esplicita la riduzione dalle forze ai coefficienti per chiarire la metodologia di Lilienthal. Gli esperimenti storici sono riprodotti per ricostruire le Tavole di Lilienthal, tabelle pubblicate interpretabili come prime polari aerodinamiche, e i dati risultanti sono analizzati per valutare come le scelte di normalizzazione e la teoria dell'epoca abbiano influenzato le magnitudini e le tendenze riportate. Le misure al braccio rotante vengono confrontate con prove nella galleria del vento a getto libero RTG del DLR e con simulazioni Reynolds-averaged Navier–Stokes (RANS) bidimensionali e tridimensionali in condizioni corrispondenti. I risultati mostrano che l'apparato risolve in modo robusto le forze aerodinamiche e cattura le tendenze, mentre differenze sistematiche nei valori dei coefficienti derivano da schemi di normalizzazione, dal coefficiente di Smeaton fino alla normalizzazione mediante la forza misurata a $\alpha = 90°$, e da differenze cinematiche tra il moto curvilineo e accelerato del *Rundlaufapparat* e l'afflusso rettilineo nelle configurazioni di galleria del vento e di simulazione. Questo studio chiarisce che cosa rappresentano le Tavole di Lilienthal in termini moderni, spiega la derivazione dei coefficienti e quali formulazioni alternative possano essere state impiegate, identifica i regimi di massima affidabilità, confronta le riduzioni storiche con le tecniche contemporanee e stabilisce una base riproducibile per la futura aerodinamica a braccio rotante.

Parole chiave: Otto Lilienthal, Apparato a braccio rotante, Coefficienti aerodinamici, Prove in galleria del vento, CFD

Contents

Abstract **i**

Abstract in lingua italiana **iii**

Contents **v**

1 Introduction **1**

2 History and Theory: From Lilienthal to Modern Aerodynamics **5**
2.1 The life of Otto Lilienthal 5
2.2 Experiments and inventions 7
2.3 The *Rundlaufapparat* 11
2.4 The evolution of flight after Lilienthal 13
2.5 Aerodynamic theory 13

3 Apparatus Design and Reconstruction **21**
3.1 Structure 22
3.2 Central drum 23
3.3 Pulleys 26
3.4 Arms 27
3.5 Wings 29
3.6 Counterbalanced lever and lift balance 31

4 Methods: Lilienthal Measurement Model **35**
4.1 Kinematics: speed from turn time 36
4.2 Lilienthal's wing drag derivation 37
4.3 Lilienthal's drag derivation with friction 41
4.4 Lilienthal's lift derivation 43
4.5 Coefficient definitions and computation 44
4.6 Alternative empirical formula from the notes 45

5 Experimental Tests and Results: *Rundlaufapparat* **47**
5.1 Kinematics and velocity characterization 47
5.2 Lilienthal measurements 61
5.3 Kinematic model application 78

6 Wind-Tunnel Tests **83**
6.1 Airfoil and wing design 83
6.2 Wind-tunnel setup 86
6.3 Wind-tunnel experiments 88
6.4 Wind-tunnel results 89

7 CFD Simulations of the *Rundlaufapparat* Wings **93**
7.1 Objectives and scope 93
7.2 Governing equations and turbulence closures 93
7.3 Numerical setup 95
7.4 3D simulations 109
7.5 Comparison with *Rundlaufapparat* results 112
7.6 Global comparison of lift-drag polars 114

8 Conclusions **115**

Bibliography **119**

A CAD Drawings **125**

B Algorithm **129**

C Geometry and Data **131**

D Simulation Code **133**

List of Figures **135**

List of Tables **139**

List of Symbols **141**

1 | Introduction

Otto Lilienthal was a pioneer of "heavier than air" flight and of experimental aerodynamics. Working before a complete aerodynamic theory existed, he combined systematic measurements on curved fabric wings with full-scale gliding, and compiled his results in the Plates of *Birdflight as the Basis of Aviation* [1, 2]. His public flights reached distances up to about 250 m, and widely circulated photographs gave his work extraordinary visibility and impact beyond Germany [3]. His results influenced the trajectory of early aviation and provided data that later experimenters and engineers used for comparison. How Lilienthal converted raw timings and masses into lift and drag, and then reduced those forces to coefficients, remains unclear and complicates comparisons with modern data. This study reconstructs a faithful whirling-arm apparatus and its measurement chain, re-derives the force and coefficient reductions, and tests alternative normalizations against new whirling-arm measurements, wind-tunnel data, and Reynolds-averaged Navier–Stokes (RANS) simulations to identify which reconciles best.

Lilienthal's measurements relied primarily on a rotating-arm apparatus, the *Rundlaufapparat*, which converted the action of falling masses into motion and allowed direct inference of lift and drag. Although an enclosed wind tunnel had been demonstrated by Wenham and Browning in 1871 [4], such facilities were uncommon during Lilienthal's working years; the best-known examples, the Wrights' 1901 tunnel [5] and Eiffel's 1909 open-jet facility [6] appeared after his death in 1896. Within this evolving tradition, from Cayley's whirling arm to early wind tunnels, Lilienthal refined rotating-arm testing and, together with complementary wind-apparatus experiments, produced data that can be read today as early aerodynamic polars [7].

Despite its historical value, the 19th-century reduction framework requires reinterpretation, and the exact reduction steps that Lilienthal applied remain a matter of debate. Given the state of theory and knowledge at the time, it was common to use the Smeaton coefficient rather than modern dynamic-pressure normalization, and it is plausible that Lilienthal followed this approach for his reductions. The historical and modern literature also documents an alternative normalization that takes the measured force at $\alpha = 90°$

as the reference, rather than an empirical formula through the Smeaton coefficient [8]. Recognizing this context is essential to understand both the limitations of the measurements and the choices made. Rotating-arm tests introduced finite-radius and wake interaction effects, and the measurements preceded the systematic use of Reynolds number scaling. Taken together, these factors help explain why Lilienthal's data captured relative trends and lift-to-drag ratios accurately, while remaining systematically different in magnitude from modern coefficients.

This thesis examines the actual work of Lilienthal with the *Rundlaufapparat*. Starting from a reproduction of the apparatus, the objectives are to establish the kinematics of the whirling-arm experiments, to clarify Lilienthal's method and the way results were treated, and to reproduce his tests in order to reconstruct his Plates. On this basis, the study evaluates whether the assumptions and methods are appropriate for the conditions considered, and to what extent the resulting coefficients agree with modern definitions. Wind-tunnel tests and computational fluid dynamics (CFD) simulations are used alongside the whirling-arm tests to assess the historical procedures under controlled conditions.

Chapter 2 reviews the historical and theoretical background relevant to Lilienthal's measurements. This context is essential to understand how advanced aerodynamic knowledge was at the time and to interpret the choices and methods applied by Lilienthal. The scaling of aerodynamic forces with the square of velocity ($L, D \propto V^2$) was known and formed a foundation for experimental practice. By contrast, the modern theory of aerodynamic coefficients, how forces develop around a surface in a flow, and other theoretical concepts were not yet established. Accordingly, an important part of the study examines the Smeaton coefficient, its historical values, and how these alternatives will be used to infer Lilienthal's procedure and results.

The reconstruction of the *Rundlaufapparat* is described in Chapter 3. At the Institute of Aerodynamics and Flow Technology at DLR in Göttingen, the apparatus is reproduced from Lilienthal's notes and drawings. Where dimensions or parts were not explicitly stated, they are inferred from the drawings and chosen to achieve functional equivalence. Any changes to the original dimensions are documented together with their expected influence on the tests and possible adjustments for future work. The chapter details the components required to operate the *Rundlaufapparat*: the overall structure, the rotating system composed of the central drum, pulleys, and a vertical shaft, the arms, the wings, and the counterbalanced lever, with the goal of establishing the kinematics and the measurement chain.

Once the apparatus is reproduced as intended, Chapter 4 derives the method adopted

by Lilienthal to obtain forces and coefficients from the measurements. Starting from torque balances and friction assumptions, consistent with the apparatus kinematics and calculations preserved in his notes, alternative drag formulations are developed and used to process the experimental data. For lift, a governing relation is obtained, and the counterbalanced lever is analyzed to clarify possible sources of error in the force reading. This chapter also defines all alternative normalizations of the coefficients, from the Smeaton coefficient reduction (with its historical and modern values described in Ch. 2), to the use of the measured force at $\alpha = 90°$ as a reference, up to modern coefficient definitions based on dynamic pressure.

The results are then discussed in Chapter 5, together with the supporting analyses. First, the apparatus kinematics are established from velocity and drop-time histories measured for different applied loads m and wing incidences α. The analysis quantifies the duration of the acceleration phase and identifies the conditions under which a steady or quasi-steady phase can be reached, where the measurements achieve higher accuracy. On this basis, a MATLAB model of the apparatus kinematics is developed to simulate any (m, α) case, and it is verified against the measurements. Once the kinematics are established, Lilienthal's procedure is documented and replicated at DLR in Göttingen. Tests are performed first without wings, then with the wings installed. The results are processed using the formulations derived in the previous chapter to examine the alternative normalizations and to reconstruct Lilienthal's method, verifying it against the new data. Finally, the MATLAB model is applied to the test data to explore variations of the results and to reduce the influence of the acceleration phase on the measured forces.

In Chapter 6, the airfoil section and the wing model used for the wind-tunnel tests and the simulations are described. Starting from a Lilienthal drawing, both geometries are reconstructed in CATIA. A negative mold is 3D-printed in PLA, and from it a half-scale carbon-fiber model is produced and tested in the RTG, an open-jet wind tunnel at DLR in Göttingen. These tests provide a first modern assessment of Lilienthal's cambered, very thin wings under controlled conditions using current techniques.

The same geometry is adopted in the simulations, described in Chapter 7. RANS 2D and 3D simulations are performed to study the flow behavior in Lilienthal's conditions of Mach number Ma and Reynolds number Re. In addition, analyses of grid convergence, boundary-layer resolution, turbulence model, and velocity scaling (Ma, Re) are carried out to represent Lilienthal's conditions as faithfully as possible, while still yielding reliable results. These simulations not only improve understanding of the flow around Lilienthal's wing geometries, but also enable comparisons of coefficient values with both the historical rotating-arm tests and the wind-tunnel measurements. A kinematic difference between the

setups is noted: the rotating arm produces curved, accelerating motion along a circular path, whereas the wind tunnel and CFD impose a rectilinear, uniform inflow. Future high-fidelity options (LES/DES and direct modeling of the rotating apparatus) are outlined in the conclusions.

In Chapter 8, the conclusions are presented and future work is outlined.

In summary, the thesis reconstructs and operates the *Rundlaufapparat* to acquire new whirling-arm measurements, derives the force and coefficient reductions, and benchmarks the outcomes against wind-tunnel and RANS results. Together, these elements interpret Lilienthal's Plates in modern terms.

2 | History and Theory: From Lilienthal to Modern Aerodynamics

2.1. The life of Otto Lilienthal

Otto Lilienthal (1848–1896) was born on 23 May 1848 in Anklam, then in Prussia (now Germany). He grew up there with his younger brother Gustav; they shared a lifelong interest in observing birds in flight, especially storks. Guided by these observations, Otto tried to understand and recreate how birds fly [2].



Figure 2.1: Otto Lilienthal portrait, 1894. Photographer: A. Regis. Otto-Lilienthal-Museum Bildarchiv, Archiv-ID 18009 [9]

Lilienthal studied mechanical engineering at the *Gewerbe-Institut* in Berlin. He worked as

a designer, then founded a small engineering firm that produced steam engines, boilers, heaters, and other mechanical devices, financing his aeronautical experiments. Gustav, throughout his life, collaborated closely with his brother, helping with their experiments, and later also editing Otto's papers [3].

At the time, "heavier than air" flight was widely considered impossible. Balloons, "lighter than air", were the only proof that sustained flight was possible. Lilienthal set out to understand why birds fly with apparent ease. From the late 1860s he ran a systematic measurement program on curved, fabric-covered wings: first with rotating-arm apparatus in still air, then with a wind apparatus to study how lift increases in wind conditions. He compiled his results in Plates in *Der Vogelflug als Grundlage der Fliegekunst* (1889) [1], translated as *Birdflight as the Basis of Aviation* [2]. These Plates effectively anticipate modern lift–drag polars and made his work widely read beyond Germany [8, 10].

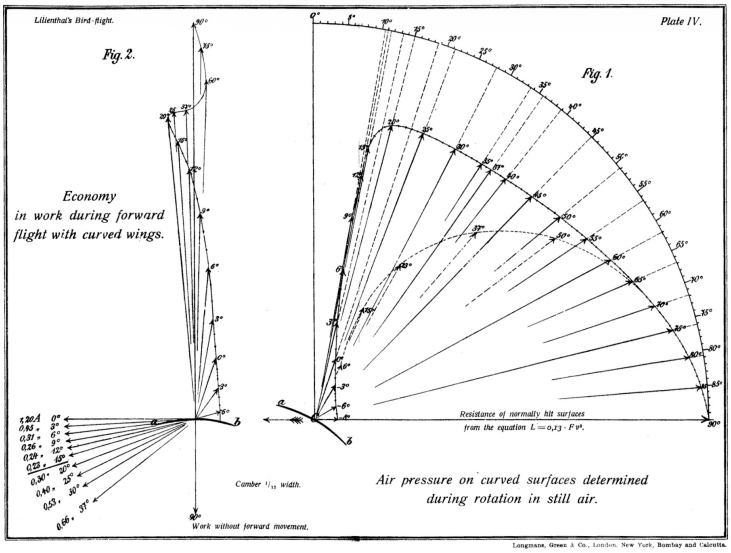

Figure 2.2: Lilienthal's Plate IV showing whirling-arm apparatus results [2, Pl. IV]

From 1891 onward, Lilienthal moved to gliding. His goal was to obtain controlled and stable flight, without falling. Early flights near Derwitz (Potsdam area) validated his curved-wing concepts. He soon built the artificial *Fliegeberg* (1894) in Berlin-Lichterfelde, and later flew extensively from the Rhinow Hills, specifically on Gollenberg near Stölln [3]. Photographs of the *Normalsegelapparat* and his biplane circulated internationally and convinced many contemporaries that controlled "heavier than air" flight was feasible [8, 11].



Figure 2.3: Otto Lilienthal in flight with the *Normalsegelapparat*, Fliegeberg (Berlin–Lichterfelde), 1894. Photo: Alex Krajewsky. Otto-Lilienthal-Museum Bildarchiv, Archiv-ID 12226 [9]

To sustain his research, he combined invention, manufacturing, and careful documentation. Surviving correspondence with contemporaries, preserved in the Otto-Lilienthal-Museum archive (including the Lilienthal–Platte letters), documents both technical debates and the skepticism he faced in Germany [12] (see also Heinzerling and Trischler [11]).

Lilienthal's career ended after a crash on 9 August 1896; he died the next day in Berlin from spinal injuries. His approach to measurement, his experimental and partly theoretical understanding of aerodynamics, developed before a complete theory existed, and his results became part of the culture of early aeronautics [8].

2.2. Experiments and inventions

Lilienthal was one of the first to understand complex aerodynamic concepts. His grasp of how air behaves around curved wings, relative to flat plates, how pressure changes, and how lift arises, was extremely advanced without a modern theory to support it. His sketches were an early form of streamline visualization and, although not perfect, they were remarkably accurate. They show how camber and angle of attack bend the flow, increase pressure on the lower side, and reduce it on the upper side, while also reducing the disturbance in the wake (what he called eddies, now known as vortices) [2].

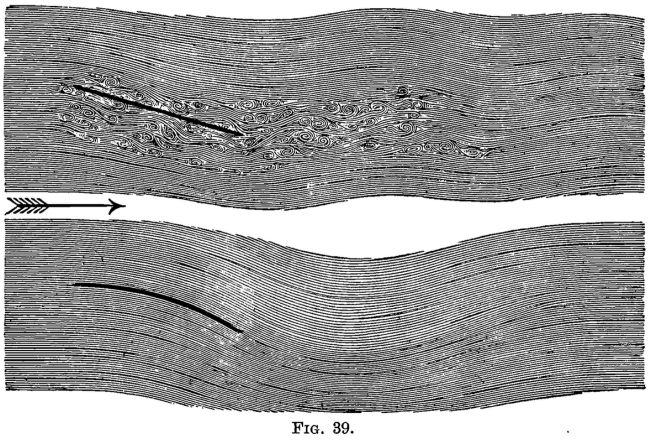

Figure 2.4: Streamline sketches around a flat plate and a curved surface [2, Fig. 39, Ch. 25]

2.2.1. Curved wings

During the 1870s and 1880s he focused on curved (cambered) fabric wings. He showed that curvature, together with incidence, greatly increases the *Tragfähigkeit* (carrying capacity) of a surface compared to a flat plate [13]. To prove and quantify this effect, he designed several devices for measuring what he called "air resistance" (lift and drag).

2.2.2. The *Rundlaufapparat* and wind apparatus

For reliable tests and data, Lilienthal built a rotating-arm apparatus, the *Rundlaufapparat*. In still air he tested model wings on a balance system with known masses, converting torque to lift and drag. He then compared those results with measurements in wind, using a modified setup to expose the same wings to a uniform flow. In the wind campaign he first analyzed the total effect due to the wind itself (Plate V [2]), then separated the aerodynamic contribution due to the wing's motion from any static support due to the wind, allowing a fair comparison with the data obtained in still air with the rotating apparatus (Plate VI [2]). From these experiments he derived his Plates.

Lilienthal understood that meaningful measurements required a steady, uniform flow over the wings. This is why modern experiments use wind tunnels. However, building a machine to provide true linear translation "would necessitate mechanism with greater secondary resistances, and consequently would introduce greater sources of error" [2, Ch.27]. For this reason, he used both devices and compared their results to compensate for the limitations of each: the disturbed flow inherent to the rotating-arm tests and the variability of the natural wind in the wind apparatus.

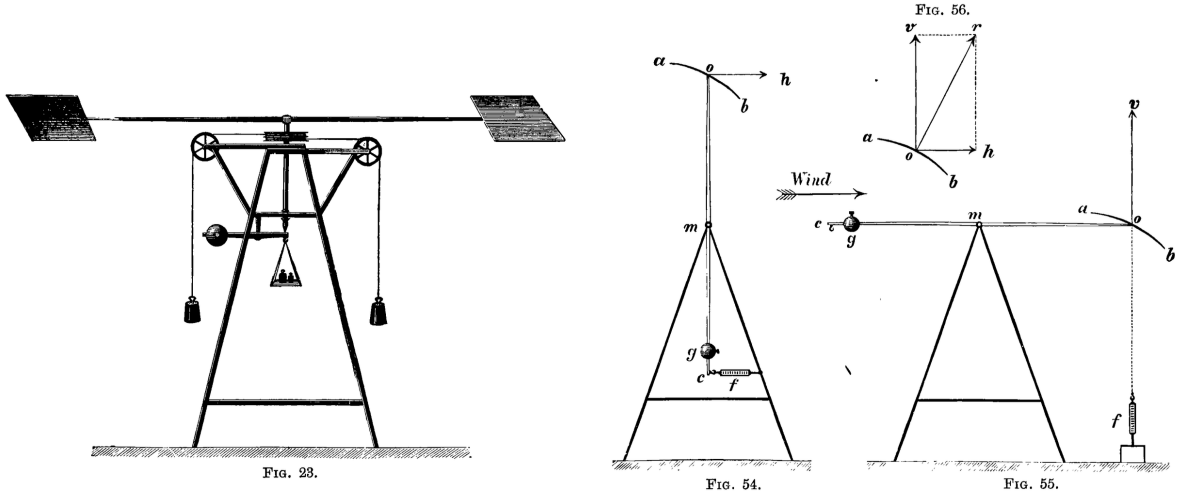

(a) Rotating-arm apparatus (b) Wind apparatus

Figure 2.5: *Rundlaufapparat* vs. wind apparatus used by Lilienthal to measure lift and drag [2, Fig. 23, Ch. 19; Figs. 54–56, Ch. 23]

In the wind measurements he also reported effects that were not entirely correct in hindsight. In his book, Lilienthal [2, Ch.33] discussed an increase in lifting effect due to wind and argued that stronger wind increases this effect. The rise of "air resistance" (drag and lift) with speed is correct, since aerodynamic forces scale with dynamic pressure, $L \propto V^2$ [14]. However, he also inferred an increase in the coefficients themselves, as can be seen in Plates V–VI [2]. Later authors noted that this likely came from an error in the Smeaton framework and its value considered generally accepted at the time, together with calibration choices, Reynolds-number variations and fabric-porosity effects [8, 15].

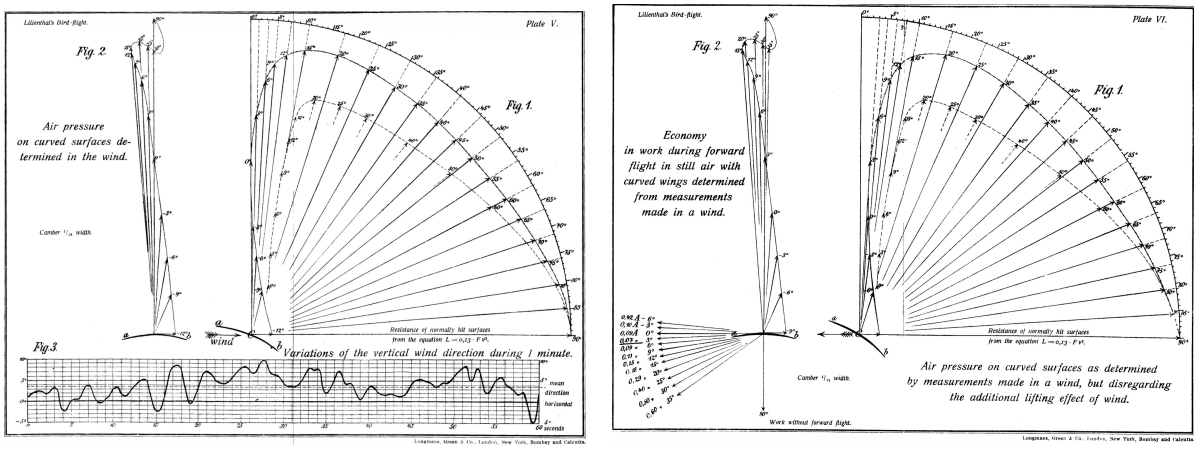

(a) Plate V (b) Plate VI

Figure 2.6: Lilienthal's Plates illustrating the wind effect [2, Pls. V–VI]

2.2.3. Gliders

Lilienthal, from 1891, built full-scale gliders, starting with the *Derwitzer*. He then developed the *Normalsegelapparat* (1893, the first serially produced aircraft), the *Sturmflügelapparat*, and a large biplane (1895). All were weight-shift gliders with cambered, fabric-covered wings; the frames were foldable to ease transport. With these he made thousands of flights and reached distances up to about 250 m, the longest of his era [3].

Quantitative assessments of flying qualities and control for these configurations are given by Raffel, Wienke, and Dillmann [16] for the Large Biplane, and by Raffel, Wienke, Schwarz, and Dillmann [17] for the 1895 experimental monoplane.

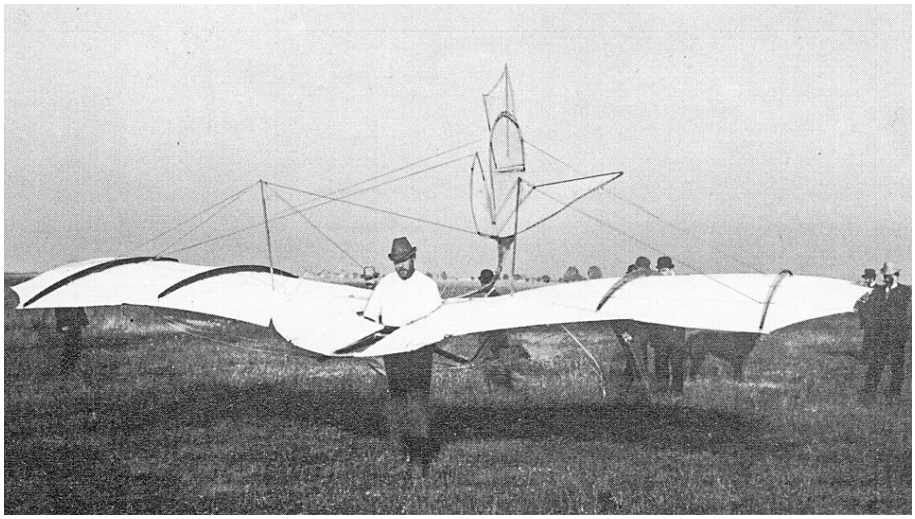

Figure 2.7: Otto Lilienthal with the *Normalsegelapparat*, 29 June 1895. Photo: Richard Neuhauss. Otto-Lilienthal-Museum Bildarchiv, Archiv-ID 12134 [9].

2.2.4. Other inventions

Beyond aeronautics, Lilienthal's workshop produced compact steam engines, water-tube boilers, and space heaters, which financed his flight experiments. His key boiler innovation was a serpentine water-tube boiler, a safety-oriented design with coiled tubes that increased heating surface while reducing stored water and explosion risk [9]. Together with Gustav he also developed a modular toy system of mineral building blocks that later became the *Anker* sets [9].

Lilienthal also explored power-aided gliding. He tested a propulsion system for his gliders with piston-driven flapping wingtips (an ornithopter concept) and integrated this idea into his experimental apparatus [18] (see also Raffel et al. [19]).

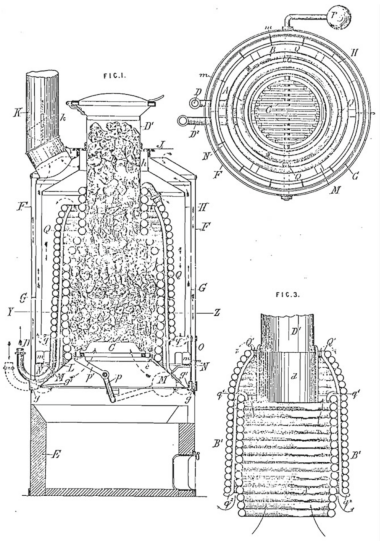

(a) Illustration of the coiled-tube (serpentine) boiler in the English patent granted to Lilienthal. *Otto, Bashall, William: An Improved Coil Steam Generator*, Brit. Patent No. 8322, June 23, 1886. Otto-Lilienthal-Museum. [9]

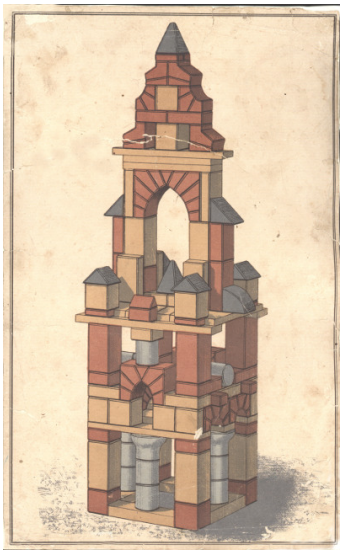

(b) *Stone Building Set, Plan No. 36* (1886). Otto-Lilienthal-Museum Image Archive, Archiv-ID 16276, OLM Inv.-No. 9545. [9]

Figure 2.8: Other inventions associated with Lilienthal's workshop

2.3. The *Rundlaufapparat*

The *Rundlaufapparat* (whirling-arm device) was built by Lilienthal in the 1870s and used for many years to test curved wings. His aim was to measure what he called "air resistance" (drag and lift); in his words, the apparatus "enabled us to determine not only the magnitude but also the direction of the pressures produced by rotating surfaces", Lilienthal [2, Ch.19]. With it he could compare flat and curved wings quantitatively, proving the aerodynamic superiority of the latter.

2.3.1. Operating principle

This apparatus consisted of a vertical shaft connected to two opposite light arms; at their tips, two test surfaces could be set to any inclination. The system was driven using falling weights connected through ropes and pulleys to a central drum (see Ch. 3). Tests were performed in still air, so the wing speed was $V = \omega R$.

From a torque balance, the horizontal component of force was inferred from the propelling weight after deducting the arm resistance and a frictional loss determined by empty runs; the vertical component was read with a counterbalanced lever, connected to the rotating

system, and allowed a small vertical travel [2]. As he noted, “we choose this arrangement in order to eliminate as far as possible the lateral pull on the bearings” [2]. The detailed mechanism and formulas are derived later in Chapter 4.

2.3.2. Layout

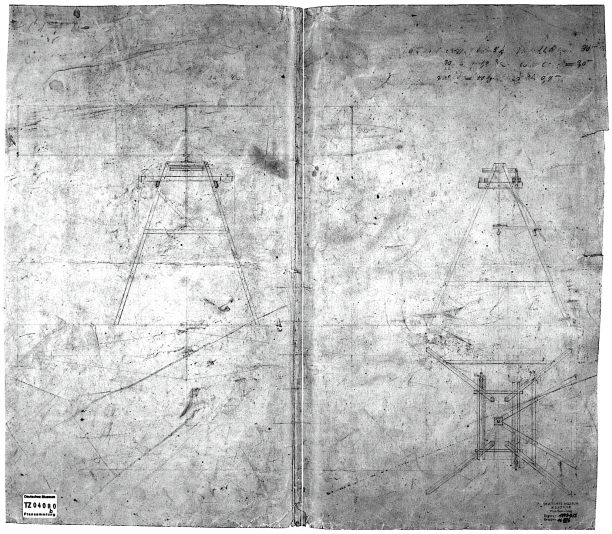

Figure 2.9: Drawing of the large *Rundlaufapparat* (diameter 7 m), 1888. Otto-Lilienthal-Museum Bildarchiv, Archiv-ID 00109 [9]

Lilienthal built different devices with diameters ranging from 2 to 7 m [8]. Testing across this range, he recognized that too small an arm radius amplifies systematic errors such as strong streamline curvature along the circular path, wake interaction between the two arms and wings, and larger relative blockage, making the measurements less representative of straight flight [2, Ch.27]. He therefore adopted a diameter of 7 m for the final measurements. The wings were roughly 4.5 m above ground, providing drop height for the weights and reducing near-ground interference. Mean test speeds at the wings reached about $V \approx 12\,\mathrm{m/s}$ [11]. He tested many planforms and cambers, from about 1/40 of the chord ("width" in his terminology), up to 1/12 [2, 13]. To put everything in motion and take all the measurements, he needed more than one person; for that reason his brother Gustav and another assistant helped throughout the experiments.

2.3.3. Results and limitations

The device produced the datasets that became Lilienthal’s Plates. Those data confirmed the advantage of cambered wings and, arranged versus angle of attack, correspond to early lift–drag polars. At the same time, several limits are inherent to the method: friction in the system, subtraction of arm and hub resistance, finite radius effects (curved flow and

two-arm/two-wing wake interaction), modest Reynolds numbers, fabric permeability, and the historical reduction using the Smeaton coefficient [20]. These factors explain in part the differences between rotating-arm and wind measurements [8].

2.4. The evolution of flight after Lilienthal

Lilienthal's measurements and gliding demonstrations set the starting point for many others. Most notably, the Wright brothers, starting from his Plates, adopted a revised Smeaton coefficient ($k = 0.0033\,\mathrm{lbf}/(\mathrm{ft}^2\,\mathrm{mph}^2)$) and built their own balance and wind tunnel in 1901; with these they were able to obtain consistent lift and drag data for cambered wings and propellers [8, 10]. They achieved the first controlled, sustained flight of an engine-powered, "heavier than air" aircraft on 17 December 1903 at Kitty Hawk [8].



Figure 2.10: Wright brothers' first powered flight, 17 December 1903, Kitty Hawk. Library of Congress, digital ID LC-DIG-ppprs-00626 [21]



Figure 2.11: Wright brothers' 1901 wind tunnel (replica). National Museum of the U.S. Air Force [22]

2.5. Aerodynamic theory

Lift and drag govern the possibility of flight. Lilienthal set out to understand how these forces act on surfaces and whether controlled flight could be achieved at all. In doing so, he produced an early analysis of aerodynamic coefficients.

2.5.1. Modern forces and aerodynamic coefficients

Any body in a flow experiences two main aerodynamic forces: the drag D, aligned (on average) with the oncoming flow and expressing resistance to motion, and the lift L, approximately normal to it and enabling flight. Today these forces are expressed using

dynamic pressure and nondimensional coefficients [14]:

$$D = q\,S\,C_{\mathrm{D}}, \qquad L = q\,S\,C_{\mathrm{L}}. \tag{2.1}$$

The dynamic pressure is

$$q = \frac{1}{2}\,\rho\,V^2, \tag{2.2}$$

with ρ the air density and V a suitable reference speed (for free-stream conditions, $V = U_\infty$) [14]. The reference area S must be stated: for finite wings, S is the planform area; for 2D sections one often uses per-unit-span forces L', D' and the section coefficients

$$c_d = \frac{D'}{q\,c}, \qquad c_\ell = \frac{L'}{q\,c}, \tag{2.3}$$

with c the chord. For bluff bodies, S is commonly the frontal area.

Often the pitching moment is also reported, about a specified reference point (typically the quarter-chord) and the spanwise (y) axis (for 2D sections, the moment about the quarter-chord):

$$M = q\,S\,c\,C_{\mathrm{M}}. \tag{2.4}$$

Meaning of the aerodynamic coefficients. C_{L} and C_{D} encapsulate how geometry and flow physics determine the forces and are dimensionless normalizations of force that remove the effects of size and speed using (q, S). They are functions of angle of attack and similarity parameters:

$$C_{\mathrm{L}}, C_{\mathrm{D}}, C_{\mathrm{M}} = f(\alpha,\ \mathrm{Re},\ \mathrm{Ma},\ \mathrm{AR},\ \text{roughness},\ \text{motion})\,. \tag{2.5}$$

C_{L} primarily reflects the pressure difference between upper and lower surfaces (circulation/deflection of flow); C_{D} combines pressure drag (form/separation) and skin-friction drag (wall shear). Consequently, C_{D} grows when separation or surface roughness increases, while C_{L} depends strongly on camber, thickness, and α.

The Reynolds number Re

$$\mathrm{Re} = \frac{\rho\,V\,\ell}{\mu} \tag{2.6}$$

compares inertial to viscous effects using a characteristic length ℓ and dynamic viscosity μ. A laminar BL has low skin-friction but higher sensitivity to adverse pressure gradients and earlier separation. A turbulent BL has higher skin-friction but more near-wall momentum, delaying separation and often improving lift at moderate-high α. The net effect is problem-

dependent: forcing or allowing turbulence can increase C_D (friction) yet reduce total drag if it prevents a large separated region. There are no universal "critical" values for external flows like those in Lilienthal's case (flow over a wing/airfoil): transition depends on disturbance level, pressure gradients, surface condition, and the local Reynolds number. By contrast, for internal flows a common guide is: $\mathrm{Re} \leq 2300$ laminar, $2300 < \mathrm{Re} < 4000$ transitional, and $\mathrm{Re} \geq 4000$ turbulent. The Mach number Ma

$$\mathrm{Ma} = \frac{V}{a} \tag{2.7}$$

compares speed to the local speed of sound a and sets compressibility effects: low subsonic/incompressible $\mathrm{Ma} \leq 0.3$; subsonic (compressible) $0.3 < \mathrm{Ma} < 0.7$; transonic $0.7-1.2$ (shocks, shock-induced separation); supersonic $1.2-5$; hypersonic $\mathrm{Ma} \geq 5$.

At small α, many wings exhibit an approximately linear lift curve, $C_L \approx C_{L_\alpha}\,\alpha$ (radians). Near stall, separation, hysteresis, and (at low Re) laminar-separation bubbles appear and C_D rises sharply.

Measurement practice. Today, aerodynamic forces are studied and measured using both computation (CFD) and controlled experiments, most notably wind-tunnel testing. Such closed-section testing was unavailable to Lilienthal, who relied on a whirling arm and a wind apparatus in natural wind. Modern facilities reproduce target flow conditions and measure forces/moments directly. In wind tunnels, q is obtained from Pitot–static measurements $(p_t - p_\infty)$, ρ from the test-section thermodynamic state, and forces/moments from internal or external balances (as in the wind-tunnel tests of Ch. 6). Because balances naturally resolve normal N and axial A components relative to the flow or chord line, results are often converted to L and D using:

$$C_L = C_N \cos\alpha - C_A \sin\alpha, \qquad C_D = C_N \sin\alpha + C_A \cos\alpha. \tag{2.8}$$

Additional methods include surface-pressure integration (from $C_p = (p - p_\infty)/q$) and wake-momentum surveys for drag.

The coefficient-based normalization (Eq. 2.1) became standard in the early 20th century through wind-tunnel practice and similarity analysis (Reynolds, Eiffel, Prandtl's school, NACA), and it is related to the 19th-century framework in Section 2.5.3.

2.5.2. Historic forces and knowledge

Lilienthal grouped lift and drag under the term "air resistance". While the detailed action of the flow on bodies was not yet theoretically explained, he was among the first to measure

these forces systematically and to reason about their trends. His book discusses ideas that are standard today but new at the time: the superiority of curved (cambered) wings over flat plates, qualitative streamline sketches around plates and curved surfaces, the role of angle of attack, considerations on the work required for flight, wing outlines, and wind effects [2]. Not every inference was correct by modern standards, but his program established a practical and conceptual foundation. He sought wind-tunnel-like conditions using several devices, from the *Rundlaufapparat* to a wind apparatus.

What was firmly known in Lilienthal's era.

- The square-law scaling of "air resistance" with speed: $D \propto V^2$ (basis of Smeaton's law).
- Bernoulli's relation linking pressure and speed in steady, inviscid flows (used qualitatively in early lift ideas).
- Angle of attack as a controlling parameter; center-of-pressure concepts for plates/sails were tabulated.
- The laminar–turbulent distinction was being established (Reynolds' dye-stream experiments, 1883).

Key advances followed shortly after Lilienthal: boundary-layer theory (Prandtl, 1904) and modern lift theory (Kutta–Joukowski, 1902–1906).

2.5.3. The Smeaton coefficient

In Lilienthal's time, aerodynamic theory was still incomplete. It was known empirically that aerodynamic forces scale with the square of velocity, $L, D \propto V^2$, but the standard form and constants were not yet theorized.

John Smeaton (1724-1792) [23] introduced a practical relation:

$$D = k\, S\, V^2, \tag{2.9}$$

with D in pound-force (lbf), S in square feet (ft^2) and V in miles per hour (mph). The constant k is now called the Smeaton coefficient [20]. Smeaton set this value by measuring the load on a flat plate of $S = 1\,\mathrm{ft}^2$ at normal incidence and at $V = 1\,\mathrm{mph}$. From these experiments he measured a force of $D = 0.005\,\mathrm{lbf}$, hence

$$k = 0.005\ \frac{\mathrm{lbf}}{\mathrm{ft}^2\ \mathrm{mph}^2}.$$

To determine this constant, he varied the speed and exploited the observed V^2 scaling to collapse the data and extract k. The flat-plate reference was chosen as the standard because it was thought to be easy to measure accurately.

SI conversion

Using $1\,\mathrm{lbf} = 0.45344\,\mathrm{kgf}$, so $1\,\mathrm{lbf} = 4.44822\,\mathrm{N}$, $1\,\mathrm{ft}^2 = 0.092903\,\mathrm{m}^2$, and $1\,\mathrm{mph} = 0.44704\,\mathrm{m/s}$, this value becomes:

$$k = 0.005\,\frac{\mathrm{lbf}}{\mathrm{ft}^2\,\mathrm{mph}^2} = 0.12216\,\frac{\mathrm{kgf}}{\mathrm{m}^2\,(\mathrm{m/s})^2} = 1.19835\,\frac{\mathrm{N}}{\mathrm{m}^2\,(\mathrm{m/s})^2}.$$

Lilienthal's adaptation

Lilienthal in his book cited Smeaton's k as accepted and correct [2]. Nonetheless, he used

$$k = 0.13\,\frac{\mathrm{kgf}}{\mathrm{m}^2\,(\mathrm{m/s})^2},$$

writing it also on the x-axis of his Plates; this slightly larger value likely reflects some differences from the period's unit conventions and rounding practices. In his book Lilienthal wrote: "These values illustrate the ratio of the resistance to the normal air resistance $c\,90°$, calculated from equation $L = 0.13\,F\,V^2$, and at the same time indicate their direction" [2, Ch.19], and "As slight curvatures are without effect upon the air pressure $C\,90°$, it is always to be calculated according to formula: $L = 0.13\,F\,V^2$" [2, Ch.28]. In his notation, L denotes the drag ("air resistance"), F the surface and V the velocity. These passages, first concerning flat plates and the second concerning curved wings, explain how he reduced all of his measurements using Equation 2.9, with $k = 0.13\,\mathrm{kgf}/[\mathrm{m}^2\,(\mathrm{m/s})^2]$. Since k scales with the normal incidence drag of the chosen reference body (see the relation $k = \frac{1}{2}\rho C_{\mathrm{D},90°}$ introduced below), applying a flat-plate k to cambered wings (with different $C_{\mathrm{D},90°}$ and Reynolds-number effects) introduces a systematic bias whose exact size is hard to quantify a priori. A complementary analysis infers an effective k from the present data in Section 5.2.

There remains debate over whether Lilienthal inferred an effective value of k from his own data, applied Smeaton's value directly, or normalized results using measurements at 90°, as discussed by Anderson [8]. These alternatives will be formalized in Section 4.5, and their results shown in Section 5.2.

Modern interpretation

In modern notation, the aerodynamic forces are written using the dynamic pressure, rather than $k\,S\,V^2$ as it was considered by Smeaton [14]:

$$q = \frac{1}{2}\,\rho\,V^2, \tag{2.10}$$

$$L = q\,S\,C_{\mathrm{L}}, \quad D = q\,S\,C_{\mathrm{D}}. \tag{2.11}$$

Comparing Equation 2.9 with Equation 2.11 for a flat plate at 90° yields a modern expression for the Smeaton coefficient:

$$k = \frac{1}{2}\,\rho\,C_{\mathrm{D}}. \tag{2.12}$$

In the modern view k is not a universal constant, as it was considered by Smeaton; it depends on air density and on the reference shape through $C_{\mathrm{D},90^\circ}$. With standard sea-level density $\rho = 1.225\,\mathrm{kg/m^3}$ [24] and a common value of $C_{\mathrm{D},90^\circ} = 1.28$ for a flat plate at normal incidence [25], k_{mod} results:

$$k_{\mathrm{mod}} = 0.784 \frac{\mathrm{N}}{\mathrm{m^2\,(m/s)^2}}.$$

This is close to the Wright brothers' revised Smeaton coefficient, $k = 0.0033\,\mathrm{lbf/(ft^2\,mph^2)}$, which converts to $k = 0.791\,\mathrm{N/[m^2\,(m/s)^2]}$ [8, 15].

For the Lilienthal definitions of coefficients, applying different values of k leads to different reported coefficients:

$$C^{(\mathrm{Lil})}(k) \;=\; \frac{1}{k}\,\frac{F}{SV^2}, \qquad C^{(\mathrm{Lil})}(k_{\mathrm{mod}}) \;=\; \frac{1}{k_{\mathrm{mod}}}\,\frac{F}{SV^2}. \tag{2.13}$$

Applying Lilienthal's value of $k = 1.275\,\mathrm{N/[m^2\,(m/s)^2]}$ (slightly higher than Smeaton's original), instead of the modern value of $k_{\mathrm{mod}} = 0.784\,\mathrm{N/[m^2\,(m/s)^2]}$, yields:

$$C^{(\mathrm{Lil})}(k) \;=\; \frac{1}{1.275}\,\frac{F}{SV^2} \;=\; \frac{0.784}{1.275}\,\underbrace{\left(\frac{1}{0.784}\,\frac{F}{SV^2}\right)}_{C^{(\mathrm{Lil})}(k_{\mathrm{mod}})} \;\approx\; 0.62\,C^{(\mathrm{Lil})}(k_{\mathrm{mod}}),$$

or equivalently $C^{(\mathrm{Lil})}(k_{\mathrm{mod}}) \approx 1.63\,C^{(\mathrm{Lil})}(k)$. This value of the Smeaton coefficient (k_{mod}) lets one reproduce a coefficient computation in the same manner Lilienthal likely used for his Plates, while adopting a modern, more correct magnitude of k.

However, today coefficients are normalized with (q, S), not with (k, S, V^2). To compare the historical and modern definitions explicitly:

$$C_{\mathrm{L}}^{(\mathrm{Lil})} = \frac{L}{k\,S\,V^2}, \qquad C_{\mathrm{L}} = \frac{L}{\frac{1}{2}\,\rho\,S\,V^2}, \tag{2.14}$$

$$C_{\mathrm{D}}^{(\mathrm{Lil})} = \frac{D}{k\,S\,V^2}, \qquad C_{\mathrm{D}} = \frac{D}{\frac{1}{2}\,\rho\,S\,V^2}. \tag{2.15}$$

From the relations above:

$$\frac{C^{(\mathrm{Lil})}}{C} = \frac{\frac{1}{2}\,\rho}{k}, \qquad C^{(\mathrm{Lil})} = \frac{\frac{1}{2}\,\rho}{k}\,C. \tag{2.16}$$

At sea level $\rho = 1.225\,\mathrm{kg/m^3}$ (so $\frac{1}{2}\rho = 0.6125\,\mathrm{N/[m^2(m/s)^2]}$) and using Lilienthal's $k = 1.275\ \mathrm{N/[m^2(m/s)^2]}$,

$$C^{(\mathrm{Lil})} \;=\; \frac{0.6125}{1.275}\,C \;\approx\; 0.48\,C.$$

Understanding how the Smeaton coefficient was adopted and adapted is essential to reconstruct Lilienthal's data reduction. A different normalization framework and an inaccurate value of k plausibly explain biases in his coefficient magnitudes, even though the overall trends (polar shapes and lift–drag ratios) were largely consistent (see Anderson [8]).

Representative values across unit systems

Source / Unit System	$\frac{\text{lbf}}{\text{ft}^2\,\text{mph}^2}$	$\frac{\text{kgf}}{\text{m}^2\,(\text{m/s})^2}$	$\frac{\text{N}}{\text{m}^2\,(\text{m/s})^2}$
Smeaton	0.00500	0.12216	1.19835
Lilienthal value	0.00532	0.13000	1.27530
Wright value	0.00330	0.08062	0.79091
Modern value: $\frac{1}{2}\,\rho\,C_{\mathrm{D},90^\circ}$	0.00327	0.07989	0.78372
Modern normalization: $\frac{1}{2}\,\rho$	0.00256	0.06244	0.61250

Unit conversions used: $1\,\mathrm{lbf} = 4.44822\,\mathrm{N}$, $1\,\mathrm{ft}^2 = 0.092903\,\mathrm{m}^2$, $1\,\mathrm{mph} = 0.44704\,\mathrm{m\,s^{-1}}$, $1\,\mathrm{kgf} = 9.80665\,\mathrm{N}$.

Table 2.1: Representative values of the Smeaton coefficient k and of the modern normalization $\frac{1}{2}\,\rho$

The last row is not a Smeaton coefficient k, but the modern normalization constant $\frac{1}{2}\rho$ shown for unit and value comparability.

Limits and applicability of k

Using a single k for every geometry and condition is misleading. Even for a flat plate, k varies with ρ; using it for a different wing or body does not account for the change in $C_{\mathrm{D},90^\circ}$. As seen in Table 2.1, Lilienthal's k is about 62 % larger than a modernized flat-plate value and about twice the modern normalization constant $\frac{1}{2}\rho$; if Equation 2.9 was actually used to reduce his data, this overestimate propagates directly into the reported coefficients, yielding values lower than those that would be computed today with q-based normalization, or even with a modern value of k.

The literature generally agrees that Lilienthal's trends (polars' shape, qualitative lift/drag ratios) were broadly right, whereas magnitudes were biased; the normalization framework and the value of k then in use can plausibly account for the error in Lilienthal's coefficients [10]. An alternative view is that he may have avoided relying on a fixed k by measuring the force at 90° directly; in that case the coefficients are again ratios to the 90° "air resistance", formed from the actual measurement rather than an empirical k, thereby removing any k-induced bias (see Anderson [8]).

3 | Apparatus Design and Reconstruction

This chapter documents the reconstruction of Otto Lilienthal's whirling-arm apparatus (*Rundlaufapparat*) to replicate his experiments. The primary goal was to reproduce the original geometry, kinematics, and measurement principles as faithfully as possible from the surviving descriptions and drawings. Where dimensions or materials are unknown, carefully chosen adaptations are introduced. These modifications are designed not to affect the aerodynamic outcomes or the measurement methodology (explained in detail in Ch. 4–5); potential impacts are analyzed later in this chapter.



Figure 3.1: *Rundlaufapparat*

3.1. Structure

The apparatus consists of:

- a rigid wooden base frame;
- a vertical steel shaft;
- a pair of rotating arms carrying the wings at their tips;
- a transmission system composed of a central wooden drum, coupled to the shaft, two wooden pulleys, and weights attached to ropes wound on the central drum;
- a counterbalanced lever for lift measurement.

Gravity pulls the weights down, setting the device in motion.

Figure 3.2 shows the geometry of the apparatus:

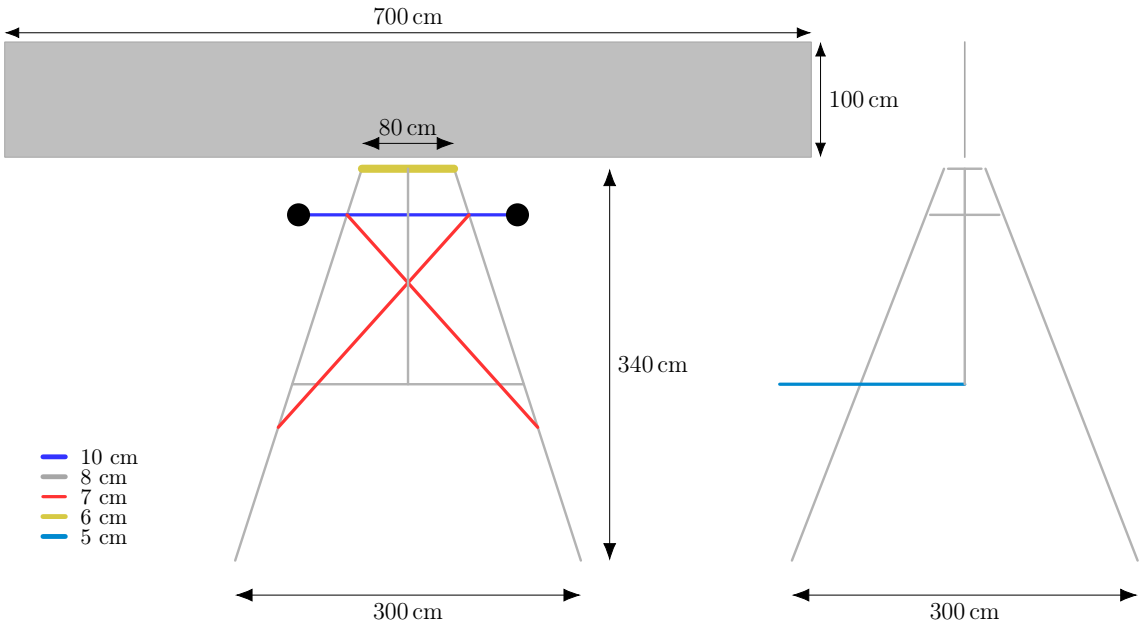

Figure 3.2: *Rundlaufapparat*: front view (left) and side view (right)

Although not all geometric dimensions are known, the most critical ones are preserved. Two key parameters are the drop height of the driving weights, approximately $h = 3\,\mathrm{m}$, and the diameter of the wing rotation, $d = 7\,\mathrm{m}$ [2, 11]. The remaining dimensions, when unspecified, are inferred from drawings and adapted to ensure sufficient structural strength and stiffness to sustain the expected loads. After finalizing the frame, the base is further stiffened with wooden cross members tying the perimeter beams together.

3.1.1. Reference frame and sign conventions

The z–axis is vertical along the shaft, r is radial in the arm plane, and θ increases with the rotation direction. The wing angle of attack α is defined about the local chord, with positive nose-up; lift is normal to the inflow and drag is tangential.

Table 3.1 reports the material and principal dimensions of each structural component.

The CAD drawings of the components designed with CATIA are shown in Appendix A.

Component	**Material**	**Principal dimensions (mm unless noted)**
Base frame	Wood	plan footprint 3000 × 3000; height $h = 3400$
Vertical shaft	Steel	∅20; length $L = 2600$
Central drum	Wood	outer ∅500, inner ∅450; $t_{\text{outer}} = 6.5$, $t_{\text{inner}} = 12$; hole ∅32
Pulley	Wood + aluminum axle	outer ∅350, inner ∅300; $t = 12$; axle hole ∅32
Drive ropes	Braided nylon	∅2; length ≥ 3000 per run
Arms	Wood	horizontal $L = 3500$; vertical $h = 1000$; diameter $d = 20$; cross rods at $r = 1750$ and $r = 3500$
Bracing cables	Steel	∅2; layout explained in Sec. 3.4.2
Shaft lugs	Steel	length 300
Wing	Wood + canvas	$c = 400$, $b = 1800$, $S = 0.50\,\text{m}^2$; T.E. support length 500
Counterbalance lever	Wood + steel	arms 900 (inner) and 900 (outer)
Counterweights	Iron	6.25 kg × 2

Table 3.1: Structural component index

3.2. Central drum

One of the crucial elements of the device is the central drum. It is connected to the falling weights via ropes and, by transmitting torque to the vertical shaft, sets the entire system in motion.

3.2.1. Dimensions and geometry

From Lilienthal's notes, the original drum diameter was approximately $d_0 = 350\,\text{mm}$ [11]. Although drum diameter influences the torque transmitted to the shaft, a larger assembly is adopted to obtain sufficient torque with lower driving masses and to reliably host the ropes. The implemented geometry consists of a stack of three wooden disks with $d_{\text{drum,outer}} = 500\,\text{mm}$ alternating with two disks with $d_{\text{drum,inner}} = 450\,\text{mm}$, forming two rope grooves. The inner disks have thickness $t_{\text{inner}} = 12\,\text{mm}$ each, while the outer disks have $t_{\text{outer}} = 6.5\,\text{mm}$ each. The inner disks are made thicker to retain the ropes in the grooves and prevent them from coming off the drum.

All disks include a central bore of diameter $d_{\text{hole}} = 32\,\text{mm}$ to couple the stack to the vertical shaft. Around this bore, four auxiliary holes of diameter 8 mm are provided for through-bolts that clamp the stack together. Glue is applied between contact faces before tightening to ensure stiffness and prevent slip (Fig. A.1 for full geometry).



(a) (b)

Figure 3.3: Central drum overview

For subsequent computations, the winding radius is taken as the inner groove radius at which the ropes act: $r_{\text{drum}} = d_{\text{drum,inner}}/2 = 225\,\text{mm}$.

3.2.2. Torque vs. rotation trade-off

Increasing r_{drum} scales the applied drive torque linearly:

$$\tau_{\text{drive}} = r_{\text{drum}} \sum_i m_i\, g \tag{3.1}$$

but it reduces the available angular excursion from a fixed drop height h:

$$\theta_{\max} = \frac{h}{r_{\text{drum}}}, \qquad n = \frac{\theta_{\max}}{2\pi} = \frac{h}{2\pi\, r_{\text{drum}}}. \tag{3.2}$$

Relative to Lilienthal's $d_0 = 350\,\text{mm}$ ($r_0 = 175\,\text{mm}$), a new drum radius r_{drum} scales the torque and the available turns as

$$\frac{\tau}{\tau_0} = \frac{r_{\text{drum}}}{r_0}, \qquad \frac{n}{n_0} = \frac{r_0}{r_{\text{drum}}}. \tag{3.3}$$

Considering a drop height of $h = 3\,\text{m}$ in both cases, the number of turns is

$$n_0 = \frac{3}{2\pi \cdot 0.175} \approx 2.7284 \text{ turns}, \quad n = \frac{3}{2\pi \cdot 0.225} \approx 2.1221 \text{ turns}. \tag{3.4}$$

Thus, increasing the radius from $r_0 = 175\,\text{mm}$ to $r_{\text{drum}} = 225\,\text{mm}$ yields

$$\Delta n = n - n_0 = -0.6063 \text{ turns } (-22.22\%), \quad \frac{\tau}{\tau_0} = \frac{0.225}{0.175} = 1.2857 \ (+28.57\%). \tag{3.5}$$

This trade-off is acceptable for the present tests and can be changed in future work by building a 350 mm drum for a direct comparison.

3.2.3. Drum–shaft connection

The drum stack is connected to the vertical shaft by a flanged spigot adapter (Fig. A.3).

It consists of:

- a circular flange ("base") bolted to the top disk with four M8 screws and large washers;
- a concentric spigot with external diameter 32 mm that fits the disk bore for concentric location and lateral support;
- an internal through-bore 20 mm that slides over the shaft.

Torque is transmitted to the shaft by a cross-bolt passing through aligned holes in the adapter and the shaft, assisted by friction from the clamped interfaces. This arrangement provides a reliable, keyless joint and prevents relative rotation during operation.

3.2.4. Drive mechanism

Weights m_i are attached to ropes that pass over the pulleys and are wound onto each groove. This configuration is chosen to allow the system to reach at least a number of $n = 2$ turns before the weights touch ground, matching the typical run length used by Lilienthal in his experiments. Two small holes in the outer disks allow the rope ends to

be secured. The drive ropes are low-stretch braided nylon lines, $d = 2\,\text{mm}$, selected for adequate strength and minimal creep.

3.3. Pulleys

The pulleys are a fundamental part of the drive system; they route the ropes between the weights and the central drum, enabling transmission of the driving torque to the wings. Their placement on the structure ensures that the weights drop freely without striking or damaging the frame. Since Lilienthal's pulley dimensions are not known, their sizes are adapted to the available space while preserving their function and while meeting stiffness and strength requirements.

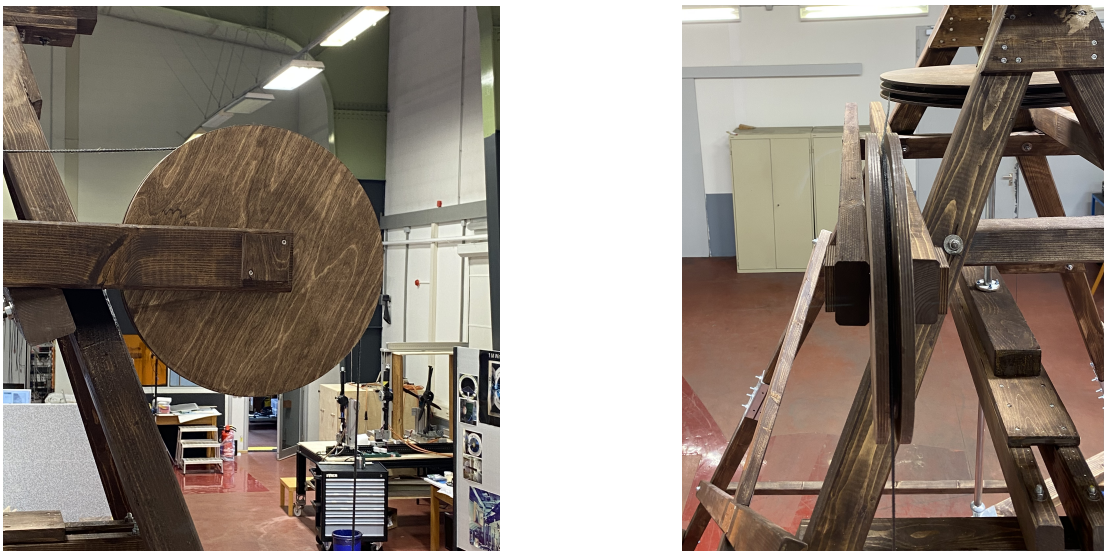

(a) Front view (b) Side view

Figure 3.4: Pulleys overview

3.3.1. Dimensions and geometry

Each pulley is composed of three wooden disks: two outer disks with diameter $d_{\text{pulley,outer}} = 350\,\text{mm}$ and one inner disk with $d_{\text{pulley,inner}} = 300\,\text{mm}$, all with thickness $t = 12\,\text{mm}$. The step creates a groove that guides the rope, transmits torque, and also prevents the rope from slipping out during tests. As with the other disks, a central bore of $d_{\text{hole}} = 32\,\text{mm}$ is provided to accept the rotational axle.

The pulleys are placed at the required height $h = 3\,\text{m}$ and with an offset of about 70 cm from the center of the structure, to allow the correct fall of the weights.

3.3.2. Rotation system

The pulleys rotate on a fixed aluminum axle clamped to two side beams connected to the main structure. The axle surface is smooth to minimize friction; a small axial gap is maintained between each pulley and the beams to allow the pulleys to spin freely while limiting lateral movement, and to avoid rubbing and additional frictional losses.

With this driving system (weights, pulleys, and central drum), friction and other non-aerodynamic losses are unavoidable (rope bending/sliding in the grooves, contact at the pulley axle, and lateral movement of the pulleys). Their combined effect is analyzed from the measured speed–time history and reported in Section 5.1. It is then included in the MATLAB model as part of the resisting torque τ_{friction} for more analysis (see Sec. 5.1.7 and Appendix D).

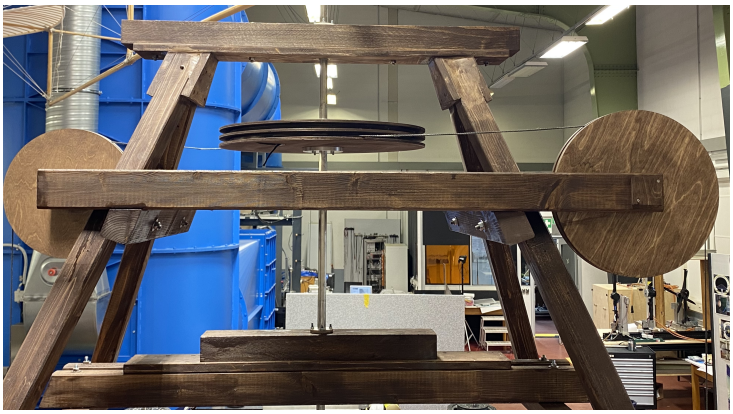

Figure 3.5: Driving system of the *Rundlaufapparat*

3.4. Arms

The arms carry the wings at their extremities. Their shape must satisfy three important requirements:

- hold the wings in the prescribed position with sufficient stiffness;
- add as little aerodynamic drag as practical;
- preserve geometry without bending and safely sustain all test loads during rotation.

3.4.1. Dimensions and geometry

Each arm (one per side) is composed of four cylindrical wooden rods of diameter $d_{\text{arm}} = 20\,\text{mm}$, arranged as a rectangular frame. Two longitudinal rods of length $L_{\text{arm}} = 3.5\,\text{m}$

run radially from the central shaft and are separated vertically by a distance of 1 m. Two transverse rods, each of $\ell_{\text{tr}} = 1\,\text{m}$, connect the longitudinal ones: the first is positioned at mid-span ($r = 1.75\,\text{m}$) and the second one at the tip ($r = L_{\text{arm}}$). The resulting structure is a rectangular frame, as shown in Figure 3.7.

The wing is mounted in the middle of the tip transverse rod, at a rotational radius of $R = L_{\text{arm}} = 3.5\,\text{m}$.

3.4.2. Bracing system

Once connected to the central shaft, the bare wooden frame was still insufficiently stiff. It had to carry its own weight, the wings, and the aerodynamic loads during rotation while remaining in plane. Therefore, a cable bracing system made of 2 mm steel wires, tensioned with turnbuckles, is added to stabilize the frame and preserve its geometry.

At the center of the shaft ($z = 0.5\,\text{m}$ above the lower longitudinal rod), two cylindrical steel lugs (300 mm long) extend out of the arm plane. These provide favorable positioning for the cables and help restrain out of plane bending of the structure. Layout per arm side:

- 2 in-plane cables: one cable from the upper hub corner to the lower tip corner, and one from the lower hub corner to the upper tip corner;
- 4 out-of-plane cables to mid cross rod: from the two shaft lugs to the mid cross rod, one to the upper longitudinal rod and one to the lower, from each lug;
- 4 out-of-plane cables to tip cross rod: from the two shaft lugs to the tip cross rod, again one to the upper longitudinal rod and one to the lower from each lug.

A total of 10 cables per side are installed. This layout controls in-plane and out-of-plane bending and provides torsional stiffness, ensuring the arms maintain their shape and safely sustain the test loads. The exact layout is illustrated in Figure 3.7.

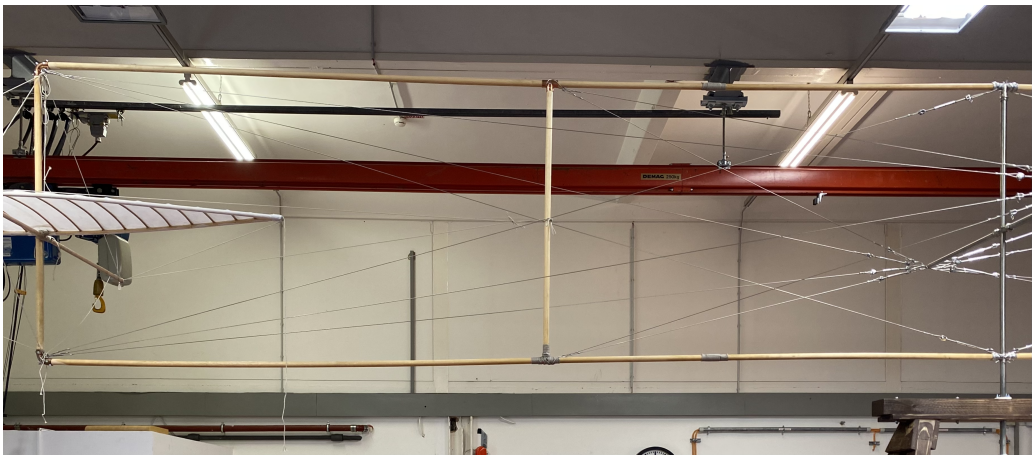

Figure 3.6: Arm frame assembly

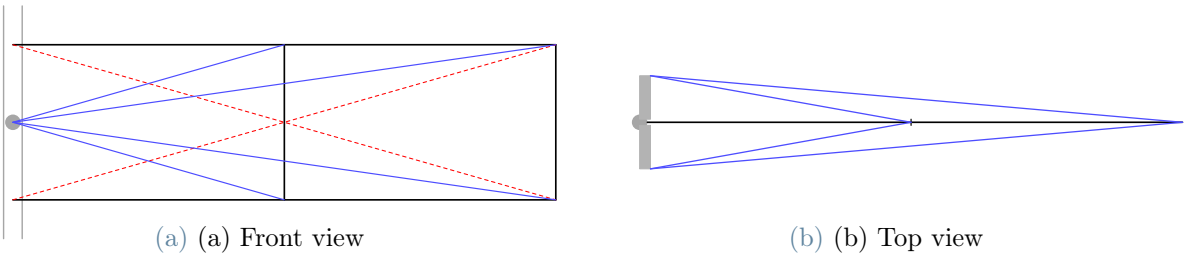

(a) (a) Front view

(b) (b) Top view

Figure 3.7: Arms: geometry and cable layout. **(a)** Front view: rectangular arm frame with in-plane cables (red) and out-of-plane cables (blue). **(b)** Top view: cables originate from two steel lugs connected to the shaft center and run to mid-span and tip.

3.5. Wings

For the tests on the *Rundlaufapparat*, wings similar to Lilienthal's are used.

Their main characteristics are:

- chord $c = 0.4\,\mathrm{m}$;
- span $b = 1.8\,\mathrm{m}$;
- reference area $S = 0.5\,\mathrm{m}^2$;
- camber of 1/12 of the width (chord), as defined by Lilienthal [2];
- planform: approximately elliptical (see Fig. 3.9);
- construction: wooden frame covered with canvas.



(a) Front view (b) Side view

Figure 3.8: Test wing

To connect the wings to the arm structure and to allow precise adjustment of the angle of attack (α), a set of ropes is routed from points on the arms to multiple attachment points on each wing (leading edge, trailing edge, and wingtips at mid-chord), as shown in Figure 3.8. At the mid-span trailing edge, a short (50 cm) cylindrical wooden piece was added to provide a secure connection point to the structure, help the wing hold its set position during rotation, and make setting at different angles α easier. This addition locally disturbs the flow, introducing a small error in the results; nonetheless, it is kept in these tests for practicality and historical fidelity, and will be removed in future iterations.

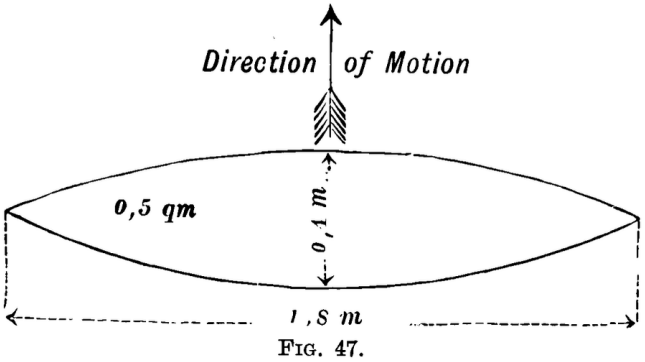

FIG. 47.

Figure 3.9: Wing shape adopted by Lilienthal in his experiments [2, Fig. 47, Ch. 28]

3.5.1. Airfoil selection

Lilienthal tested several cambered surfaces and, within the whirling arm setup, obtained similar aerodynamic results across different shapes tested (see Lilienthal [2, Ch.28]). For the historical experiments, the simplest airfoil to manufacture is chosen, shown in Figure 3.10:

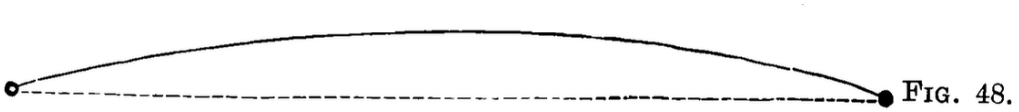

Figure 3.10: Historical airfoil tested by Lilienthal [2, Fig. 48, Ch. 28]

For the simulation study (Ch. 7), the wind tunnel tests on the scaled model (Ch. 6), and for future analyses and experiments (Ch. 8), a different airfoil is adopted and discussed in detail in Section 6.1.

3.5.2. Angle of attack setting

Each wing is held by ropes from the arm frame corners to the wing extremities to be consistent with the original apparatus; in this way, the desired position and angle α can be set and maintained during the test rotation. The angle of attack is defined using the chord line from leading to trailing edge, the same convention also adopted in the wind tunnel experiments (Ch. 6).

Because rope lengths are adjusted manually for each target α, small setting errors arise from operator handling (mounting and rigging) and inclinometer reading (resolution and parallax), introducing some uncertainty in the exact angle achieved. This problem has been minimized as much as possible, keeping every measured angle within $\pm 0.5^\circ$ of the target value.

The test campaign covers ten angles, in line with Lilienthal's range:

$$\alpha \in \{-5^\circ\,,\ 0^\circ\,,\ 5^\circ\,,\ 10^\circ\,,\ 15^\circ\,,\ 20^\circ\,,\ 30^\circ\,,\ 40^\circ\,,\ 60^\circ\,,\ 90^\circ\}.$$

3.6. Counterbalanced lever and lift balance

The last element needed to record the results is a counterbalanced lever connected to the central shaft. This lever moves up and down with the rotating assembly (shaft, drum, arms, wings) and allows the lift generated by the two wings to be read as an equivalent mass on a small balance during the rotation.

The system consists of:

- a triangular wooden lever frame linked to the central shaft that rises and lowers with

the moving structure;

- removable counterweights mounted on the lever to balance the weight of the moving structure, isolating the lift measurement;
- a small balance for the equivalent masses used to measure lift.



Figure 3.11: Counterweight lever system

3.6.1. Dimensions and geometry

The lever is a triangular frame made of three wooden beams, plus a fourth one to strengthen this structure. The inner vertex rests against the shaft at the apparatus center. The lever pivot, which is a horizontal crossbeam of the main frame, is located 90 cm from this inner connection point; from the pivot to the outboard tip there is a further 90 cm. The outboard side of the triangle is about 160 cm long.

Two 6.25 kg counterweights are mounted near the outboard ends (total added mass of 12.50 kg), as shown in Figure 3.11.

3.6.2. Lift balance

At the shaft connection a small hanging basket acts as the balance for lift measurements. During a test, the moving system tends to rise as the lift generated by the wings increases with speed; masses are added to the basket until, at steady state, the lever is horizontal. At steady state:

- the rotational speed is constant and so is the wing speed;

- the lift is no longer increasing;
- the upward motion stops.

With the lever horizontal and equal arms length (90 cm), under steady conditions the moments about the pivot balance. The mass in the basket therefore represents the total lift of both wings, expressed in (kgf). In SI units, (N), the lift per wing is:

$$L = \frac{m_{\mathrm{L}}}{2}\, g, \tag{3.6}$$

where m_{L} is the total mass added in the balance.



Figure 3.12: Lift balance

4 | Methods: Lilienthal Measurement Model

Symbols

Symbol	Description
r	drive-drum radius [m]
R	arm-tip radius [m]
n	number of turns completed before the weights touch the ground [−]
S	reference area [m^2]
g	gravitational acceleration [m/s^2]
ρ	air density [kg/m^3]
V_w	speed measured in paired runs: wings with m and empty with m' [m/s]
V_a	speed measured in empty configuration with mass m [m/s]
t_w	time to complete n turns at speed V_w [s]
t_a	time to complete n turns at speed V_a [s]
m	mass used for the paired (wings and empty) runs [kg]
m'	empty-run mass that yields the same speed V_w [kg]
m_f	friction-equivalent constant mass [kg]
$D_w(V)$	wing drag at speed V [N]
$D_a(V)$	total drag in empty configuration at speed V [N]
$D_{a+w}(V)$	total drag in wings configuration at speed V [N]
m_L	mass added on the balance to counteract lift [kg]
r_{lev}	lever arm length (each side) [m]
m_{bal}	counterweight mass used to balance the system weight [kg]
m_{sys}	rotating system mass (shaft, drum, arms, wings) [kg]

Table 4.1: Symbols used in the measurement model

Table 4.1 lists the symbols used in the rotating-apparatus measurement model. In the text we refer to two configurations: empty (arms only) and wings (arms + wings). Unless stated otherwise, speeds are tip speeds.

4.1. Kinematics: speed from turn time

To understand how Lilienthal defined drag with the *Rundlaufapparat*, it is necessary to clarify what he measured in his experiments. In his notes he reported [11]:

- the time required for the apparatus to complete $n = 2$ turns,
- the falling mass applied to move the system,
- the mass applied to the lift balance.

Whether the timing referred to the last two turns after accelerating the apparatus, or to exactly two turns from rest until the weights reached the ground, is still unclear and will be discussed in more detail in Chapter 5. In the former case, using the final two turns would reduce acceleration effects and better approximate steady conditions, yielding more accurate measurements.

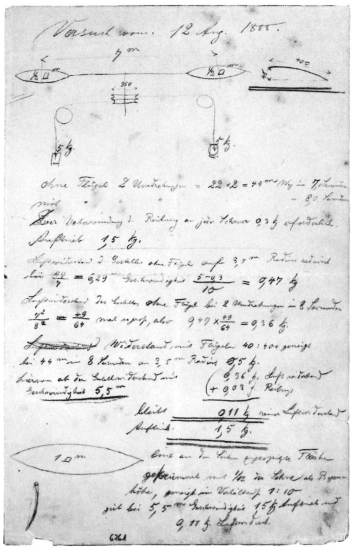

Figure 4.1: Otto Lilienthal, *Skizze und Berechnungen zu Versuchen am großen Rundlaufapparat* (Sketches and calculations for experiments on the large whirling apparatus), 12 Aug. 1888; pencil and ink on paper, 21.0×33.0 cm; 14 pages (4 bifolia); Otto-Lilienthal-Museum Bildarchiv, Archiv-ID 00119; copy after Deutsches Museum, HS 626, BN 46906 [11]

From the measured times, the mean velocity over n turns is:

$$V = \frac{2\,\pi\,R\,n}{\Delta t}. \tag{4.1}$$

From now on the number of turns is fixed to $n = 2$.

For different runs, different velocities and masses are considered. Installing the wings increases the drag of the system. Therefore, applying the same mass m to the two configurations yields different velocities: V_w in the wing configuration, and V_a in the empty one, with $V_\mathrm{a} > V_\mathrm{w}$.

To reach the same speed V_w in the empty configuration, a smaller mass m' is required, hence $m' < m$.

Because the arc length over n turns is the same, $s = 2\,\pi\,R\,n$, the different velocities and times satisfy:

$$V_\mathrm{w} = \frac{2\,\pi\,R\,n}{t_\mathrm{w}}, \qquad V_\mathrm{a} = \frac{2\,\pi\,R\,n}{t_\mathrm{a}}, \tag{4.2}$$

and therefore:

$$\frac{V_\mathrm{w}}{V_\mathrm{a}} = \frac{t_\mathrm{a}}{t_\mathrm{w}}. \tag{4.3}$$

Considering the mean velocity while the apparatus is still accelerating introduces uncertainty. Nonetheless, for historical fidelity, the two-turn mean is adopted here; in Sections 5.2–5.3 this definition is compared with alternative speed estimates.

4.2. Lilienthal's wing drag derivation

From now on, by symmetry (the same mass is applied on both sides of the system), relations are written for a single side, yielding the correct drag for one wing.

4.2.1. Torque balance

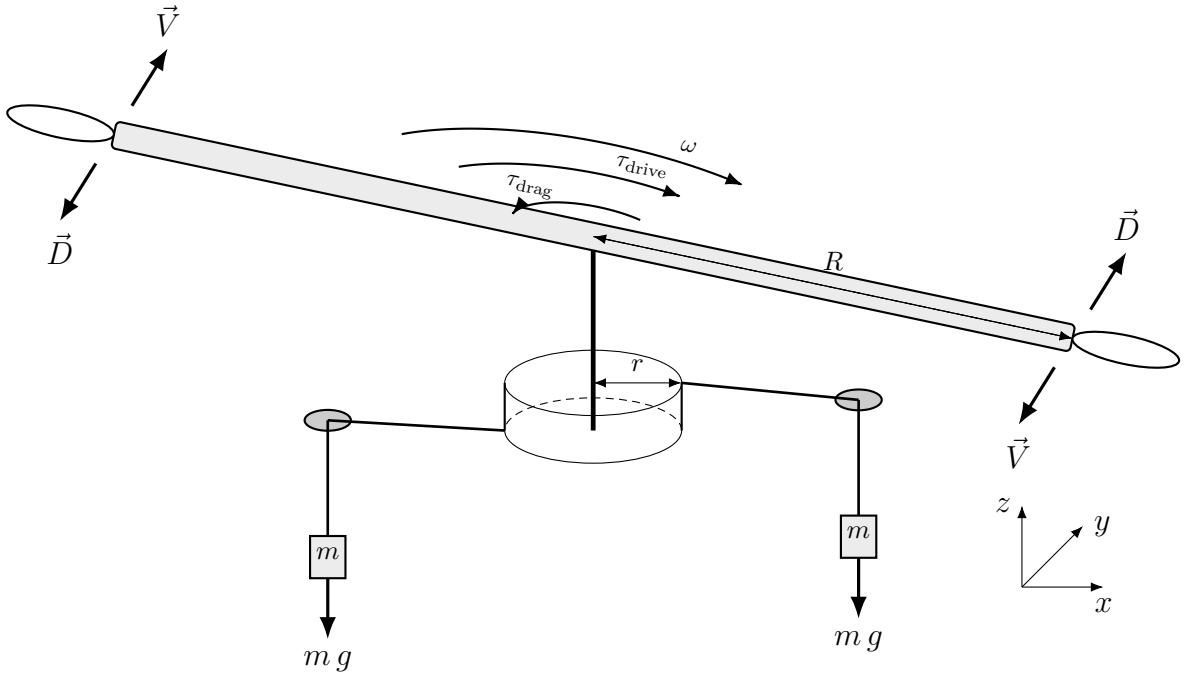

Figure 4.2: Apparatus operation and applied torques. Driving torque $\tau_{\text{drive}} = 2\,m\,g\,r$; resisting (drag) torque $\tau_{\text{drag}} = 2\,D\,R$

At first, the system is considered ideal, without friction, since it is still unclear how Lilienthal treated frictional losses.

Under these conditions, torque equilibrium about the vertical shaft, the apparatus center, gives:

$$D\,R = m\,g\,r \tag{4.4}$$

where D is the total tip-equivalent resisting force. It represents a single resultant placed at the tip whose moment about the shaft equals the net resisting torque of the system [26].

From this torque balance, the tip-equivalent resisting force D in each configuration equals the applied tip-equivalent weight, scaled by the radius ratio r/R:

$$D_{\text{a}}(V_{\text{w}}) = m'\,g\,\frac{r}{R}, \tag{4.5}$$

$$D_{\text{a}}(V_{\text{a}}) = m\,g\,\frac{r}{R}, \tag{4.6}$$

$$D_{\text{a+w}}(V_{\text{w}}) = m\,g\,\frac{r}{R}. \tag{4.7}$$

4.2.2. Wing drag definition

The wing drag is defined as the difference between the total drag in wings configuration and the total drag in empty configuration, at the same speed:

$$D_{\mathrm{w}}(V) = D_{\mathrm{a+w}}(V) - D_{\mathrm{a}}(V)\,. \tag{4.8}$$

Evaluating at the paired speed V_{w} for both cases, and substituting the torque balances 4.5–4.7, results in:

$$D_{\mathrm{w}}(V_{\mathrm{w}}) = D_{\mathrm{a+w}}(V_{\mathrm{w}}) - D_{\mathrm{a}}(V_{\mathrm{w}}) = (m - m')\,g\,\frac{r}{R}. \tag{4.9}$$

4.2.3. Arm drag coefficient

The goal is now to link clearly the two hanging masses, m and m'. As stated, m yields V_{w} in the wings-on configuration and V_{a} in the empty (arms-only) case, while m' yields V_{w} in the empty case.

Considering the empty configuration, the geometry is the same (same rods, same incidence), and for the actual Reynolds-number range, similar for all test cases (Sec. 4.2.3), the arm drag scales with the aerodynamic pressure ($D_{\mathrm{a}} \propto V^2$), with a constant coefficient $C_{D,\mathrm{a}}$ [14]:

$$D_{\mathrm{a}}(V) = \tfrac{1}{2}\,\rho\,V^2\,S\,C_{D,\mathrm{a}}. \tag{4.10}$$

Therefore:

$$C_{D,\mathrm{a}} = \frac{D_{\mathrm{a}}(V_{\mathrm{w}})}{\frac{1}{2}\,\rho\,V_{\mathrm{w}}^2\,S} = \frac{D_{\mathrm{a}}(V_{\mathrm{a}})}{\frac{1}{2}\,\rho\,V_{\mathrm{a}}^2\,S}. \tag{4.11}$$

Substituting the torque-balance Equations 4.5–4.6 for $D_{\mathrm{a}}(V_{\mathrm{w}})$ and $D_{\mathrm{a}}(V_{\mathrm{a}})$ gives:

$$C_{D,\mathrm{a}} = \frac{m'\,g\,\frac{r}{R}}{\frac{1}{2}\,\rho\,V_{\mathrm{w}}^2\,S} = \frac{m\,g\,\frac{r}{R}}{\frac{1}{2}\,\rho\,V_{\mathrm{a}}^2\,S}. \tag{4.12}$$

The relation between the two masses, using also the kinematic Equation 4.3, is:

$$m' = m\left(\frac{V_{\mathrm{w}}}{V_{\mathrm{a}}}\right)^2 = m\left(\frac{t_{\mathrm{a}}}{t_{\mathrm{w}}}\right)^2. \tag{4.13}$$

Reynolds-number range Tested tip speeds span approximately $V \in [3,\,12]$m/s (min-max); the wing chord is $c = 0.4\,\mathrm{m}$, span $1.8\,\mathrm{m}$, and apparatus radius $R = 3.5\,\mathrm{m}$. The

Reynolds number is computed as:

$$\mathrm{Re} = \frac{\rho\, V\, c}{\mu}. \tag{4.14}$$

With standard-air values $\rho \approx 1.225\,\mathrm{kg/m^3}$ and $\mu \approx 1.8 \times 10^{-5}\,\mathrm{Pa\,s}$ [27], this gives

$$\mathrm{Re}(3\,\mathrm{m/s}) \approx 8.17 \times 10^4, \qquad \mathrm{Re}(12\,\mathrm{m/s}) \approx 3.27 \times 10^5,$$

so over the tested envelope $V \in [3, 15]\,\mathrm{m/s}$ one has $\mathrm{Re} \in [\,8.2 \times 10^4,\, 3.3 \times 10^5]$. Within this range, $C_{D,\mathrm{a}}$ is taken constant.

4.2.4. Historical note on Smeaton coefficient

In modern aerodynamics lift and drag are expressed through the dynamic pressure $q = \frac{1}{2}\,\rho\, V^2$, and scaled through their respective coefficients. C_L and C_D depend on angle of attack α, Reynolds number Re, Mach number Ma, and geometry; Ma effects are negligible in Lilienthal's case because the flow is in a low-subsonic range [14]:

$$D = q\, S\, C_D = \tfrac{1}{2}\,\rho\, V^2\, S\, C_D, \tag{4.15}$$

$$L = q\, S\, C_L = \tfrac{1}{2}\,\rho\, V^2\, S\, C_L. \tag{4.16}$$

At the end of the 19th century, it was common to write the "air resistance" (drag at normal incidence, 90°) using the Smeaton coefficient k:

$$D = k\, S\, V^2. \tag{4.17}$$

Importantly, k is a constant factor for a given unit system; it does not depend on S or V. As seen in Section 2.5.3, Lilienthal adopted a value of

$$k = 0.13\,\frac{\mathrm{kgf}}{\mathrm{m^2\,(m/s)^2}}.$$

Lilienthal's idea was to normalize the measured forces by the drag at 90° to obtain ratios that now are interpreted as drag coefficient C_D, and, by applying this reduction also to the lift , lift coefficient C_L. Although he stated in his book that he actually adopted Smeaton's equation [2, Ch. 19-28], there is still historical debate about how he performed this normalization (see Anderson [8]):

1. he treated the value k as generally "accepted", as noted and explained in [2, Ch. 5],

and reduced all measurements with Equation 4.17;

2. he normalized directly by the measured drag at 90° of his test wing; this measurement could also be viewed as an empirical check on k, but k is not required explicitly in the reduction.

Thus, for his derivation, the $C_{D,\mathrm{a}}$ (and, in general, any C_{D}) relation is the same as the modern one 4.12, but with k in place of the dynamic pressure term $\frac{1}{2}\rho$:

$$D = k\,S\,V^2\,C_{\mathrm{D}}, \tag{4.18}$$

$$C_{D,\mathrm{a}} = \frac{m'\,g\,\frac{r}{R}}{k\,S\,V_{\mathrm{w}}^2} = \frac{m\,g\,\frac{r}{R}}{k\,S\,V_{\mathrm{a}}^2}. \tag{4.19}$$

The constant terms cancel when comparing the same geometry at two speeds, yielding the same result obtained in Equation 4.13.

4.2.5. Derivation result

Knowing the relation between m and m' (Eq. 4.13), the kinematic relation (Eq. 4.3), and substituting in the wing drag D_{w} (Eq. 4.9), it is obtained:

$$\begin{aligned} D_{\mathrm{w}}(V_{\mathrm{w}}) = D_{\mathrm{a+w}}(V_{\mathrm{w}}) - D_{\mathrm{a}}(V_{\mathrm{w}}) = (m - m')\,g\,\frac{r}{R} = \\ = m\,g\,\frac{r}{R} - m\,g\,\left(\frac{V_{\mathrm{w}}}{V_{\mathrm{a}}}\right)^2\,\frac{r}{R} = m\,g\,\frac{r}{R}\left[1 - \left(\frac{V_{\mathrm{w}}}{V_{\mathrm{a}}}\right)^2\right] \end{aligned} \tag{4.20}$$

defining the equation adopted by Lilienthal in his notes [11]

$$D_{\mathrm{w}}(V_{\mathrm{w}}) = m\,g\,\frac{r}{R}\left[1 - \left(\frac{t_{\mathrm{a}}}{t_{\mathrm{w}}}\right)^2\right]. \tag{4.21}$$

4.3. Lilienthal's drag derivation with friction

It is also possible to derive the equation Lilienthal used by introducing a friction term measured on his apparatus. As he wrote, "the horizontal component of the air pressure was arrived at by reducing the propelling weight for the centres of air pressure of the surfaces, after deducting the air resistance due to the arms only, and the frictional loss which was experimentally determined beforehand" [2, Ch. 19].

While Equation 4.21 provides the no-friction result, there remains uncertainty about how Lilienthal treated and measured friction. Therefore, some assumptions need to be made.

4.3.1. Assumptions on friction

1. Lilienthal probably computed the frictional loss as the mass that was able to put the entire system in motion, like a propelling weight correction.
2. Because drag does not come into play at start-up ($V = 0\,\mathrm{m/s}$ and $D \propto V^2$), the minimum mass to put the system in motion should be the same for both the wings and the empty cases [14].
3. Over the low-speed regime considered, device friction is approximated as a speed-independent (Coulomb) torque.

Accordingly, m_f is modeled as a constant Coulomb-type torque and expressed as an equivalent hanging mass.

4.3.2. Torque balance

Considering only one mass m_f for any case, the torque balance with respect to the shaft can be written as:

$$D\,R = m\,g\,r - m_\mathrm{f}\,g\,r. \tag{4.22}$$

For the three cases (empty at $V = V_\mathrm{w}$, empty at $V = V_\mathrm{a}$, and wings at $V = V_\mathrm{w}$), torque balance gives:

$$D_\mathrm{a}(V_\mathrm{w}) = (m' - m_\mathrm{f})\,g\,\frac{r}{R}, \tag{4.23}$$

$$D_\mathrm{a}(V_\mathrm{a}) = (m - m_\mathrm{f})\,g\,\frac{r}{R}, \tag{4.24}$$

$$D_\mathrm{a+w}(V_\mathrm{w}) = (m - m_\mathrm{f})\,g\,\frac{r}{R}. \tag{4.25}$$

From here, the steps follow the same sequence as in the no-friction case.

4.3.3. Wing drag definition

$$D_\mathrm{w}(V_\mathrm{w}) = D_\mathrm{a+w}(V_\mathrm{w}) - D_\mathrm{a}(V_\mathrm{w}) = \Big[(m - m_\mathrm{f}) - (m' - m_\mathrm{f})\Big]\,g\,\frac{r}{R} = (m - m')\,g\,\frac{r}{R}. \tag{4.26}$$

4.3.4. Arm drag coefficient

$$C_{D,\mathrm{a}} = \frac{D_{\mathrm{a}}(V_{\mathrm{w}})}{\frac{1}{2}\,\rho\,V_{\mathrm{w}}^2\,S} = \frac{D_{\mathrm{a}}(V_{\mathrm{a}})}{\frac{1}{2}\,\rho\,V_{\mathrm{a}}^2\,S}. \tag{4.27}$$

$$C_{D,\mathrm{a}} = \frac{(m' - m_{\mathrm{f}})\,g\,\frac{r}{R}}{\frac{1}{2}\,\rho\,V_{\mathrm{w}}^2\,S} = \frac{(m - m_{\mathrm{f}})\,g\,\frac{r}{R}}{\frac{1}{2}\,\rho\,V_{\mathrm{a}}^2\,S}. \tag{4.28}$$

$$m' = m\left(\frac{V_{\mathrm{w}}}{V_{\mathrm{a}}}\right)^2 + m_{\mathrm{f}}\left[1 - \left(\frac{V_{\mathrm{w}}}{V_{\mathrm{a}}}\right)^2\right] \tag{4.29}$$

4.3.5. Derivation result

From these, the final equation from Lilienthal's drag with also the addition of frictional loss is:

$$\begin{aligned} D_{\mathrm{w}}(V_{\mathrm{w}}) &= D_{\mathrm{a+w}}(V_{\mathrm{w}}) - D_{\mathrm{a}}(V_{\mathrm{w}}) = (m - m')\,g\,\frac{r}{R} = \\ &= \left\{m - \left[m\left(\tfrac{V_{\mathrm{w}}}{V_{\mathrm{a}}}\right)^2 + m_{\mathrm{f}}\left(1 - \left(\tfrac{V_{\mathrm{w}}}{V_{\mathrm{a}}}\right)^2\right)\right]\right\}\,g\,\frac{r}{R} = \\ &= (m - m_{\mathrm{f}})\,g\,\frac{r}{R}\left[1 - \left(\frac{V_{\mathrm{w}}}{V_{\mathrm{a}}}\right)^2\right]. \end{aligned} \tag{4.30}$$

Using also the kinematic in Equation 4.3:

$$D_{\mathrm{w}}(V_{\mathrm{w}}) = (m - m_{\mathrm{f}})\,g\,\frac{r}{R}\left[1 - \left(\frac{t_{\mathrm{a}}}{t_{\mathrm{w}}}\right)^2\right]. \tag{4.31}$$

4.4. Lilienthal's lift derivation

Lilienthal measured the total lift of the rotating system with a counterbalanced lever (Sec. 3.6).

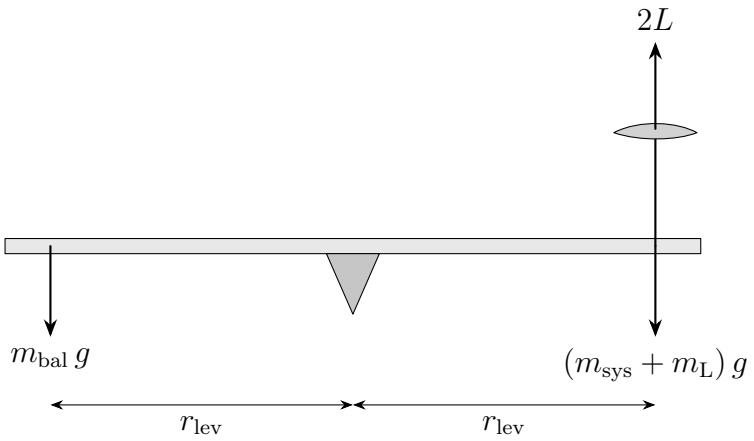

Figure 4.3: Counterbalanced lift lever. Left end: counterweight m_{bal}. Right end: rotating system m_{sys}, added mass in lift balance m_{L} and the two wings that produce lift

The torque balance with respect to the pivot of the lever in steady conditions gives:

$$m_{\mathrm{bal}}\, g\, r_{\mathrm{lev}} - m_{\mathrm{sys}}\, g\, r_{\mathrm{lev}} - m_{\mathrm{L}}\, g\, r_{\mathrm{lev}} + 2\, L\, r_{\mathrm{lev}} = 0. \tag{4.32}$$

Because the lever arms are equal ($r_{\mathrm{lev}} = 90\,\mathrm{cm}$), the counterweight is adjusted so that $m_{\mathrm{bal}} = m_{\mathrm{sys}}$, and the rotating system is symmetric, the lift of one wing is:

$$L = \frac{m_{\mathrm{L}}\, g}{2}. \tag{4.33}$$

As with the drag, $L \propto V^2$. At a fixed incidence α, a larger falling mass (and thus larger tip speed V_{w}) requires a larger m_{L} to rebalance the lever.

This lift determination involves several uncertainties, and some steps are not explicit in Lilienthal's notes (for more detail see Sec. 5.2).

4.5. Coefficient definitions and computation

The following definitions will be adopted for the experimental results (see Sec. 5.2.5) to infer which normalization is most consistent with Lilienthal's procedure.

Unless noted otherwise, coefficients are defined per one wing using the wing area S and the tip speed at the wings V_{w}.

The forces considered are those derived earlier: Equations 4.21–4.33 for the frictionless case, and Equations 4.31–4.33 when friction is included. Friction only affects $D_{\mathrm{w}}(V_{\mathrm{w}})$ through the replacement of m with $(m - m_{\mathrm{f}})$.

Changing the dynamic pressure definition, either following Smeaton or the modern one, gives different coefficients:

$$q = \begin{cases} \frac{1}{2}\,\rho\,V_{\mathrm{w}}^2 & \text{(modern definition)}, \\ k\,V_{\mathrm{w}}^2 & \text{(Smeaton coefficient)}. \end{cases} \tag{4.34}$$

$$C_{\mathrm{D}} = \frac{D_{\mathrm{w}}(V_{\mathrm{w}})}{q\,S}, \qquad C_{\mathrm{L}} = \frac{L(V_{\mathrm{w}})}{q\,S}. \tag{4.35}$$

A reduction based on the Smeaton coefficient is arguably the most faithful to Lilienthal's own statements, as already explained in Section 2.5.3, but it is not the only plausible interpretation. When the Smeaton form is used, k may be set to any historical or modern value from the literature (see Sec. 2.5.3) [20].

Coefficients with normalization by 90° case

Another possibility, mostly discussed by Anderson [8], is that he did not employ the Smeaton coefficient, but instead normalized every force by the wing drag at 90°, considering the tabulated coefficients as force ratios:

$$C_{\mathrm{D}}(\alpha) = \frac{D_{\mathrm{w}}(V_{\mathrm{w}},\,\alpha)}{V_{\mathrm{w}}^2}\,\frac{V_{90^\circ}^2}{D_{\mathrm{w}}(V_{90^\circ},\,90^\circ)}, \qquad C_{\mathrm{L}}(\alpha) = \frac{L(V_{\mathrm{w}},\,\alpha)}{V_{\mathrm{w}}^2}\,\frac{V_{90^\circ}^2}{D_{\mathrm{w}}(V_{90^\circ},\,90^\circ)}. \tag{4.36}$$

If the data at 90° has been taken at a different velocity V_{90°, every force has to be rescaled assuming the proportionality $D \propto V^2$. By construction, $C_{\mathrm{D}}(90^\circ) = 1$ and $C_{\mathrm{L}}(90^\circ) = 0$, matching Lilienthal's Plates [2].

4.6. Alternative empirical formula from the notes

Define the tip-equivalent empty mass as $m_{\mathrm{eq,empty}} = m'\,\frac{r}{R}$. An empirical form consistent with the notes is:

$$D_{\mathrm{w}}(V_{\mathrm{w}}) = (m - m_{\mathrm{eq,\,empty}})\,g\,\frac{r}{R}\left[1 - \left(\frac{t_{\mathrm{a}}}{t_{\mathrm{w}}}\right)^2\right]. \tag{4.37}$$

This expression is not derived and it may be inconsistent depending on the different equivalent-mass convention adopted. Since the surviving notes do not make clear how Lilienthal accounted for friction, it is included only because it matches the empty-configuration data in notes (Fig. 4.1) and the corresponding empty graph (Fig. 5.10) [11].

5 | Experimental Tests and Results: *Rundlaufapparat*

5.1. Kinematics and velocity characterization

Before reproducing Lilienthal's experiments, the apparatus is characterized kinematically to verify reachable speeds and the extent to which a quasi-steady regime can be approached.

5.1.1. Experimental setup

The *Rundlaufapparat* reconstruction is described in Chapter 3.

Equipment:

- Piher PSC-360 Hall-effect end-of-shaft rotary sensor (analog, ratiometric) [28];
- PLA contact wheel mounted on the sensor shaft and a thin rubber band to ensure grip on the outer rim of the drive pulley (Figs. 5.1–A.4);
- Dewetron acquisition with Dewesoft;
- driving weights;
- a pole to rewind the ropes and set the start position.

5.1.2. Sensor and signal model

The PSC-360 provides an analog ratiometric output: the signal spans approximately 10%–90% of V_{ref} over 0°–360° [28]. These features make it well suited to the present application in a dusty workshop environment. Define the dimensionless voltage ratio:

$$\eta \equiv \frac{V_{\mathrm{sig}}}{V_{\mathrm{ref}}}. \tag{5.1}$$

The transfer used here is





Figure 5.1: Velocity measurement setup

$$\theta_s = 360^\circ \frac{\eta - 0.10}{0.80} \quad \text{for} \quad 0.10 \leq \eta \leq 0.90, \tag{5.2}$$

which removes sensitivity to supply variation through the ratio η. A PLA disk of diameter $d_{\text{sens}} = 60\,\text{mm}$ is fitted to the shaft; a 1 mm thick rubber band increases the effective diameter to $d_{\text{sens}} = 62\,\text{mm}$. The contact runs on the pulley outer rim of diameter $d_{\text{pulley,outer}} = 350\,\text{mm}$. The pulley inner groove of diameter $d_{\text{pulley,inner}} = 300\,\text{mm}$ is connected by rope to the drum inner groove of diameter $d_{\text{drum,inner}} = 450\,\text{mm}$. Angles are expressed in degrees throughout; conversion to radians is applied when computing the angular velocity ω and the tangential velocity V.

5.1.3. Contact transmission kinematics (ideal)

Ideal no-slip transmission at each contact gives

$$d_{\text{sens}}\,\mathrm{d}\theta_s = d_{\text{pulley,outer}}\,\mathrm{d}\theta_p, \qquad d_{\text{pulley,inner}}\,\mathrm{d}\theta_p = d_{\text{drum,inner}}\,\mathrm{d}\theta_d, \tag{5.3}$$

where $\mathrm{d}\theta_s$, $\mathrm{d}\theta_p$ and $\mathrm{d}\theta_d$ are respectively the sensor, the pulley and the drum angles. The drum is keyed to the shaft, so $\theta_d = \theta$ (the apparatus/wing rotation angle). Differentiating:

$$\omega(t) = \dot{\theta}(t) = \dot{\theta}_s(t)\,\frac{d_{\text{sens}}}{d_{\text{pulley,outer}}}\,\frac{d_{\text{pulley,inner}}}{d_{\text{drum,inner}}}. \tag{5.4}$$

The wing-tip speed follows as:

$$V(t) = R\,\omega(t) = R\,\dot{\theta}(t) = R\,\dot{\theta}_{\mathrm{s}}(t)\,\frac{d_{\mathrm{sens}}}{d_{\mathrm{pulley,outer}}}\,\frac{d_{\mathrm{pulley,inner}}}{d_{\mathrm{drum,inner}}}. \tag{5.5}$$

With $d_{\mathrm{sens}} = 62\,\mathrm{mm}$, $d_{\mathrm{pulley,outer}} = 350\,\mathrm{mm}$, $d_{\mathrm{pulley,inner}} = 300\,\mathrm{mm}$, $d_{\mathrm{drum,inner}} = 450\,\mathrm{mm}$, the kinematic factor is

$$x_0 = \frac{\theta}{\theta_{\mathrm{s}}} = \frac{d_{\mathrm{sens}}}{d_{\mathrm{pulley,outer}}}\,\frac{d_{\mathrm{pulley,inner}}}{d_{\mathrm{drum,inner}}} \approx 0.1181.$$

Thus, one full apparatus turn corresponds to $1/x_0 \approx 8.47$ sensor turns.

In the actual experiments, non-ideal effects such as rubbing, rope slip, local compliance, and friction are considered and accounted for with a non-ideal factor $\hat{x}$ (see Sec. 5.1.4).

5.1.4. Experimental procedure

The following steps are performed.

Step 1. Sensor calibration. The law in Equation 5.2 is checked quasi-statically. The pulley is stepped through eight positions over the full 0°–360° rotation (spanning the corresponding η range), recording $(V_{\mathrm{sig}}, V_{\mathrm{ref}})$. A least-squares fit

$$\theta = a_0 + a_1\,\eta \tag{5.6}$$

is overlaid on the nominal law. Agreement lies within the device linearity; deviations are negligible relative to timing and geometry uncertainties (Fig. 5.2).

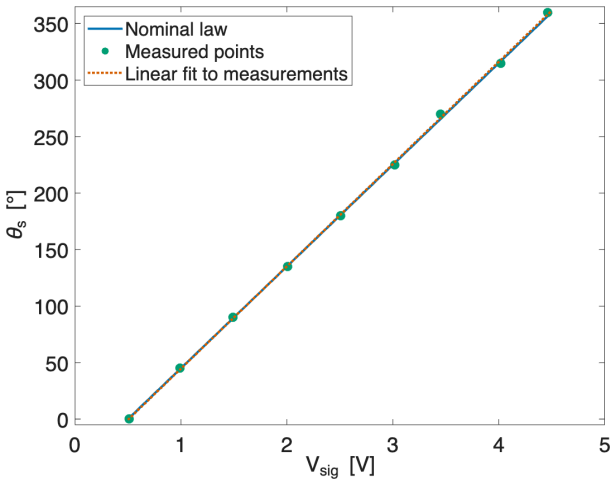

Figure 5.2: PSC-360 calibration

Step 2. Transmission calibration (non-ideal effects). From the ideal computations, one full turn of the apparatus corresponds to about 8.47 turns of the sensor ($x_0 \approx 0.1181$). The transmission is not ideal and several effects can introduce a lag between the drum rotation and the sensor reading:

- slip between rope and pulley,
- slip between pulley and sensor wheel,
- effective diameters modified by rope thickness and local compliance,
- rope stretch and slow creep under load,
- bearing drag and small misalignments,
- out-of-round/eccentric rims and rope layering/crossovers in grooves.

Therefore, it is plausible that the measured transmission ratio

$$x_{\mathrm{tr}} \equiv \frac{\theta}{\theta_{\mathrm{s}}} \tag{5.7}$$

is higher than the ideal x_0 (Eq. 5.4–5.5).

Each drop is configured to produce a prescribed base rotation $B \in \{180^\circ, 360^\circ\}$ of the apparatus (one base turn only). The total sensor angle θ_{s} accumulated while the ropes are tensioned $[t_{\mathrm{in}}, t_{\mathrm{end}}]$ is measured; the per-test ratio is $x_{\mathrm{tr}} = \theta/\theta_{\mathrm{s}}$, where the apparatus rotation is B by design (minor deviations are rounded to B; see Algorithm B.1). The measurement stops when the weights reach the ground, because the ropes become loose and traction is lost. The applied mass and the number of turns are varied to check for possible torque-dependent effects; the global estimate is denoted $\hat{x}$. The wing angle of attack is fixed at $\alpha = 0^\circ$.

Tests carried out:

- 2 tests with $m = 10\,\mathrm{kg}$ targeting $\theta = 180^\circ$;
- 4 tests with $m = 10\,\mathrm{kg}$ targeting $\theta = 360^\circ$;
- 3 tests with $m = 20\,\mathrm{kg}$ targeting $\theta = 360^\circ$.

From these tests, the time histories (t, θ_{s}) are extracted; after converting V_{sig} to θ_{s} and applying the preprocessing described in Section 5.1.5, the non-ideal transmission ratio $x_{\mathrm{tr}} \equiv \theta/\theta_{\mathrm{s}}$ is identified. The procedure uses the windowed angle increments and the known base turns. The global estimate $\hat{x}$ follows Algorithm B.1. The calibrated transmission (per-test x_{tr}, global $\hat{x}$) is used later to map sensor angle to apparatus rotation, and

therefore wing velocities (see Sec. 5.1.6), and to parameterize the kinematic simulation (see Sec. 5.1.7).

Step 3. Actual test. Tests follow Lilienthal's practice of $n = 2$ full turns. With the present drum geometry, only two rotations from rest are feasible. The following combinations of hanging mass m and angle of attack α are tested:

- $\alpha = 0°$ is tested with hanging pairs $m \in \{10, 15, 20\}$ kg;
- $\alpha = 12°$ with $m = 10$ kg;
- $\alpha = 30°$ with $m = 10$ kg.

Step 4. Data processing. From these tests, the data are processed to obtain the angular velocity history $\omega(t)$ and the tip speed $V(t) = R\,\omega(t)$; see Section 5.1.5 for processing and Section 5.1.6 for results.

Step 5. Kinematic model. Based on the apparatus data and results, a code is implemented to simulate each condition (m, α), aiming to reproduce the measured kinematics (see Sec. 5.1.7).

5.1.5. Data reduction to ω and V

Test data are acquired with Dewetron and saved via Dewesoft. Signals are converted from volts (V) to angle in degrees (°) using Equation 5.2; basic issues (out-of-range samples, spikes, duplicates) are handled during a preprocessing phase in MATLAB. Figure 5.3 summarizes the processing to obtain the angular velocity $\omega_s(t)$ for Steps 2–3. Panel (a) shows the raw angle signal θ_s with the analysis window $[t_{in}, t_{end}]$; panel (b) shows the unwrapped angle inside that window after circular low-pass filtering and resampling.

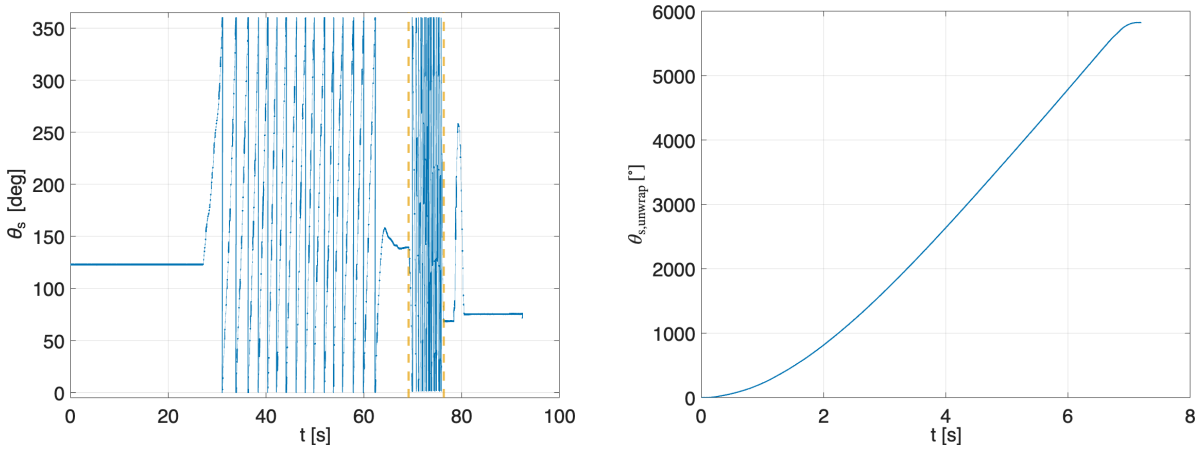

(a) Raw signal with analysis window

(b) Unwrapped angle inside the window

Figure 5.3: Sensor angle processing

The angular velocity is obtained by a Savitzky-Golay time derivative and lightly low-pass filtered to suppress small high-frequency oscillations introduced by noise and differentiation [29].

$$\omega_{\mathrm{s}}(t) = \frac{\mathrm{d}\theta_{\mathrm{s}}}{\mathrm{d}t} \ [^\circ/\mathrm{s}], \qquad \omega_{\mathrm{s,rad}}(t) = \omega_{\mathrm{s}}(t)\,\frac{\pi}{180} \ [\mathrm{rad/s}]. \tag{5.8}$$

The drum angular velocity, and thus the wings, follows from the transmission:

$$\omega(t) = \hat{x}\,\omega_{\mathrm{s,rad}}(t), \tag{5.9}$$

where $\hat{x}$ is obtained by Algorithm B.1.
For the ideal case, $x_0 = (d_{\mathrm{sens}}/d_{\mathrm{pulley,outer}})\,(d_{\mathrm{pulley,inner}}/d_{\mathrm{drum,inner}})$ replaces $\hat{x}$ in Equation 5.9. The wing speed is:

$$V(t) = R\,\omega(t) = R\,\hat{x}\,\omega_{\mathrm{s,rad}}(t). \tag{5.10}$$

5.1.6. Results: velocity experiments

Unless noted otherwise, all ω and V shown here are computed from $\theta_{\mathrm{s}}(t)$ using the calibrated transmission $\hat{x} = 0.1250$ (Algorithm B.1). The ideal ratio is $x_0 = 0.1181$ and is used only for comparison in Section 5.1.6 (transmission effects). Small offsets in trace start times arise from the manual release; curves are shifted to align the onset of motion.

Repeatability at $\alpha = 12°$

Three nominally identical tests at $(m, \alpha) = (10\,\text{kg}, 12°)$ are overlaid. Run-to-run variability is low: peak speed and mean speed over the window differ by at most 3.35 % and 1.53 %, respectively. Comparable repeatability is observed for the other conditions.

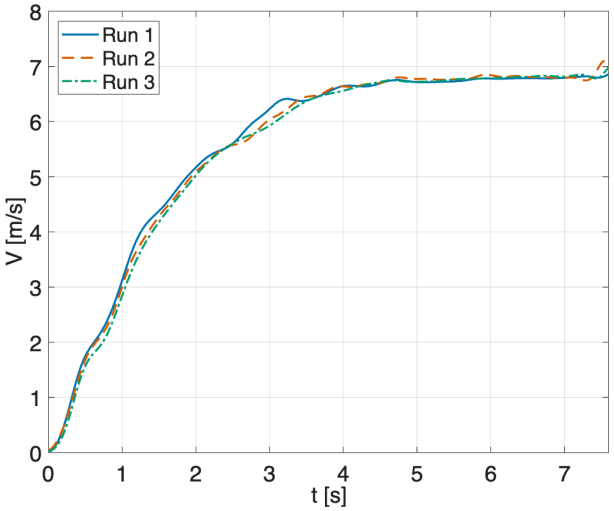

Figure 5.4: $V(t)$ for three runs at $(10\,\text{kg}, 12°)$

Effect of mass at fixed angle ($\alpha = 0°$)

One representative run per mass is shown. Increasing m increases both peak and mean V, and shortens the drop time of the weights. For $m = 10\,\text{kg}$, a short quasi-steady plateau appears near the end of the window; for $m = 20\,\text{kg}$, the velocity $V(t)$ continues to rise over the available drop, so a strict steady regime is not reached. Relative to Lilienthal's operating range (velocities around 6 m/s were frequently noted in his records [11]), the $m = 10\,\text{kg}$ case remains in that range for more than 2 s.

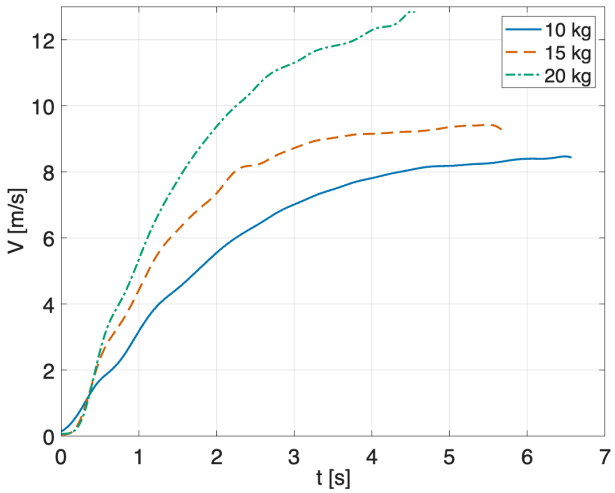

Figure 5.5: $V(t)$ at $\alpha = 0°$ for one representative run at each mass (10, 15, 20 kg)

Effect of angle of attack at fixed mass ($m = 10\,\text{kg}$)

One representative run per angle is shown, with $\alpha \in \{0°, 12°, 30°\}$. Increasing the angle of attack increases aerodynamic drag and reduces both peak and mean V; it also lengthens the run (longer drop time of the weights). During the first 1–2 s the acceleration is similar across angles because, at low speeds, aerodynamic torque is small ($D \propto V^2$) and the dynamics are dominated by the applied torque and inertia. At higher α the end of the run becomes fully steady: for 0° the plateau is short and not fully steady, for 12° the apparatus rotates at approximately constant speed for about 4 s, and for 30° for about 6 s.

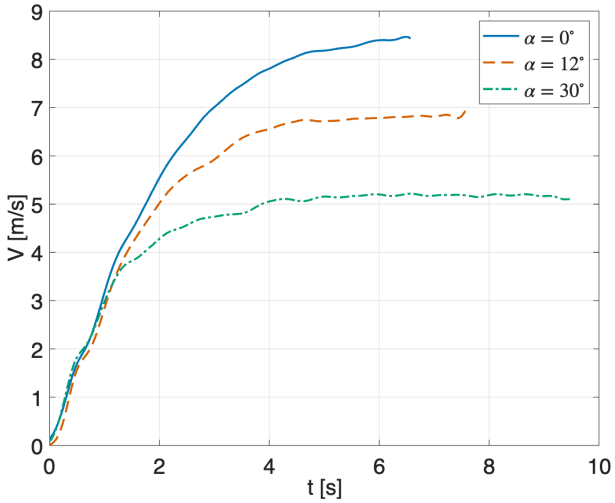

Figure 5.6: $V(t)$ at $m = 10\,\text{kg}$ for one representative run at each α (0°, 12°, 30°)

Transmission calibration: results and application

Per-test transmission ratios are defined as $x_{\mathrm{tr},j} \equiv \theta_j/\theta_{\mathrm{s},j}$ over the drop windows $[t_{\mathrm{in},j}, t_{\mathrm{end},j}]$ (Step 2). A robust dispersion is shown as a band $\pm\sigma_{\mathrm{MAD}}$, with

$$\mathrm{MAD} = \mathrm{median}_j\big|x_{\mathrm{tr},j} - \mathrm{median}_\ell(x_{\mathrm{tr},\ell})\big|, \qquad \sigma_{\mathrm{MAD}} = 1.4826\,\mathrm{MAD}. \tag{5.11}$$

MAD is the median absolute deviation, a robust measure of spread; the factor 1.4826 rescales MAD to the standard-deviation scale for Gaussian data.

The global fit in Algorithm B.1 yields a single value for all runs, $\hat{x} = 0.1250$, larger than the ideal $x_0 = 0.1181$ (+5.8%). Figure 5.7 shows the per-test $x_{\mathrm{tr},j}$ together with x_0, $\hat{x}$, the sample median and the robust band $\pm\sigma_{\mathrm{MAD}}$.

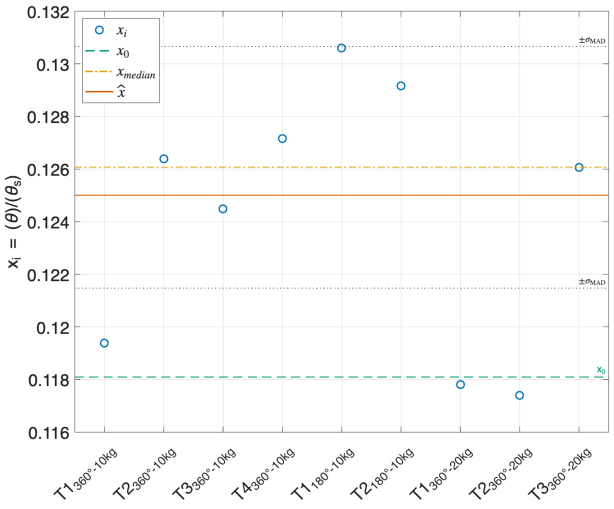

Figure 5.7: Per-test transmission ratios $x_{\mathrm{tr},j}$ with ideal x_0 and calibrated $\hat{x}$

Physically, $\hat{x} > x_0$ is consistent with small slip at the contacts and effective diameter changes due to rope thickness/compliance and minor eccentricities. Define the calibration gain (ratio to ideal) $f \equiv \hat{x}/x_0 = 1.0584$. The equivalent slip

$$s_{\mathrm{eq}} \equiv 1 - \frac{x_0}{\hat{x}} = 5.52\%,$$

means the sensor reports $\approx 5.5\%$ less angle than the ideal no-slip geometry ($0.0552 \times 720° \approx 40°$ over two turns). The calibrated transmission is used throughout to map sensor angle/velocity to apparatus angle/velocity, and thus to wing speed V (Sec. 5.1.5, Sec. 5.1.6). For reference, Figure 5.8 compares $V(t)$ reconstructed with x_0 and with $\hat{x}$ on a representative run; as expected from $f \geq 1$, the calibrated curves are higher by 5.84 % in both peak and mean over the same window.

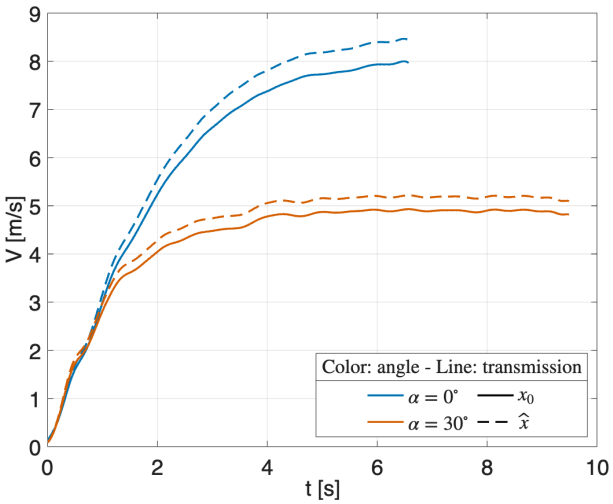

Figure 5.8: Comparison of $V(t)$ reconstructed with ideal x_0 and calibrated $\hat{x}$

Non-ideal mechanisms are listed in Step 2 (Sec. 5.1.4).

Summary. The objective of these experiments was to verify that the reconstructed *Rundlaufapparat* delivers the intended kinematic behavior under representative loads and angles of attack.

1. Achievable speeds. The apparatus attains wing speeds in Lilienthal's operating range (order of 6 m/s), with multi-second intervals inside that band for suitable settings.
2. Repeatability. Run-to-run variability is low when the procedure is followed: for (10 kg, 12°), peak V and window-mean $\overline{V}$ differ by at most 3.35% and 1.53%, respectively, with comparable repeatability across other conditions.
3. Quasi-steady rotation. A clear near-constant-speed plateau emerges at higher angles of attack for several seconds; at low α and higher loads, the motion remains predominantly acceleration-dominated over the available drop.

5.1.7. Model implementation and validation

A MATLAB model (Appendix D) is implemented to reproduce the whirling-arm apparatus as a single degree of freedom in $\omega(t)$, driven by hanging masses and opposed by quadratic aerodynamic drag and transmission losses. The model includes rigid-body inertia (drum, shaft, pulleys, arms, rods, wings, cables), capstan attenuation in the rope-pulley contact and Coulomb (dry) friction at the pulley pin, plus radius-weighted aerodynamic torques. Secondary effects are neglected (rope mass/inertia and bending hysteresis, viscous bearing losses, slip beyond the capstan law, aerodynamic drag on the hanging masses and on the

vertical rope). The model is used to analyze the measured results and to generate velocity traces for different settings (Sec. 5.3).

Physical blocks

Rigid inertia. Stacked wooden disks composing the drum, a hollow shaft, pulleys (mapped by $i_{\text{ratio}}^2 = (r_{\text{drum,inner}}/r_{\text{pulley,inner}})^2$), four radial arms, two vertical rods at the center of the arms and two at the tips, two wings, and all bracing cables:

$$J_{\text{rigid}} = I_{\text{drum}} + I_{\text{shaft}} + I_{\text{pulleys}}\, i_{\text{ratio}}^2 + I_{\text{arms,rad}} + I_{\text{arms,vert}} + I_{\text{wings}} + I_{\text{cables}}. \tag{5.12}$$

Only the generic formulas appear in the main text; the per-component expressions are tabulated in Appendix C.

Hanging masses. Mapped to the shaft by the drum radius,

$$J_{\text{masses}} = 2\, m\, r_{\text{drum,inner}}^2, \tag{5.13}$$

and therefore the total effective inertia is

$$J_{\text{eff}} = J_{\text{rigid}} + J_{\text{masses}}. \tag{5.14}$$

Torque transmission. Each mass satisfies $m\,g - T_{\text{in}} = m\,a$ with $a = r_{\text{drum,inner}}\,\dot{\omega}$. Hence, for one side

$$T_{\text{in}} = m\left(g - r_{\text{drum,inner}}\,\dot{\omega}\right), \qquad k_{\text{cap}} = e^{-\mu_{\text{rope}}\,\theta_{\text{wrap}}}, \qquad T_{\text{out}} = k_{\text{cap}}\,T_{\text{in}},$$

and the torque on one pulley is $(T_{\text{in}} - T_{\text{out}})\, r_{\text{pulley,inner}} = (1 - k_{\text{cap}})\, T_{\text{in}}\, r_{\text{pulley,inner}}$ [30]. Mapping to the shaft by $i_{\text{ratio}} = r_{\text{drum,inner}}/r_{\text{pulley,inner}}$ and summing $n_{\text{pulley}} = 2$ identical sides gives the drive torque at the shaft

$$\begin{aligned} \tau_{\text{drive}}(\omega) &= 2\,(1 - k_{\text{cap}})\, T_{\text{in}}\, r_{\text{pulley,inner}}\, i_{\text{ratio}} \\ &= 2\,(1 - k_{\text{cap}})\, m\, r_{\text{drum,inner}}\left(g - r_{\text{drum,inner}}\,\dot{\omega}\right). \end{aligned} \tag{5.15}$$

Bushing dry friction at the pulley. The reaction at the pulley pin from the two rope branches is

$$N = \sqrt{T_{\text{in}}^2 + T_{\text{out}}^2 - 2T_{\text{in}}T_{\text{out}}\cos\theta_{\text{wrap}}} = T_{\text{in}}\,C_{\text{wrap}}, \quad C_{\text{wrap}} = \sqrt{1 + k_{\text{cap}}^2 - 2k_{\text{cap}}\cos\theta_{\text{wrap}}}. \tag{5.16}$$

The Coulomb torque at one pulley is $\mu_b\, N\, r_{\text{pulley,inner}}$ (dry friction [31]); mapped to the shaft and summed:

$$\begin{aligned}\tau_{\text{friction}} &= n_{\text{pulley}}\,\mu_b\,C_{\text{wrap}}\,T_{\text{in}}\,r_{\text{pulley,inner}}\,i_{\text{ratio}} \\ &= n_{\text{pulley}}\,\mu_b\,C_{\text{wrap}}\,r_{\text{pulley,inner}}\,i_{\text{ratio}}\,m\big(g - r_{\text{drum,inner}}\,\dot{\omega}\big).\end{aligned} \tag{5.17}$$

Aerodynamic drag torque. All elements contribute a quadratic torque $D\,\omega|\omega|$. The generic radius-weighted contribution of a slender cylinder of diameter d spanning $r \in [a, b]$ is

$$D_{\text{cyl}}(a,b) \;=\; \tfrac{1}{8}\,\rho\,C_{\text{D,cyl}}\,d\,\big(b^4 - a^4\big), \tag{5.18}$$

which we use for arms and cables (see Appendix C). Wings are modeled as

$$D_{\text{wing}} \;=\; \tfrac{1}{2}\,\rho\,S_{\text{wing}}\,C_{\text{D,wing}}\,R^3, \tag{5.19}$$

and therefore the total drag is

$$D_{\text{tot}} \;=\; D_{\text{arms}} + D_{\text{cables}} + 2\,D_{\text{wing}}. \tag{5.20}$$

Here $C_{\text{D,wing}}$ is treated as an assigned case-specific value representing the intended α at the test Reynolds number.

Governing equations

With $J_{\text{eff}} = J_{\text{rigid}} + J_{\text{masses}}$ and $\tau_{\text{drag}} = D_{\text{tot}}\,\omega|\omega|$, the angular momentum balance is:

$$J_{\text{eff}}\,\dot{\omega} = \tau_{\text{drive}}(\omega) - \tau_{\text{friction}}(\omega) - \tau_{\text{drag}}(\omega). \tag{5.21}$$

Using Equations 5.15–5.17 with two equal masses m (as in the actual experiments) and inner radii $r_{\text{drum,inner}}, r_{\text{pulley,inner}}$, collecting the $\dot{\omega}$ terms gives

$$\begin{aligned}\underbrace{\Big[J_{\text{eff}} + 2\,m\,(1-k_{\text{cap}})\,r_{\text{drum,inner}}^2 - 2\,m\,\mu_b\,C_{\text{wrap}}\,r_{\text{pulley,inner}}\,i_{\text{ratio}}\,r_{\text{drum,inner}}\Big]}_{\hat{J}\ \text{(effective inertia)}}\,\dot{\omega} \;=\\ =\ \underbrace{2\,m\,g\Big[(1-k_{\text{cap}})\,r_{\text{drum,inner}} - \mu_b\,C_{\text{wrap}}\,r_{\text{pulley,inner}}\,i_{\text{ratio}}\Big]}_{\tau_g\ \text{(gravity drive)}} - D_{\text{tot}}\,\omega|\omega|.\end{aligned} \tag{5.22}$$

Define the state $x = [\theta,\ \omega,\ z]^T$ with θ the rotation angle and z the remaining drop height. The state equations are:

$$\begin{cases}\dot{\theta} = \omega & \text{(5.23a)}\\ \dot{\omega} = \dfrac{\tau_g - D_{\text{tot}}\,\omega|\omega|}{\hat{J}} & \text{(5.23b)}\\ \dot{z} = -r_{\text{drum,inner}}\,\omega & \text{(5.23c)}\end{cases}$$

with initial conditions $\theta(0) = 0$, $\omega(0) = 0$, $z(0) = h$, and integration stops when $z(t) = 0$.

Closed-form benchmark

Assuming no sign change ($\omega \geq 0$), define

$$a = \frac{\tau_g}{\hat{J}}, \qquad b = \frac{D_{\text{tot}}}{\hat{J}}. \tag{5.24}$$

Then the angular speed with $\omega(0) = \omega_0$ solves

$$\omega(t) \;=\; \sqrt{\frac{a}{b}}\ \tanh\left[\sqrt{ab}\,t \;+\; \operatorname{atanh}\Big(\frac{\omega_0}{\sqrt{a/b}}\Big)\right]. \tag{5.25}$$

Equivalently, with

$$\tau_c = \frac{1}{\sqrt{ab}}, \qquad \omega_\infty = \sqrt{\frac{a}{b}} = \sqrt{\frac{\tau_g}{D_{\text{tot}}}}, \qquad C = \operatorname{atanh}\Big(\frac{\omega_0}{\omega_\infty}\Big),$$

$$\omega(t) \;=\; \omega_\infty\,\tanh\Big(\frac{t}{\tau_c} + C\Big). \tag{5.26}$$

The exact solutions of the grouped ODE (Eq. 5.22) are:

$$\begin{cases} \omega(t) = \omega_\infty \tanh\left(\frac{t}{\tau_c} + C\right) & (5.27a) \\ \theta(t) = \omega_\infty \tau_c \left[\ln\left(\cosh(\frac{t}{\tau_c} + C)\right) - \ln\left(\cosh(C)\right)\right] & (5.27b) \\ z(t) = h - r_{\text{drum,inner}}\, \omega_\infty \tau_c \left[\ln\left(\cosh(\frac{t}{\tau_c} + C)\right) - \ln\left(\cosh(C)\right)\right]. & (5.27c) \end{cases}$$

The tip speed is $V(t) = R\,\omega(t)$ with asymptote $U_\infty = R\,\omega_\infty$.

Starting from rest, as in the actual experiments, $\omega(0) = 0$ so $C = 0$:

$$\begin{cases} \omega(t) = \omega_\infty \tanh\left(\frac{t}{\tau_c}\right) & (5.28a) \\ \theta(t) = \omega_\infty \tau_c \ln\left(\cosh(\frac{t}{\tau_c})\right) & (5.28b) \\ z(t) = h - r_{\text{drum,inner}}\, \omega_\infty \tau_c \ln\left(\cosh(\frac{t}{\tau_c})\right). & (5.28c) \end{cases}$$

Inputs and identification

The test-varying inputs are the mass per side m, the angle of attack α, and the associated $C_{\text{D,wing}}(\alpha, \text{Re})$. Transmission-loss parameters are the capstan factor $k_{\text{cap}} = e^{-\mu_{\text{rope}}\theta_{\text{wrap}}}$ and the dry-friction coefficient at the pulley pin μ_b (entering through C_{wrap}). These are identified once from low-drag runs (wings off or $\alpha \approx 0°$) and then kept fixed for all cases.

Validation against experiments

The MATLAB model (Appendix D) was compared with the measured runs. It reproduces well the dependence on angle of attack α. At higher masses (see Fig. 5.9b for the $m = 20\,\text{kg}$ case), the final velocity and the drop time are captured accurately; the larger differences appear in the initial acceleration, reflecting the practical difficulty of a perfectly clean release and precise timing. Figure 5.9 shows four representative overlays.

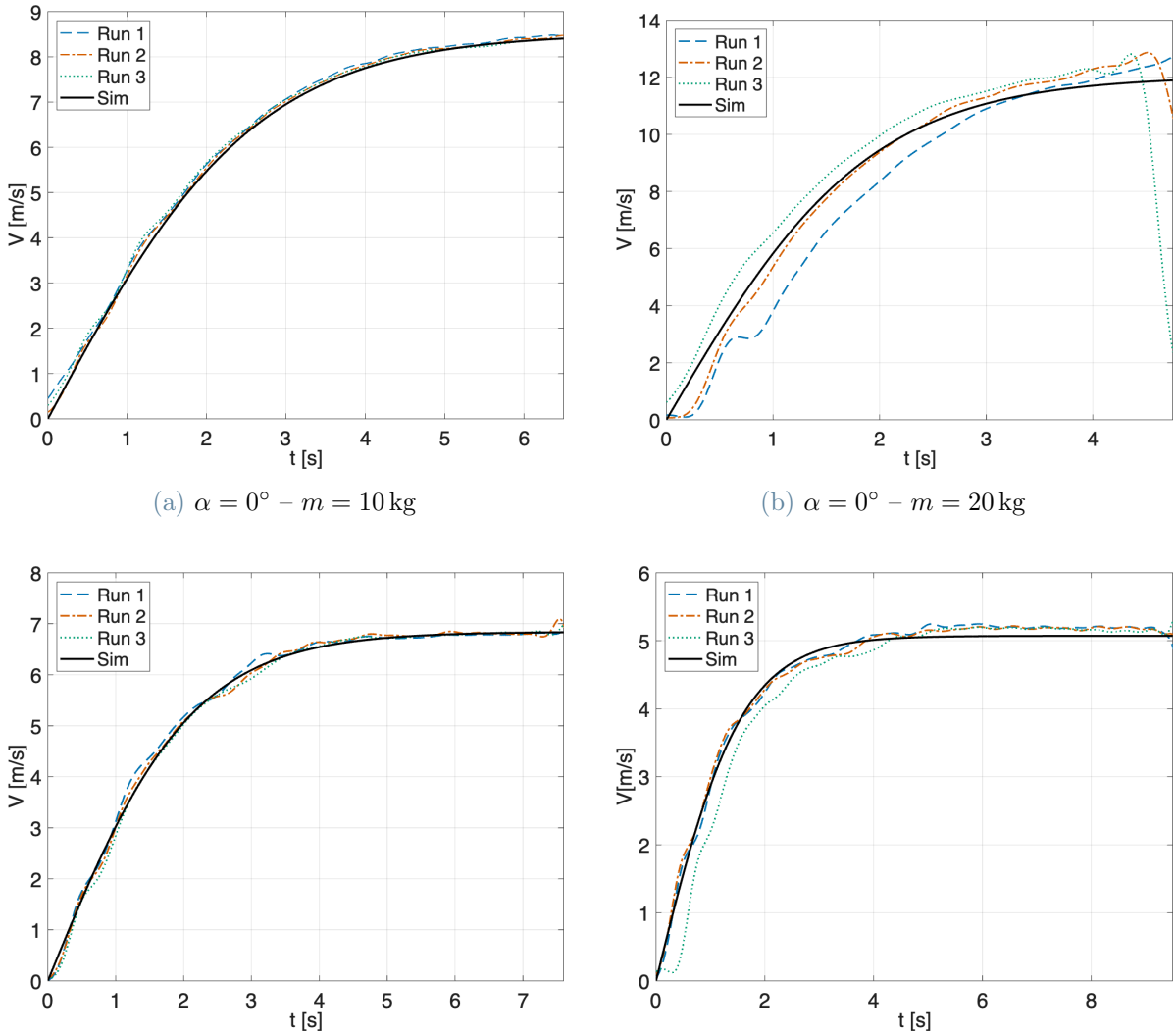

(a) $\alpha = 0° - m = 10\,\text{kg}$

(b) $\alpha = 0° - m = 20\,\text{kg}$

(c) $\alpha = 12° - m = 10\,\text{kg}$

(d) $\alpha = 30° - m = 10\,\text{kg}$

Figure 5.9: Measured vs. simulated $V(t)$ for four representative cases

5.2. Lilienthal measurements

Lilienthal's work with the *Rundlaufapparat* was extremely important and influenced later flight research. To understand what he measured with the whirling-arm device, and to check whether his results were actually correct, the tests are reproduced as closely as practicable.

5.2.1. Experimental setup

The *Rundlaufapparat* reconstruction is described in Chapter 3.

Equipment:

- driving weights for the rotation,
- small weights for the lift balance,
- a long pole to rewind the ropes and set the starting position,
- a handheld stopwatch with 0.01 s resolution.

Lilienthal's notes indicate that times were recorded with a resolution of 0.1 s [11].

Lilienthal wrote: "the machine was erected in the open, experiments were only carried out during perfect calms; buildings and trees were sufficiently far away not to exert any disturbing influence upon the test surfaces" [2, Ch. 28]. The present experiments are conducted indoors in DLR's 1MG hall (Göttingen): airflow is undisturbed, but wall/blockage effects are significant, which may introduce differences relative to the historical outdoor tests. For this reason, future tests will also be conducted outdoors.

5.2.2. Experimental procedure

The following steps are carried out to reproduce Lilienthal's experiments on the whirling-arm apparatus.

Step 1. Baseline (arms only). The apparatus is first characterized without wings to quantify the arm drag. Pairs of equal hanging masses are mounted on both sides, ranging from 0.5 kg to 20 kg. To reproduce Lilienthal's method, the apparatus is released from rest and allowed to run $n = 2$ turns; the drop time is recorded with a stopwatch. With the present drum diameter $d = 450\,\text{mm}$, which differs from Lilienthal's, only two turns are possible, so the mean speed includes the acceleration phase. Implications of this limitation are discussed later. For each applied mass m, five timings t are taken; the mean speed is:

$$V = \frac{2\,\pi\,R\,n}{\Delta t}. \tag{5.29}$$

The resulting points are plotted to replicate Lilienthal's "empty" curve [11].

A slight upward bias of the lever (small lift) is observed without wings. The vertical position of the drive drum is kept within the same range as used later in the wings configuration; neither so low that the drum risks rubbing the structure (causing extra friction), nor so high that it might touch the top side of the structure. This helps keep parasitic effects comparable between the empty and wings runs.

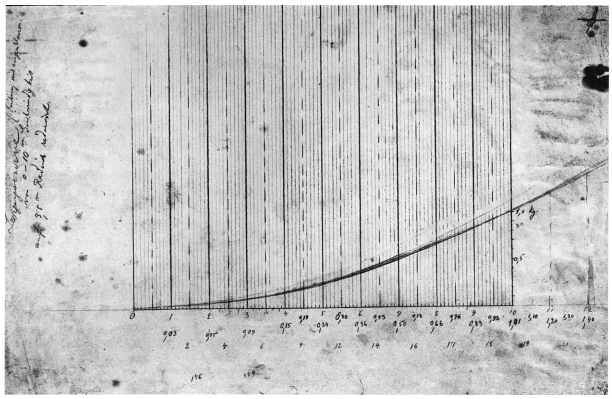

Figure 5.10: Otto Lilienthal, *Meßkurve zum Eigenwiderstand des Rundlaufapparats* (Measurement curve of the inherent resistance of the whirling-arm apparatus), 1874. Pencil on paper, 21.0 × 33.0 cm; 8 pages. Otto-Lilienthal-Museum Bildarchiv, Archiv-ID 00112; copy after Deutsches Museum, HS 6262, BN 2517. [9]

Step 2. Interpolating the baseline. To define the empty curve in Lilienthal's units, the hanging mass is converted to a tip-equivalent force via the torque balance (see Sec. 4.2). In kgf, for comparability with Lilienthal:

$$D_{\text{empty}} \equiv m_{\text{eq, empty}} = m\,\frac{r}{R} \quad [\text{kgf}]. \tag{5.30}$$

Data are plotted with mean speed on the x-axis and tip-equivalent empty force on the y-axis. For each mass, the five repeats are averaged and the resulting points are interpolated to obtain a function that returns the empty drag from the measured drop time (and thus mean speed) for $n = 2$ (interpolation performed in MATLAB). This interpolation is also used later for the analysis with the alternative empirical formula (Eq. 4.37).

Step 3. Mounting wings. After completing the empty configuration, the wings are installed. They are fixed at the arm tips by a rope system; by adjusting rope lengths the desired angle of attack α is set. Measurements at different α are performed with the same pair of hanging masses; in future work, different pairs of masses will be used to vary the driving torque and broaden the coverage of conditions. For this campaign with wings installed, a mass $m = 7.40\,\text{kg}$ is used; it allows most angles of attack to reach near-steady conditions while avoiding excessively high speeds that would compromise reliable timing and balance readings.

Step 4. Lift estimation. Because timing the turns and reading the lift simultaneously is difficult, these tasks are separated. First, lift is estimated with the lift balance and the

lever system; the weights in the balance are adjusted so that, when the falling weights touch the ground ($n = 2$ turns), the lever is horizontal, satisfying the steady-state torque balance (see Sec. 4.4). At higher speeds (typically at lower α), the system may not be fully steady and the lever may still be moving; in that case, the weights are set so the lever is horizontal exactly at the completion of the two turns, to mitigate non-steady effects. The tests are repeated several times to check the consistency of the balance mass m_{L}. The lift for one wing is:

$$L = \frac{m_{\mathrm{L}}\, g}{2}. \tag{5.31}$$

Step 5. Timed runs with wings. With α and m_{L} fixed, runs are performed and the time t_{w} to complete $n = 2$ turns is recorded. The mean wing speed is $V_{\mathrm{w}} = (2\,\pi\,R\,n)/t_{\mathrm{w}}$. The measurements are repeated ten times to reduce timing errors, such as ensuring exactly two turns and reaction time when starting/stopping the stopwatch.

Step 6. Angle-of-attack sweep (polar data). After completing the ten repetitions at one angle of attack, the same procedure is repeated at further angles to assemble the polar data. The angles α tested are:

$$\alpha \in \{-5^\circ\,,\, 0^\circ\,,\, 5^\circ\,,\, 10^\circ\,,\, 15^\circ\,,\, 20^\circ\,,\, 30^\circ\,,\, 40^\circ\,,\, 60^\circ\,,\, 90^\circ\}.$$

Step 7. Friction losses. Lilienthal noted that frictional losses were "experimentally determined beforehand" [2, Ch.19], but the exact procedure is not documented. A possibility is that he measured the hanging mass m_{f} required to initiate motion of the apparatus. Accordingly, the same procedure is applied to determine m_{f}, later used in Equation 4.31.

Step 8. Coefficient definitions (C_{D} - C_{L}). For each test, lift and drag are computed using the different formulas derived in Chapter 4. Each measurement is then nondimensionalized according to the alternatives described in Section 4.5. Because ten repetitions are considered for each angle α, the reported values in the results are the means of those repetitions, consistent with Lilienthal's reporting [2, Ch. 19].

Alternative empirical formula Given the measured time t_{w}, the equivalent empty force ($m_{\mathrm{eq,\,empty}}$) is read from the interpolated baseline (Step 2) and inserted into Equation 4.37; this option is included because the value used in Lilienthal's computation (Fig. 4.1) matches his empty graph (Fig. 5.10), even though no derivation is provided.

5.2.3. Arms-only results

The apparatus is characterized without wings to obtain the empty baseline. Equal pairs of hanging masses are tested:

$$m \in \{0.50, 1.00, 2.00, 3.00, 4.80, 7.40, 9.85, 12.45, 14.65, 19.70\}\,\text{kg}.$$

For each mass, five runs from rest are performed and the drop time over $n = 2$ turns is recorded (Fig. 5.11a). The mean tip speed for each run is computed as $V = (2\,\pi\,R\,n)\,/\,\Delta t$. With $n = 2$ and a drum diameter $d = 450\,\text{mm}$, this average always includes the initial acceleration; in the empty configuration a substantial fraction, if not all, of the drop is spent accelerating. Results are nevertheless reported with the mean speed to remain consistent with Lilienthal's procedure.

For each mass m, the per-mass mean speed $\overline{V}(m)$ and its sample standard deviation $\sigma_V(m)$ across repeats are evaluated. If t_i is the time recorded for run i at the same mass m, then

$$V_i = \frac{2\,\pi\,R\,n}{\Delta t_i}, \tag{5.32}$$

and, with n_m repeats at that mass,

$$\overline{V}(m) = \frac{1}{n_m}\sum_{i=1}^{n_m} V_i, \qquad \sigma_V(m) = \sqrt{\frac{1}{n_m - 1}\sum_{i=1}^{n_m}\big(V_i - \bar{V}(m)\big)^2}. \tag{5.33}$$

A shape-preserving cubic interpolation (pchip) is then computed through the per-mass means to obtain a smooth mapping $m = f(V)$, representing the hanging mass (without wings) to obtain the observed mean speed V (Fig. 5.11b). Horizontal error bars indicate $\pm 1\sigma$ on V at each mass; the relative spread increases slightly at higher speed because shorter timing windows amplify timing uncertainty, and the two-turn average is more sensitive to the acceleration part of the measurement.

For comparisons with the empty graph obtained by Lilienthal (see Fig. 5.10), this function $m(V)$ is expressed as the tip-equivalent empty force via Equation 5.30. The tip-equivalent empty force is:

$$m_{\text{eq, empty}}(V) = m(V)\,\frac{r}{R} \quad [\text{kgf}], \tag{5.34}$$

with $r = 0.225\,\text{m}$ and $R = 3.5\,\text{m}$ (Fig. 5.11c). This empty curve is used in the alternative empirical formulation (Eq. 4.37) to correct the wings configuration results.

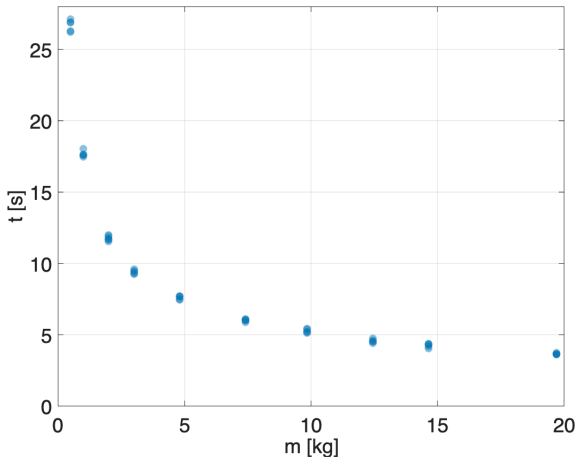

(a) Tested timings: drop time for $n = 2$ turns vs. hanging mass m

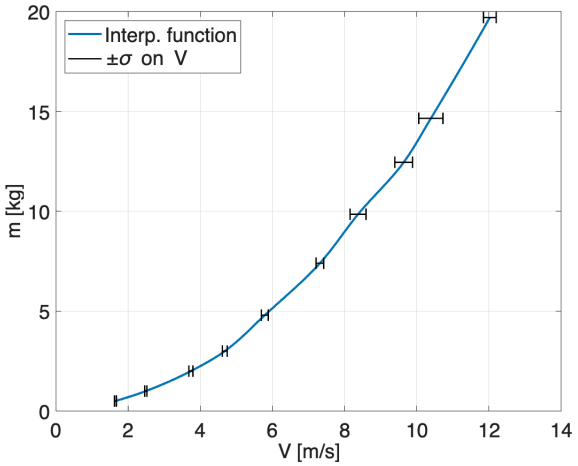

(b) Baseline $m(V)$: pchip interpolation through per-mass means; black error bars show $\pm 1\sigma$ on V

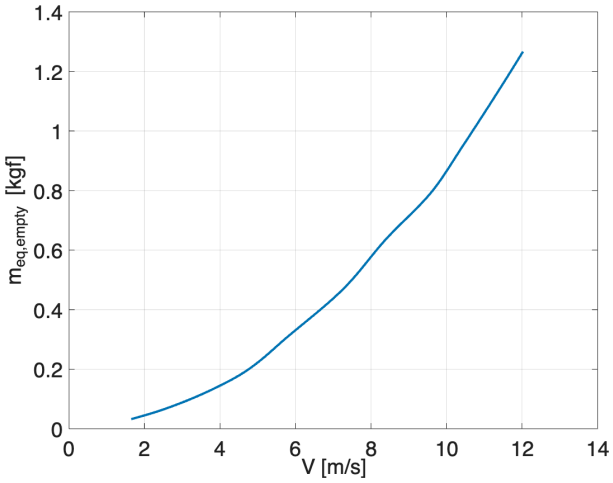

(c) Empty curve: tip-equivalent force $m_{eq,empty}$ vs. V

Figure 5.11: Arms-only baseline of the whirling-arm apparatus

5.2.4. Effect of driving mass

The main test campaign uses a single pair of equal hanging masses, $m = 7.40\,\mathrm{kg}$. To assess the influence of the applied mass (and therefore of the driving torque) at a fixed aerodynamic condition, tests at $\alpha = 0°$ are repeated with different pairs of equal masses:

$$m \in \{4.80, 7.40, 9.85, 12.45\}\,\mathrm{kg}.$$

As in the main campaign, ten repetitions are performed for each mass. For each run, the time for $n = 2$ turns is recorded and the mean tip speed is computed as $V = (2\,\pi\,R\,n)\,/\,\Delta t$.

Drag follows the relation derived in Section 4.2 without friction:

$$D = m\,g\,\frac{r}{R}\left[1 - \left(\frac{t_\mathrm{a}}{t_\mathrm{w}}\right)^2\right] \tag{5.35}$$

and lift is computed from Equation 4.33. To obtain the coefficients, the normalization through the Smeaton coefficient is adopted (see Sec. 4.5):

$$C_\mathrm{D} = \frac{D}{k\,S\,V^2}, \qquad C_\mathrm{L} = \frac{L}{k\,S\,V^2}. \tag{5.36}$$

At fixed α, the aerodynamic coefficients are expected to be independent of the driving mass. The results in Figure 5.12 show that C_D varies only weakly across the four masses, whereas C_L exhibits a larger spread. Let $\overline{C_\mathrm{L}}^{(i)}$ be the per-mass means ($i = 1, \ldots, 4$). Define:

$$\Delta C_\mathrm{L} = \max_i \overline{C_\mathrm{L}}^{(i)} - \min_i \overline{C_\mathrm{L}}^{(i)}, \qquad \overline{C_\mathrm{L}}^{*} = \tfrac{1}{4}\sum_{i=1}^{4} \overline{C_\mathrm{L}}^{(i)}, \qquad \Delta_\% = \frac{\Delta C_\mathrm{L}}{\overline{C_\mathrm{L}}^{*}} \times 100\%. \tag{5.37}$$

Across the four driving masses, these give: $\overline{C_\mathrm{L}} \in [0.0913,\, 0.1349]$, $\Delta\overline{C_\mathrm{L}} = 0.0436$, $\Delta_\% = 35.93\%$. Applying the same to the drag gives: $\overline{C_\mathrm{D}} \in [0.0829,\, 0.0844]$, $\Delta\overline{C_\mathrm{D}} = 0.0015$, $\Delta_\% = 1.85\%$. This spread shows a stronger correlation with the driving torque (and therefore with the mean velocity reached) than with the mass alone. When the velocities are low ($V < 5\,\mathrm{m/s}$ in this case; see Tab. 5.1), computing the lift becomes challenging. The lift signal scales with V^2 while mechanical friction and other parasitic forces remain relatively constant. With rotating-arm tests, unsteady effects and low-Reynolds-number sensitivity to separation and hysteresis further increase the observed variability in C_L [32].

Mass m [kg]	**$\overline{V}$ [m/s]**	**$\overline{C_\mathrm{D}}$ [−]**	**$\overline{C_\mathrm{L}}$ [−]**	**n [−]**
4.80	4.5894	0.0837	0.0913	10
7.40	5.7520	0.0844	0.1279	10
9.85	6.6255	0.0829	0.1315	10
12.45	7.5514	0.0833	0.1349	10

Table 5.1: Mean results per driving mass at $\alpha = 0°$

These qualitative conclusions remain unchanged under the alternative formulations and normalizations considered elsewhere in this chapter, but they must be accounted for in the main test campaign, especially at high angles of attack, where the velocities are lower.

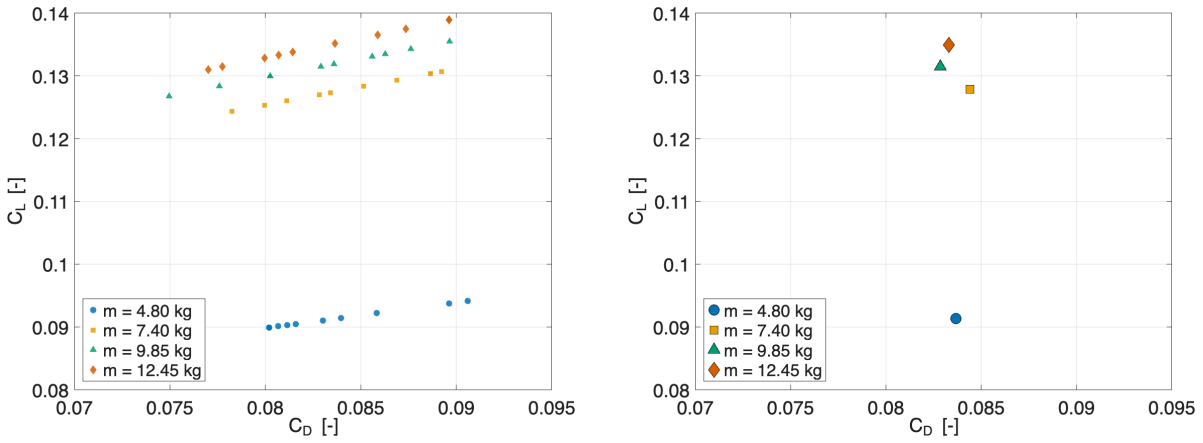

(a) C_L vs. C_D tests at different applied masses

(b) Per-mass means of C_L vs. C_D

Figure 5.12: Effect of driving mass at $\alpha = 0°$

5.2.5. Wings-on results

Lilienthal's experiments are reproduced with the present apparatus to enable a direct comparison with his historical results. Apart from minor differences in apparatus and procedure (see Sec. 5.2.9), the tests follow the method described in Section 5.2.2. The driving mass is 7.40 kg. Ten angles of attack α are tested, with ten repetitions per angle, covering Lilienthal's α range and reducing timing errors.

In this section, the drag uses the no-friction form and lift follows the balance evaluation (derivations in Ch. 4):

$$D = m\,g\,\frac{r}{R}\left[1 - \left(\frac{t_\mathrm{a}}{t_\mathrm{w}}\right)^2\right], \qquad L = \frac{m_\mathrm{L}\,g}{2}. \tag{5.38}$$

To obtain the coefficients in Figure 5.13, the measured forces are normalized with four different conventions (Sec. 4.5):

- normalization through the Smeaton formula for the drag at 90°: $D = k\,S\,V^2$ with $k = 0.13\,\mathrm{kgf/[m^2\,(m/s)^2]}$, as adopted by Lilienthal [1];
- normalization through the drag measured at 90°;
- normalization through the Smeaton formula but with the modern coefficient $k = 0.07989\,\mathrm{kgf/[m^2\,(m/s)^2]}$ (equivalent to $k = \frac{1}{2}\,\rho\,C_\mathrm{D,flatplate}$);

[1]The coefficient k is expressed in $\mathrm{kgf/[m^2\,(m/s)^2]}$ for comparability with Lilienthal; conversions to SI (N) are applied where needed.

- normalization through the classic definition of aerodynamic coefficients $\frac{1}{2}\rho V^2 S$.

The results are superimposed on Plate IV because the test wing adopted for these measurements matches that plate's camber (see Sec. 3.5) [2].

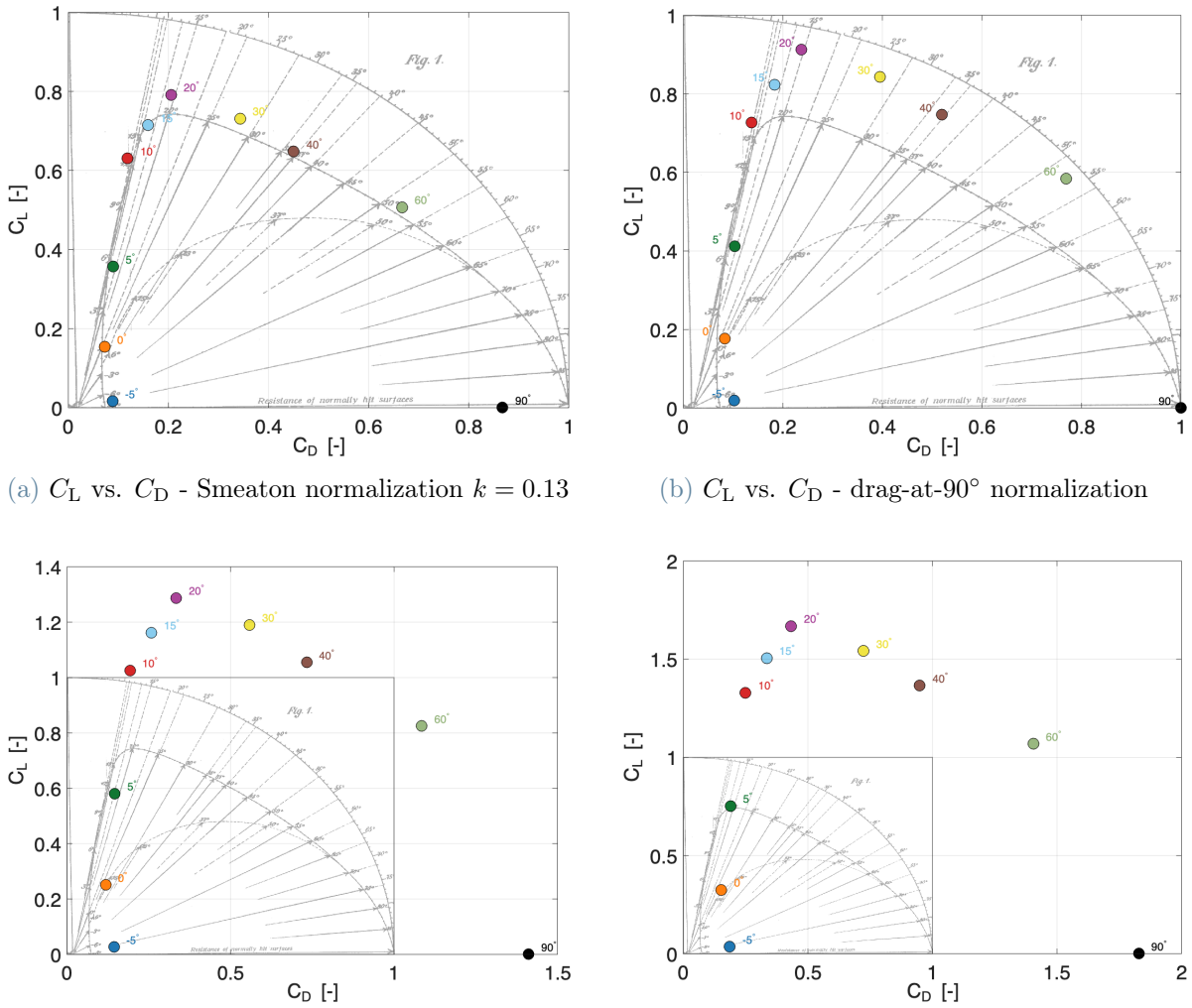

(a) C_L vs. C_D - Smeaton normalization $k = 0.13$

(b) C_L vs. C_D - drag-at-90° normalization

(c) C_L vs. C_D - modern Smeaton normalization $k = 0.0799$

(d) C_L vs. C_D - $\frac{1}{2}\rho V^2 S$ normalization

Figure 5.13: Comparison with Lilienthal's Plate IV [2] under different normalizations

Except for the value at 90°, which he possibly never measured, the normalization with the Smeaton formula (and the k adopted by Lilienthal) gives the closest agreement with his results, once again suggesting that, as he wrote in his book, he never measured that force but always adopted Smeaton's formula [2]. At high α the differences between these results and the historical ones increase. Because the same pair of masses is used for all

measurements, higher α increases drag and therefore lowers the mean speed V; this makes the force estimation more difficult, especially the lift. Lilienthal in his experiments varied the driving masses and averaged over the different pairs of masses tested, which likely mitigated this low-speed effect.

For completeness, the polars $C_{\mathrm{L}}(\alpha)$ and $C_{\mathrm{D}}(\alpha)$ are reported in Figure 5.14; coefficients use the same normalization as Figure 5.13a and the color code matches the legend.

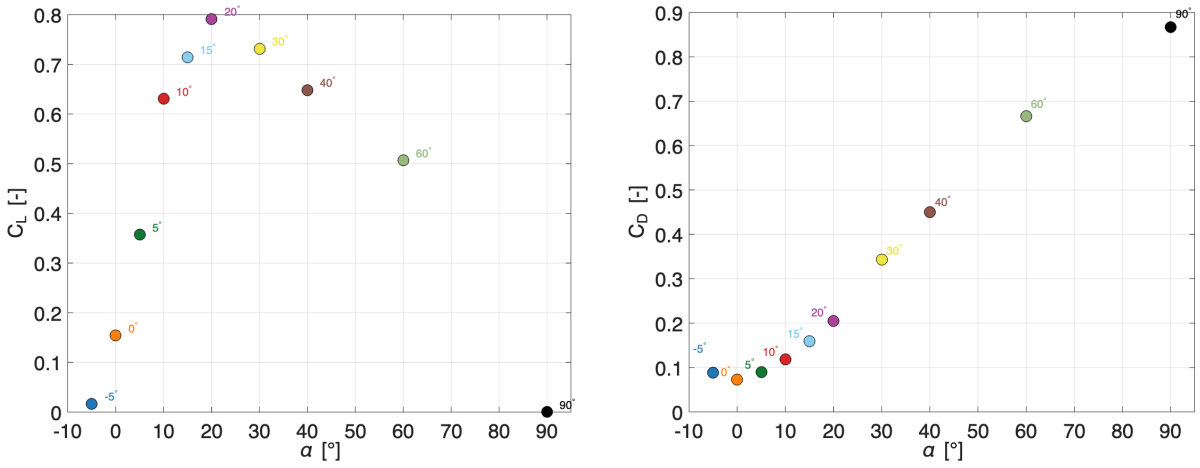

(a) C_{L} vs. α (b) C_{D} vs. α

Figure 5.14: Polars $C_{\mathrm{L}}(\alpha)$ and $C_{\mathrm{D}}(\alpha)$

5.2.6. Alternative formulations

In Chapter 4, different expressions for the drag were derived. The baseline without friction, also used in Section 5.2.5 to show the apparatus results, is:

$$D = m\,g\,\frac{r}{R}\left[1-\left(\frac{t_{\mathrm{a}}}{t_{\mathrm{w}}}\right)^2\right]. \tag{5.39}$$

A second expression, based on some assumptions on friction, introduces a constant loss m_{f}:

$$D = (m-m_{\mathrm{f}})\,g\,\frac{r}{R}\left[1-\left(\frac{t_{\mathrm{a}}}{t_{\mathrm{w}}}\right)^2\right]. \tag{5.40}$$

This constant value is measured as the mass required to start the apparatus: $m_{\mathrm{f}} = 0.3\,\mathrm{kg}$.

A third empirical expression is also used, although not derived analytically, but because it is numerically consistent with values adopted by Lilienthal [11]:

$$D = (m-m_{\mathrm{eq,\,empty}})\,g\,\frac{r}{R}\left[1-\left(\frac{t_{\mathrm{a}}}{t_{\mathrm{w}}}\right)^2\right]. \tag{5.41}$$

Here $m_{\mathrm{eq,\,empty}}$ is obtained from the velocity-mass interpolation of Step 2 (Sec. 5.2.2). Given the wings run time t_{w} (and thus V_{w}), the function gives the empty configuration mass m' that would produce the same speed which is then converted to a tip-equivalent force as $m_{\mathrm{eq,\,empty}} = m'\,(r\,/\,R)$. Since this quantity is already referred to the wing position, subtracting it from a quantity written before torque scaling (the hanging mass m in Eq. 5.41) is inconsistent; this expression should be therefore treated as heuristic and its results are included for completeness.

For a fair comparison, all three are converted to coefficients using the Smeaton normalization $D = k\,S\,V^2$ with $k = 0.13\,\mathrm{kgf}/[\mathrm{m}^2\,(\mathrm{m/s})^2] = 1.2753\,\mathrm{N}/[\mathrm{m}^2\,(\mathrm{m/s})^2]$ (Sec. 4.5). Lift and C_{L} are identical across the three models, since the lift formula is unchanged.

Figure 5.15b shows that the differences in drag coefficient C_{D} are small. For the constant friction model the difference is constant at -4.05% relative to the baseline without friction, across the tested α range. The empirical correction departs by about -4% at small α and gradually approaches about -1% near 90°. This trend reflects that at higher α the wing drag increases, the mean speed V decreases, and the relative impact of subtracting this empirical correction $m_{\mathrm{eq,\,empty}}$ diminishes. Quantitatively, the root-mean-square-error (RMSE) in C_{D} relative to the baseline is 0.016 for the friction model and 0.006 for the empirical model; the maximum absolute deviations are 0.036 and 0.009, respectively (over the ten α values). The metrics are defined as:

$$\mathrm{RMSE} = \sqrt{\frac{1}{N}\sum_{i=1}^{N}\left(C_{D,i}^{\mathrm{model}} - C_{D,i}^{\mathrm{base}}\right)^2}, \qquad \max|\Delta C_D| = \max_i \left|C_{D,i}^{\mathrm{model}} - C_{D,i}^{\mathrm{base}}\right|. \tag{5.42}$$

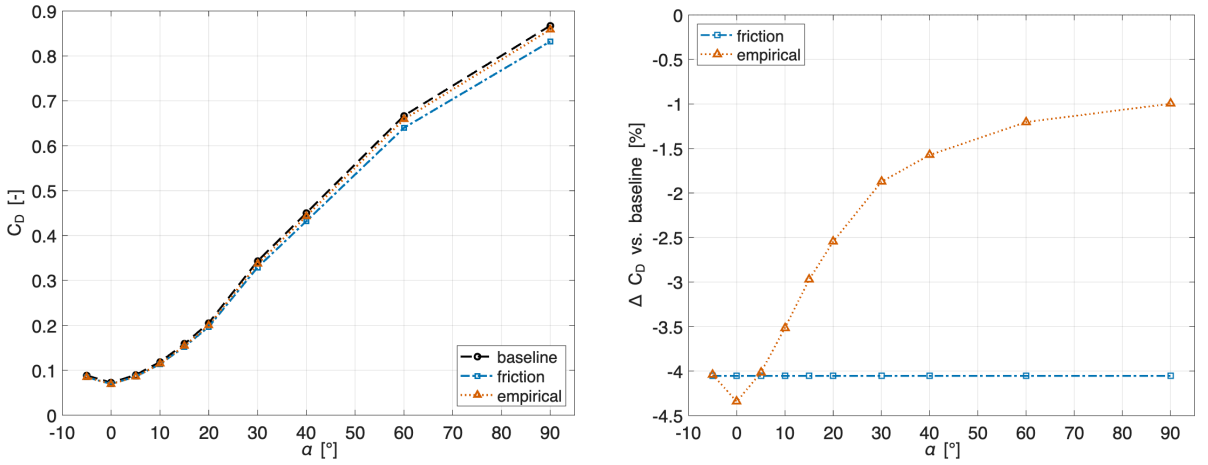

(a) C_D vs. α for the three drag formulas (b) Percent difference in C_D relative to the baseline

Figure 5.15: Comparison of drag formulations

5.2.7. Smeaton coefficient from experiments

With the force at 90°, the Smeaton coefficient can be measured and compared with the historical and the modern values. The wing tested is not a thin flat plate, while the original coefficient refers to the perpendicular force on a flat plate. From the ten repetitions at 90°, ten mean velocities V_w and ten drag values $D_{90°}(V_w)$ are obtained, both with the no-friction Equation 5.39 and with the friction Equation 5.40. Applying the Smeaton formula for the "air resistance" at 90° (Eq. 4.17), the per-run values of k are:

$$k_{\text{meas}} = \frac{D_{90°}(V_w)}{S\,V_w^2}. \tag{5.43}$$

Averaging the ten values in the no-friction case:

$$k_{\text{meas}} = 0.11276\,\frac{\text{kgf}}{\text{m}^2\,(\text{m/s})^2} = 0.00462\,\frac{\text{lbf}}{\text{ft}^2\,\text{mph}^2} = 1.10622\,\frac{\text{N}}{\text{m}^2\,(\text{m/s})^2}.$$

Including the constant frictional loss m_f reduces the drag by about 4% at fixed V_w, and therefore lowers k accordingly:

$$k_{\text{meas}} = 0.10819\,\frac{\text{kgf}}{\text{m}^2\,(\text{m/s})^2} = 0.00443\,\frac{\text{lbf}}{\text{ft}^2\,\text{mph}^2} = 1.06137\,\frac{\text{N}}{\text{m}^2\,(\text{m/s})^2}.$$

For reference (Sec. 2.5.3), the measured Smeaton coefficient lies closer to the historical value measured by Smeaton than to the modern one:

$$k_{\text{meas}} = 0.11276\,, \qquad k_{\text{smeaton}} = 0.12216\,, \qquad k_{\text{mod}} = 0.07989 \quad \left[\frac{\text{kgf}}{\text{m}^2\,(\text{m/s})^2}\right].$$

The absolute differences are:

$$k_{\text{meas}} - k_{\text{smeaton}} = -0.00940, \qquad k_{\text{meas}} - k_{\text{mod}} = +0.03287 \quad \left[\frac{\text{kgf}}{\text{m}^2\,(\text{m/s})^2}\right].$$

As the relative differences show:

$$\frac{k_{\text{meas}} - k_{\text{smeaton}}}{k_{\text{smeaton}}} \times 100\,\% = -7.69\,\%,$$

$$\frac{k_{\text{meas}} - k_{\text{mod}}}{k_{\text{mod}}} \times 100\,\% = +41.14\,\%.$$

Possible contributors to these differences are discussed in Section 5.2.9.

The present apparatus yields a coefficient closer to Smeaton's historical value than to the modern value or to the early Wright wind tunnel result (see Sec. 2.5.3). The discrepancy is consistent with methodological biases of rotating arm measurements (finite radius kinematics, acceleration during timed runs, interference from arms and ropes, and blockage), together with the use of a non-plate article at 90°. Within that historical context, Lilienthal's choice of $k = 0.13\,\text{kgf}/[\text{m}^2\,(\text{m/s})^2]$ was reasonable, even though modern theory and calibrations indicate lower values.

5.2.8. Uncertainty analysis

This section quantifies the measurement uncertainty following the ISO GUM framework [33]. Two classes of contributions are distinguished: statistical (Type A), obtained from repeated readings, and instrumental/model (Type B), arising from instrument resolution, alignment and geometric tolerances, and modeling assumptions. Unless noted otherwise, Type B bounds are rectangular and are converted to standard uncertainties by division by $\sqrt{3}$.

Timing and the requirement of "exactly two turns" dominate the acquisition. Even with careful execution, residual start–stop jitter and small angular offsets from exactly two turns are unavoidable. Since these effects are indistinguishable in the data, they are treated within repeatability (Type A). Ten repetitions are acquired at each condition (α), so the standard uncertainty of the mean scales as $1/\sqrt{10}$. Stopwatch resolution contributes a

Type B rectangular term that also reduces by $1/\sqrt{10}$ when averaging $n = 10$ runs.

Table 5.2 lists the Type B inputs (and their adopted distributions) used in the propagation; the statistical terms from repeatability are added at the propagation stage. When two independent sources act on the same quantity (as for lift mass and tip radius), their standard uncertainties are combined in quadrature.

Quantity	**Value**	**Bound**	**Std. unc. u**	**Distribution**
Hanging mass m	7.40 kg	$\pm$ 0.010 kg	0.010 / $\sqrt{3}$ kg	Balance resolution (rect.)
Lift mass (lever) m_{L}	(per angle)	$\pm$ 0.050 kg	0.050 / $\sqrt{3}$ kg	Lever error (rect.)
Lift mass (balance) m_{L}	(per angle)	$\pm$ 0.050 kg	0.050 / $\sqrt{3}$ kg	Lift balance resolution (rect.)
Lift mass combined $u_{\mathrm{m_L}}$	(per angle)	–	$\sqrt{u_{\mathrm{lev}}^2 + u_{\mathrm{bal}}^2}$ = 0.0408 kg	Two independent rectangular bounds
Tip radius (static) R	3.50 m	$\pm$ 0.025 m	0.025 / $\sqrt{3}$ m	Wing position (rect.)
Tip radius (dynamic) R	3.50 m	$\pm$ 0.025 m	0.025 / $\sqrt{3}$ m	Wing oscillations (rect.)
Tip radius combined u_R	3.50 m	–	$\sqrt{u_{\mathrm{stat}}^2 + u_{\mathrm{dyn}}^2}$ = 0.0204 m	Two independent rectangular bounds
Drum radius r	0.225m	–	0.0015 m	Rope + manufacture
Area S	0.5 m^2	–	0.02 S	2 % standard relative
Smeaton coefficient k	0.13 $\frac{\mathrm{kgf}}{\mathrm{m^2\,(m/s)^2}}$	–	0	Assumed constant
Time runs t_{w}	(per run)	$\pm$ 0.01 s	0.01 / $\sqrt{3}$ s	Stopwatch resolution (rect.)
Arms-only time t_{a}	(per mass - 5 runs mean)	$\pm$ 0.01 s	$\frac{0.01}{\sqrt{3}\sqrt{5}}$ s	Per run resolution (rect.), averaged

Table 5.2: Input quantities and distributions for uncertainty propagation

It is noted that, for propagation, both forces and the Smeaton coefficient are expressed in kgf, consistent with Lilienthal's formulation. This choice does not affect the coefficient analysis because conversion to SI (N) multiplies both numerator and denominator by g,

which cancels in C_{D} and C_{L}.

The angle of attack setting uncertainty is fixed at $\pm 0.5^{\circ}$ (see Sec. 3.5.2). This does not enter the present propagation because the formulas do not depend explicitly on α.

For the analysis, the drag definition without friction (Eq. 5.39) is adopted, and the aerodynamic coefficients are obtained through the historical Smeaton formula with value of k equal to the one used by Lilienthal. Therefore, the uncertainty propagation and results reported below apply directly to the datasets plotted in Figures 5.13a–5.14.

Velocity uncertainty

$$V = \frac{2\,\pi\,R\,n}{t_{\mathrm{w}}}. \tag{5.44}$$

The two inputs that carry Type B uncertainty are R and t_{w} (operator reaction time on start/stop is already captured in repeatability):

$$\frac{\partial V}{\partial R} = \frac{2\,\pi\,n}{t_{\mathrm{w}}}, \qquad \frac{\partial V}{\partial t_{\mathrm{w}}} = -\frac{2\,\pi\,R\,n}{t_{\mathrm{w}}^{2}}. \tag{5.45}$$

$$u_{\mathrm{V}}^{2} = \left(\frac{\partial V}{\partial R}\,u_{\mathrm{R}}\right)^{2} + \left(\frac{\partial V}{\partial t_{\mathrm{w}}}\,u_{t_{\mathrm{w}}}\right)^{2}. \tag{5.46}$$

Equivalently, in relative form (useful for checks):

$$\left(\frac{u_{\mathrm{V}}}{V}\right)^{2} = \left(\frac{u_{\mathrm{R}}}{R}\right)^{2} + \left(\frac{u_{t_{\mathrm{w}}}}{t_{\mathrm{w}}}\right)^{2}. \tag{5.47}$$

Forces uncertainty

Lift. Lift, expressed in kgf, is obtained from the balance as:

$$L = \frac{m_{\mathrm{L}}}{2}, \qquad u_{\mathrm{L}} = \frac{u_{m_{\mathrm{L}}}}{2}. \tag{5.48}$$

Drag. Drag is obtained from Equation 5.39, again in kgf,

$$D = m\,\frac{r}{R}\left[1 - \left(\frac{t_{\mathrm{a}}}{t_{\mathrm{w}}}\right)^{2}\right], \tag{5.49}$$

so that:

$$\begin{aligned}
\frac{\partial D}{\partial m} &= \frac{r}{R}\left[1-\left(\frac{t_\mathrm{a}}{t_\mathrm{w}}\right)^2\right], & \frac{\partial D}{\partial r} &= m\,\frac{1}{R}\left[1-\left(\frac{t_\mathrm{a}}{t_\mathrm{w}}\right)^2\right],\\
\frac{\partial D}{\partial R} &= -m\,\frac{r}{R^2}\left[1-\left(\frac{t_\mathrm{a}}{t_\mathrm{w}}\right)^2\right], & \frac{\partial D}{\partial t_\mathrm{a}} &= -2\,m\,\frac{r}{R}\left(\frac{t_\mathrm{a}}{t_\mathrm{w}^2}\right),\\
\frac{\partial D}{\partial t_\mathrm{w}} &= 2\,m\,\frac{r}{R}\left(\frac{t_\mathrm{a}^2}{t_\mathrm{w}^3}\right).
\end{aligned} \tag{5.50}$$

$$u_\mathrm{D}^2 = \sum_{\mathrm{x}\in\{\mathrm{m,r,R,t_a,t_w}\}} \left(\frac{\partial D}{\partial x}\,u_\mathrm{x}\right)^2. \tag{5.51}$$

Coefficients uncertainty

Lift coefficient.

$$C_\mathrm{L} = \frac{L}{k\,S\,V^2}. \tag{5.52}$$

Considering k as a constant value adopted by Lilienthal:

$$\frac{\partial C_\mathrm{L}}{\partial L} = \frac{1}{k\,S\,V^2}, \quad \frac{\partial C_\mathrm{L}}{\partial S} = -\frac{L}{k\,S^2\,V^2}, \quad \frac{\partial C_\mathrm{L}}{\partial V} = -\frac{2\,L}{k\,S\,V^3}. \tag{5.53}$$

$$u_{C_\mathrm{L}}^2 = \left(\frac{\partial C_\mathrm{L}}{\partial L}\,u_\mathrm{L}\right)^2 + \left(\frac{\partial C_\mathrm{L}}{\partial S}\,u_\mathrm{S}\right)^2 + \left(\frac{\partial C_\mathrm{L}}{\partial V}\,u_\mathrm{V}\right)^2. \tag{5.54}$$

Drag coefficient.

$$C_\mathrm{D} = \frac{D}{k\,S\,V^2}. \tag{5.55}$$

When uncertainties are propagated in two stages (first u_D and u_V, then u_{C_D}), D and V are not independent because both depend on R and t_w. The covariance term $\mathrm{cov(D,V)}$ must be included to correctly account for the shared contributions of R and t_w:

$$\mathrm{cov(D,V)} = \frac{\partial D}{\partial R}\,\frac{\partial V}{\partial R}\,u_R^2 + \frac{\partial D}{\partial t_\mathrm{w}}\,\frac{\partial V}{\partial t_\mathrm{w}}\,u_{t_\mathrm{w}}^2. \tag{5.56}$$

Again taking k constant:

$$\frac{\partial C_\mathrm{D}}{\partial D} = \frac{1}{k\,S\,V^2}, \quad \frac{\partial C_\mathrm{D}}{\partial S} = -\frac{D}{k\,S^2\,V^2}, \quad \frac{\partial C_\mathrm{D}}{\partial V} = -\frac{2\,D}{k\,S\,V^3}. \tag{5.57}$$

$$u_{C_\mathrm{D}}^2 = \left(\frac{\partial C_\mathrm{D}}{\partial D}\,u_\mathrm{D}\right)^2 + \left(\frac{\partial C_\mathrm{D}}{\partial S}\,u_\mathrm{S}\right)^2 + \left(\frac{\partial C_\mathrm{D}}{\partial V}\,u_\mathrm{V}\right)^2 + 2\,\frac{\partial C_\mathrm{D}}{\partial D}\,\frac{\partial C_\mathrm{D}}{\partial V}\,\mathrm{cov(D,V)}. \tag{5.58}$$

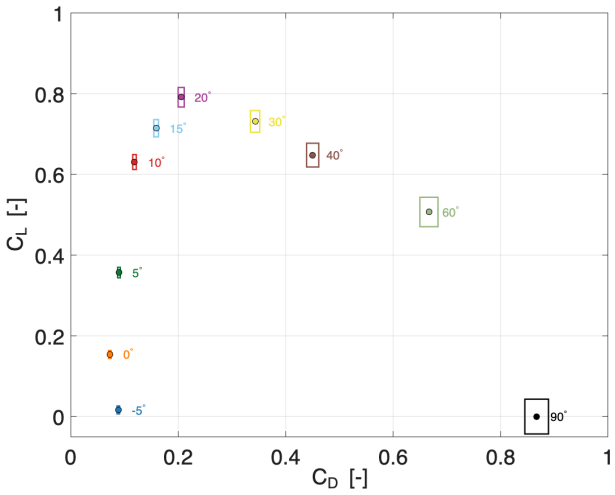

Figure 5.16: Uncertainty – polar curve C_L vs. C_D

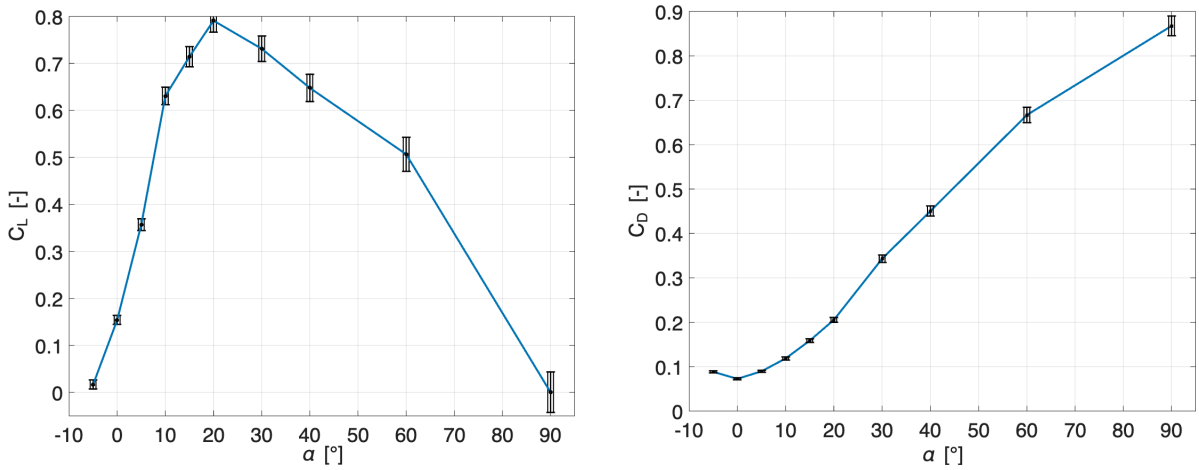

(a) C_L vs. α

(b) C_D vs. α

Figure 5.17: Uncertainty – $C_\mathrm{L}(\alpha)$ and $C_\mathrm{D}(\alpha)$

5.2.9. Differences vs. Lilienthal

The following differences and effects can bias both the measured coefficients (C_L, C_D) and the estimated Smeaton coefficient k:

- Shape and materials of the tested wing. The cambered wing, even though a reproduction, may present small differences in geometry and materials. Even more, at 90° the projected shape is nearly elliptical, unlike the thin rectangular flat plate assumed in the original Smeaton definition.
- Thickness and camber of the wing. Finite thickness and camber affect the effective

forces, especially at 90°, and therefore the inferred C_L, C_D and k.

- Single driving mass and low speed. As shown in Section 5.2.4, using a single pair of driving masses can influence the computation of C_L and C_D. Lilienthal varied the masses to reach higher velocities, which likely mitigated low-speed issues. At 90° the mean speed is about $V = 2.70\,\mathrm{m/s}$, making the exact evaluation of the forces even more complex and therefore affecting k.
- Blockage effects. Indoors tests introduce solid and wake blockage, modifying the forces at a given V compared with outdoor conditions.
- Acceleration bias. The average over two turns always includes the acceleration phase from rest; therefore the forces are inferred from an unsteady run. Historical treatments of this effect and differences in drum diameter may not match the present setup and methodology.
- Velocity non uniformity and interference. Radial variation of V across the span and local disturbances from structural components (arms, ropes, cables) can alter the flow and the loads.
- Ambient conditions. Variations in pressure, temperature and humidity (indoor vs. outdoor) affect comparisons.
- Friction modeling and apparatus differences. Static and kinetic friction, bearing characteristics, and construction details differ from the historical device and may vary with load and temperature; a constant m_f is only an approximation. All of these factors can alter the actual running behavior of the apparatus.
- Timing methodology. Stopwatch resolution, reaction time, and whether timing strictly spans two turns from rest, introduce additional uncertainty.

5.3. Kinematic model application

The MATLAB model (Appendix D) is applied to the actual results, obtained through the experiments and shown in Section 5.2.5, to try to understand how Lilienthal may have treated the velocity in the *Rundlaufapparat* experiments. Apart from a few notes reporting only the drop time, his treatment of the velocity is not explicit; from context he appears to have used a mean speed when computing drag and lift (see Fig. 4.1), but this is documented only for a single case [11].

The results in the next sections are derived from Equations 4.21–4.33, without any friction introduction.

5.3.1. Different velocity bases

From each run, and from its simulated counterpart, three velocity normalizations are post-processed:

$$\overline{V} = \frac{2\,\pi\,R\,n}{\Delta T}, \qquad V_{\mathrm{rms}} = \sqrt{\frac{1}{\Delta T}\int_0^{\Delta T} V(t)^2\,\mathrm{d}t}, \qquad V_{\max} = \max_t V(t), \tag{5.59}$$

where $\overline{V}$ is the mean velocity over the drop duration ΔT, V_{rms} is the root-mean-square speed (quadratic mean) over ΔT, and $V_{\max}$ is the maximum velocity reached during the run. The mean velocity $\overline{V}$ coincides for measured and simulated runs (see Sec. 5.1.7); the root-mean-square velocity V_{rms} and the maximum velocity $V_{\max}$ are taken from the simulations constrained by the measured drop height h. Therefore these last two values can have small differences from the true values, but they are minimal because the code has been tested and proved on several actual cases. Figure 5.18 shows the three different metrics for the tested case $\alpha = 0° - m = 7.40\,\mathrm{kg}$.

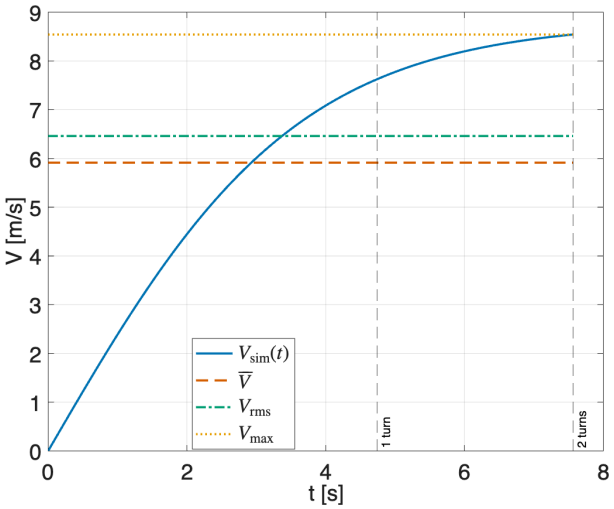

Figure 5.18: Representative time history $V_{\mathrm{sim}}(t)$ with the three scalar metrics: $\overline{V}$, V_{rms}, and $V_{\max}$

Because the aerodynamic forces scale with the instantaneous $V(t)^2$, the natural dynamic–pressure basis is $q(t) = \frac{1}{2}\rho V(t)^2$. Since instantaneous forces are unavailable in the historical drops, coefficients are reported under three scalar normalizations, obtained by replacing $\langle V^2 \rangle$ with each of the three bases:$\langle V^2 \rangle \in \{\ \overline{V}^2,\ V_{\mathrm{rms}}^2,\ V_{\max}^2\ \}$. The most appropriate choice to represent the effect of the instantaneous $V(t)^2$ is V_{rms}^2, because it equals the time-average of the quadratic term entering the aerodynamic forces. In accelerated drops, using $\overline{V}^2$ underestimates $\langle V^2 \rangle$, being exact only during perfectly steady states, whereas $V_{\max}^2$ overestimates it. Consequently, for the same force data the expected

ordering of the aerodynamic coefficients is

$$C\Big|_{\overline{V}^2} > C\Big|_{V^2_{\mathrm{rms}}} > C\Big|_{V^2_{\mathrm{max}}}.$$

This trend is visible in Figure 5.19: differences are largest at low drag ($\alpha \leq 20°$), where the motion is dominated by the acceleration phase, and they shrink at higher α, where the drop approaches a quasi-steady regime.

Two normalizations are compared. First, the Smeaton form (Eq. 4.17 with Lilienthal's k), where $C = F/(k\,S\,\langle V^2\rangle)$; here the choice of velocity basis is most visible (Fig. 5.19a). Second, a normalization through the drag at 90° and rescaled by each velocity (Fig. 5.19b):

$$C_{\mathrm{D}}(\alpha) = \frac{D(\alpha)}{\langle V^2\rangle}\,\frac{\langle V^2_{90°}\rangle}{D(90°)}, \qquad C_{\mathrm{L}}(\alpha) = \frac{L(\alpha)}{\langle V^2\rangle}\,\frac{\langle V^2_{90°}\rangle}{D(90°)}. \tag{5.60}$$

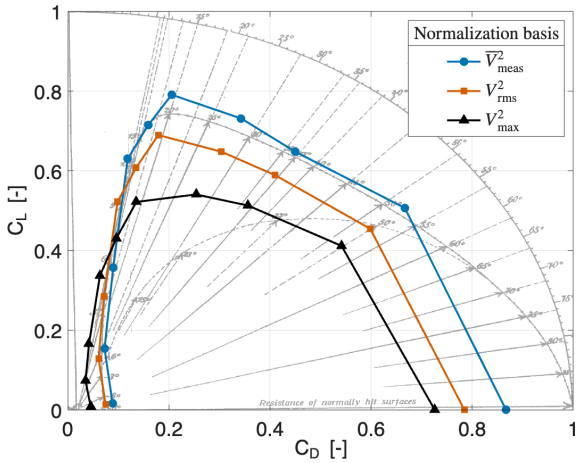

(a) Polar with Smeaton normalization $D = k\,S\,\langle V^2\rangle$

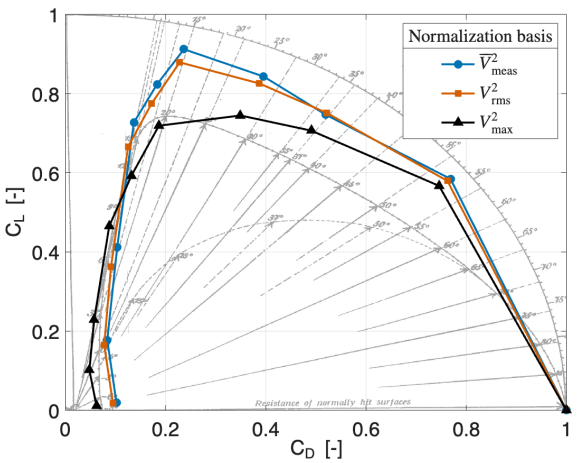

(b) Polar normalized by $D(90°)$ and rescaled by $\langle V^2\rangle$

Figure 5.19: Comparison with Lilienthal's results showing the effect of the different velocity bases

From the results it appears once again that Lilienthal, who performed the experiments in the late nineteenth century, probably adopted the mean speed with a Smeaton-form normalization, and was probably not in a position to compute a more appropriate velocity measure during the drop such as V^2_{rms}.

5.3.2. Comparison with Lilienthal's drum radius

The results with the present drum $r = 0.225\,\mathrm{m}$ are compared with the corresponding (simulated) results for Lilienthal's $r_0 = 0.175\,\mathrm{m}$ at the same drop height h. A smaller r

thus yields more turns (here $n \approx 2.57$ instead of $n = 2$), allowing a mean over the last two turns that is less affected by the acceleration phase. Lilienthal may have exploited this, although it is not explicitly documented.

A key choice is which mass m to apply when changing r. Three options are meaningful:

1. Same mass: keep m unchanged. Then the driving torque $\tau = m\,g\,r$ decreases with r, reducing acceleration and the final speed for the same h.
2. Same torque: rescale the mass to keep τ unchanged, $m_{\mathrm{Lil}} = m\,\frac{r}{r_0}$, isolating geometric effects of r.
3. Same final/max speed: select m so that the peak (or end-of-drop) speed matches the present case, $V_{\max}^{\mathrm{Lil}} \approx V_{\max}$.

Option (iii) is adopted because, in these tests, the lift-balance mass is fixed; matching the final/peak speed provides the most similar aerodynamic state at the end of the run, when lift is actually measured.

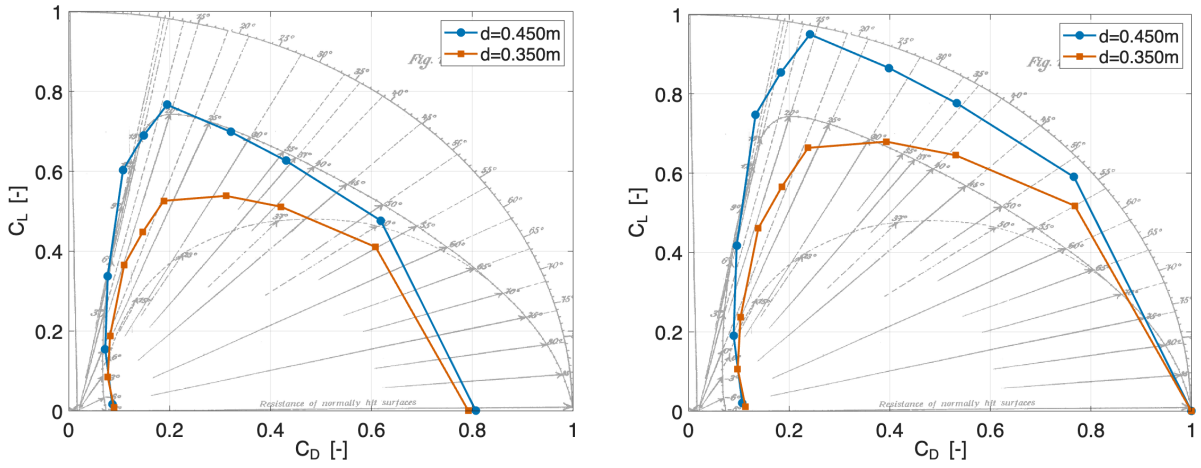

(a) Polar with Smeaton normalization

(b) Polar normalized by $D(90°)$

Figure 5.20: Comparison with Lilienthal's results showing the effect of different drum radii

With r_0 the curves trend lower; however, multiple confounders (mass choice, averaging window, residual acceleration) and, above all, the sensitivity of C_{L} when the lift-balance mass is fixed at each α, prevent firm conclusions.

6 | Wind-Tunnel Tests

6.1. Airfoil and wing design

For the wind-tunnel experiments and the simulations, a different wing shape is adopted compared with the *Rundlaufapparat* reproduction. Lilienthal tested several airfoils and reported that many produced similar aerodynamic results; therefore, for the tunnel and CFD work a more aerodynamically clean profile is selected to obtain clearer section aerodynamics while remaining faithful to his design approach.

6.1.1. Airfoil choice

In his book, Lilienthal sketched numerous cambered airfoils. The profile selected here is shown in Figure 6.1.

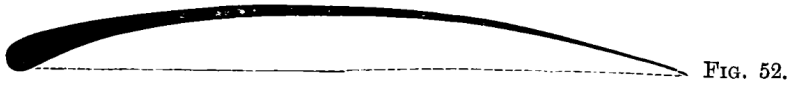

Figure 6.1: Selected airfoil for wind-tunnel tests and simulations [2, Fig. 52, Ch. 28]

The section exhibits features useful for clean measurements: a rounded, teardrop-like leading edge, a smoothly convex upper surface with gradual recovery, and a sharp trailing edge. Compared with many of Lilienthal's very thin, acutely pointed sketches, this profile remains thin overall but has a less acute nose, reducing sensitivity to small surface imperfections and alignment.

For consistency with Lilienthal, the chord is set to $c = 0.400\,\mathrm{m}$. A key design variable is the camber. Lilienthal measured the amount of curvature by the camber "height" w, the maximum rise of the surface above the chord measured normal to it, and expressed it as the ratio w/c (with the chord c called the "width"). In the present work, a camber of $w/c = 1/12 \approx 8.3\%$ is adopted for the wind-tunnel tests, the simulations, and the whirling-arm reproduction (see Sec. 3.5); this camber is the one that produced the best results in Lilienthal's experiments.

The airfoil is reconstructed from the drawing reported by Lilienthal in his book [2]. The profile is digitized and then smoothed in CATIA to remove drafting artifacts and obtain a regular, closed, gap-free curve suitable for meshing and subsequent wing design.

6.1.2. Wing design

The wing is designed from the airfoil selected and modeled in CATIA. Lilienthal's wings exhibit an approximately elliptical planform; at mid-span the airfoil section is maintained, while toward the tips the chord tapers and the section transitions to a small circular profile, a practical outcome of wooden structures covered with canvas [9]. Accordingly, the present wing preserves the airfoil section over most of the span and blends smoothly to a circular tip, maintaining a gradual change of camber and thickness. As a CAD reconstruction, it may differ slightly from the historical wings; nonetheless, keeping the section as constant as possible spanwise yields a wing that is as similar as practicable to Lilienthal's.

The chord is $c = 0.400\,\mathrm{m}$ and, for consistency with Lilienthal, the span is $b = 1.8\,\mathrm{m}$ [2, Ch. 28]. The reference area for forces is the projected planform area, as defined also by Lilienthal. Because the geometry is generated in CATIA from the digitized profile, small discretization tolerances may be present; the projected area computed in CAD is $S = 0.494\,\mathrm{m}^2$, close to the historical value of $S = 0.50\,\mathrm{m}^2$.

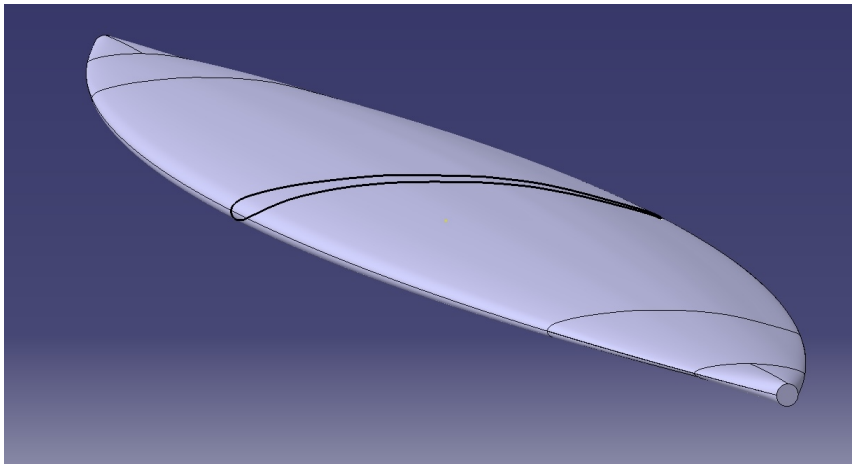

Figure 6.2: Wing model with airfoil highlight at mid-span in CATIA

6.1.3. Wing model reproduction

For the wind-tunnel tests, a half-scale model of the wing is manufactured.

After scaling by a factor 1:2, a negative mold of the upper surface was created to form the skins. Producing only the upper-surface mold reduced manufacturing time and risk;

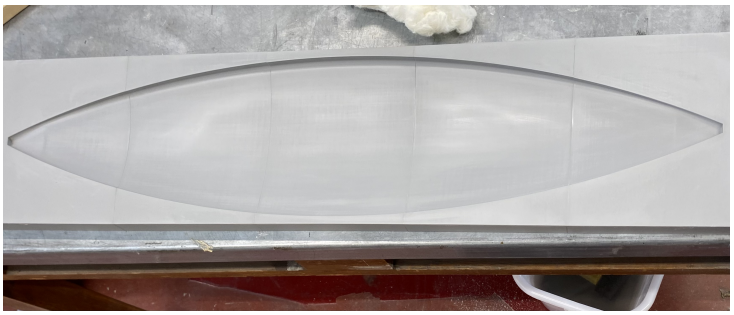

Figure 6.3: Half-scale upper-surface mold; eight PLA blocks with mold-release layer applied

although a two-sided mold would yield a closer geometric reproduction, the key features (rounded leading edge and very thin section) are preserved. The mold is divided into eight blocks and 3D-printed in PLA. Before lay-up, a mold-release layer is applied to enable demolding.

All plies are laid up sequentially on the single upper-surface mold (one-sided process). The laminate uses epoxy-bonded carbon fabric (2×2 twill); a thin glass-fiber surface veil is used as the outermost ply to improve optical contrast for flow visualization and to ease finishing. After cure, the part is demolded.

The model characteristics are:

- chord $c = 0.200\,\mathrm{m}$;
- span $b = 0.900\,\mathrm{m}$;
- reference area $S = 0.124\,\mathrm{m}^2$;
- camber $w/c = 1/12$.

The very thin section and the one-sided molding make both the measurements and the flow interpretation more delicate: the free-side contour is set by the laminate build-up, so small waviness/thickness scatter can shift the effective incidence; the small nose radius and sharp trailing edge foster laminar-separation bubbles and strong tip interactions that are highly Reynolds- and roughness-dependent. Nevertheless, the planform, chord, and camber ($w/c = 1/12$) are preserved, so the model is suitable for the planned force measurements and qualitative flow visualization.



Figure 6.4: Half-scale model for wind-tunnel tests

6.2. Wind-tunnel setup

6.2.1. RTG wind tunnel

The tests are carried out in the open-jet (Eiffel-type) wind tunnel of the Rotor Test Facility Göttingen (RTG) at DLR [34]. The model is positioned ahead of a square nozzle; the nozzle outlet measures $1.6 \times 1.6\,\mathrm{m}$. Ambient air is drawn through the intake window from outside the building, passes through the contraction and the $1.6 \times 1.6\,\mathrm{m}$ nozzle to form the inflow. Downstream of the nozzle, the jet passes on both sides of the control room and exits the building. The freestream Mach number is limited to $\mathrm{Ma} \leq 0.04$; all tests were conducted within this range, which is adequate for the present objectives.

As an Eiffel-type open-jet (fan downstream, suction), the RTG configuration reduces wall interference relative to closed test sections, which helps mimic whirling-arm conditions. It also introduces a developing shear layer at the jet boundary and interactions with the room flow, so correct model spacing to the nozzle and collector and careful blockage control are important [35].

6.2.2. Force balance

Forces are measured with a multicomponent external balance, a Kistler quartz three-component dynamometer (Type 9257B; top plate $100 \times 170\,\mathrm{mm}$). The sensor integrates four triaxial quartz elements preloaded between a base plate and a top plate; the combined outputs provide F_x, F_y, and F_z with high rigidity and natural frequency. Nominal ranges are $\pm 5\,\mathrm{kN}$ in F_x and F_y and $-5 \ldots 10\,\mathrm{kN}$ in F_z (for $|F_x|, |F_y| \leq 0.5\,F_z$); calibrated partial ranges down to $0 \ldots 50\,\mathrm{N}$ (F_x, F_y) and $0 \ldots 100\,\mathrm{N}$ (F_z) are available for higher resolution. Typical sensitivities are $\approx -7.5\,\mathrm{pC/N}$ (F_x, F_y) and $\approx -3.7\,\mathrm{pC/N}$ (F_z); linearity is $\leq \pm 1\%\,\mathrm{FSO}$ and cross-talk $\leq \pm 2\%$. The assembly is ground-insulated and, with the specified cables, is

IP67 rated [36]. Balance axes are defined with $F_x \parallel U_\infty$ (drag positive), F_z normal to the plate and positive downward (lift negative), and F_y spanwise (monitored but not used). Quartz/charge systems can exhibit temporal zero drift, so the indicated force may slowly wander during long runs. Mitigation includes warm-up, stable temperature, low-noise fixed cables, and periodic tare/zero before and after each run; in post-processing, a short baseline segment is used to remove residual offsets.

6.2.3. Model plate and sting

The model is mounted on a rigid wooden adapter plate bolted to the dynamometer top plate using the M8×1.25 threaded pattern.

The sting, bolted to the adapter plate, consists of one wooden element and one metallic element: the wooden part connects to the plate, and the metal part provides the bolted connection to the wing. Both CAD designs are shown in Appendix A. The geometry is optimized to keep the wing near the jet centerline while increasing the distance to the downstream sting to reduce support interference. The assembly is installed on the RTG angle-adjustment unit (AWE, *Anstellwinkel-Einrichtung*) with a motion range of approximately ±37.5°, so conditions within $\alpha \in [-10°, 35°]$ share nearly the same spatial location in the jet. The sting geometry is optimized for this range. To reach higher incidences and cover Lilienthal's full range, the sting is reconfigured to allow α up to 90°. In this second configuration the geometry is not optimal: support interference and positioning uncertainty are higher, as expected for these extreme angles (see Figure 6.5).

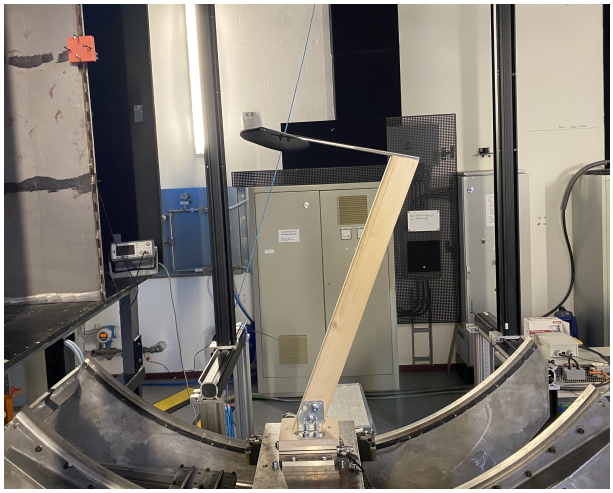

(a) Setup for $\alpha \in [-10°, 35°]$

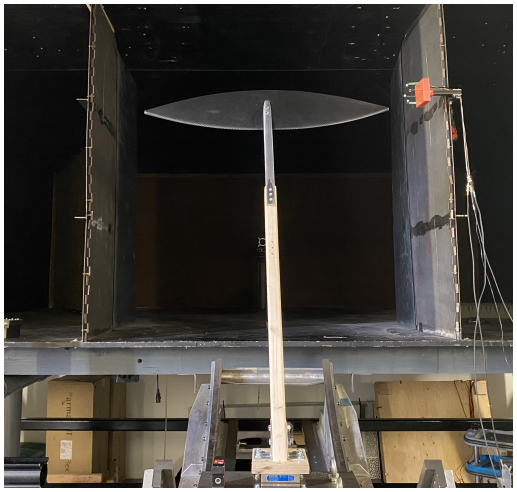

(b) Setup for $\alpha \in [35°, 90°]$

Figure 6.5: Wind-tunnel test setup: balance, plate, sting, and wing

6.2.4. Flow and ambient instrumentation

Tunnel speed is measured with an ultrasonic anemometer; ambient pressure, temperature, and humidity are recorded with a barometer, thermometer, and hygrometer. Air density is computed from the measured state as

$$\rho = \frac{p - e_{\mathrm{v}}}{R_d\, T} + \frac{e_{\mathrm{v}}}{R_v\, T}, \quad e_{\mathrm{v}} = \frac{\mathrm{RH}}{100}\, e_s, \quad e_s = 611.21 \, \exp\left[\left(18.678 - \frac{T_c}{234.5}\right)\frac{T_c}{257.14 + T_c}\right], \tag{6.1}$$

with $T = T_c + 273.15$ (K), p (Pa), $R_d = 287.05\,\mathrm{J/(kg\,K)}$, $R_v = 461.5\,\mathrm{J/(kg\,K)}$, and e_s (Pa).

All instruments were previously tested and calibrated.

6.2.5. Data acquisition

All data are acquired with a DEWETRON system and processed offline using the associated analysis software.

6.3. Wind-tunnel experiments

6.3.1. Experimental procedure

Before and after each test campaign, a zero-offset measurement is recorded. The RTG angle-adjustment unit executes a continuous sweep over its range; to increase point density in a single campaign, the sweep is run forward and backward. Only the descending branch is retained in the analysis, from $\alpha_{\mathrm{bal}} = +37.5^\circ$ down to $\alpha_{\mathrm{bal}} = -37.5^\circ$.

Measurements are taken with the wing installed and with the wing removed, and for both wind-on and wind-off conditions, so that weight, support loads, and sting interference can be characterized and removed.

The angle of attack of the wing follows the convention used throughout the work: the chord is the straight line joining LE and TE (see Sec. 6.1). The balance angle α_{bal} differs from the wing angle α_{wing} by a constant geometric offset that depends on the mechanical configuration. For the two wind-tunnel setups of Figure 6.5, the offsets are respectively:

$$\Delta\alpha_1 \equiv \alpha_{\mathrm{wing}} - \alpha_{\mathrm{bal}} = 5.97^\circ, \qquad \Delta\alpha_2 \equiv \alpha_{\mathrm{wing}} - \alpha_{\mathrm{bal}} = 60.35^\circ.$$

During all sweeps, the tunnel operates at $U_\infty \approx 9$–$10\,\mathrm{m/s}$; for the half-scale wing ($c =$

0.200 m) this corresponds to Re $\approx$ (1.2–1.3) $\times 10^5$ and Ma $\approx$ 0.027–0.03, giving good Reynolds- and Mach-number similarity to the whirling-arm tests and the CFD cases (Ma = 0.035, Re = 3.25×10^5).

6.3.2. Wind-tunnel data analysis

Data are processed in five steps for both configurations.

Step 1. Pre-processing. For each measurement file, a stationary window is selected and means and standard errors are computed for (F_x, F_y, F_z), V, p, T_c, RH. Humid-air density ρ and dynamic pressure $q = \frac{1}{2}\rho V^2$ follow from the measured state.

Step 2. Drift removal. Two zero points (start/end) bracket each campaign; a linear temporal drift is estimated channel-wise and subtracted to obtain drift-corrected forces. This mitigates the temporal zero drift typical of quartz/charge systems [36].

Step 3. Wing-on, wind-off tare. Angle-dependent tare functions are built from wind-off files with the wing installed, aligned to the wind-on set by a constant shift from overlapping angles, and subtracted to remove weight/support loads.

Step 4. Sting correction. Sting-only campaigns (wing removed) are processed analogously; a small-angle model of sting loads, normalized by q and expressed vs. α, is fitted and subtracted from the wing-on forces to yield wing-only forces in balance axes.

Step 5. Rotation and coefficients. Forces in balance axes are rotated by α_{bal} to obtain D and L, and then $C_D = D/(qS)$, $C_L = L/(qS)$. Plots versus wing angle use $\alpha_{\text{wing}} = \alpha_{\text{bal}} + \Delta\alpha_i$.

6.4. Wind-tunnel results

Figures 6.6–6.7 show the force measurements (as coefficients C_{L} and C_{D}) over the full incidence range. A noticeable discontinuity appears near $\alpha \approx 35°$, where the setup changes from the AWE-optimized configuration ($\alpha \in [-10°, 35°]$, Fig. 6.5a) to the high-incidence configuration ($\alpha \in [35°, 90°]$, Fig. 6.5b). The jump is more evident in C_{L} and smaller in C_{D}, consistent with a small effective-angle shift between configurations and support-interference differences that primarily affect lift.

In the pre-stall range, C_{L} grows approximately linearly and reaches a maximum at $\alpha \approx 12°$, after which stall sets in. From this point C_{L} decreases and becomes more unsteady, while C_{D} continues to rise. The angle of maximum lift $C_{\text{L,max}}$ and the onset of stall agree well

with the 3D CFD (see Sec. 7.4, stall onset $\alpha \approx 15°$); in the whirling-arm tests the lift continues to increase to about $\alpha = 20°$. The minimum drag occurs around $\alpha \approx 2°$-$3°$, in line with the 3D CFD results and close to the whirling-arm findings (see Sec. 5.2.5; the coarser sampling places the $C_{\mathrm{D,min}}$ at $\alpha = 0°$).

At negative incidence, an anomalous behavior is observed near $\alpha \approx -10°$: C_{L} becomes slightly positive and C_{D}, which had been rising as α moved more negative, decreases again. Plausible contributors are: (i) the particular geometry (teardrop-like nose and an extremely thin afterbody) promoting partial reattachment on the nominal pressure side at negative incidence; (ii) open-jet effects (shear-layer curvature, model position in the jet) and increased support interference; and (iii) residual tare/zero-drift errors. Accordingly, the data around $\alpha \approx -10°$ should be interpreted with caution.

Overall magnitudes are lower than in the CFD and whirling-arm data, which is consistent with the lower Reynolds number of the half-scale model (Re ≈ 1.2-1.3×10^5) and with added losses from surface tolerances and open-jet operation. Also, the very thin section yields small absolute loads and higher sensitivity to drift/tare, making the forces harder to resolve accurately. Trends (angle of $C_{\mathrm{L,max}}$ and stall, rise of C_{D} with α, and $C_{\mathrm{D,min}}$ near small positive α) are nevertheless coherent across datasets.

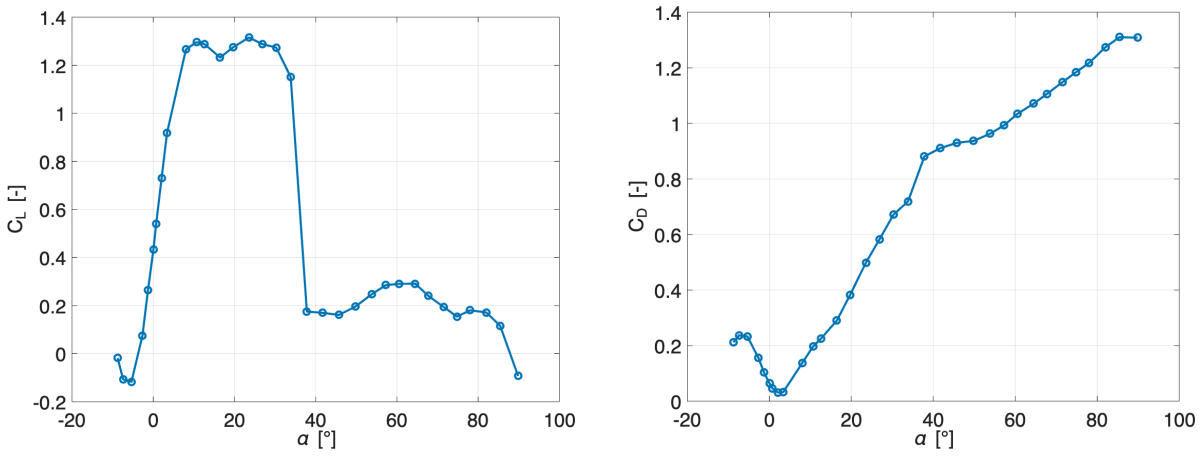

(a) C_{L} vs. α (b) C_{D} vs. α

Figure 6.6: Wind-tunnel results over the full angle range, $\alpha \in [-10°, 90°]$

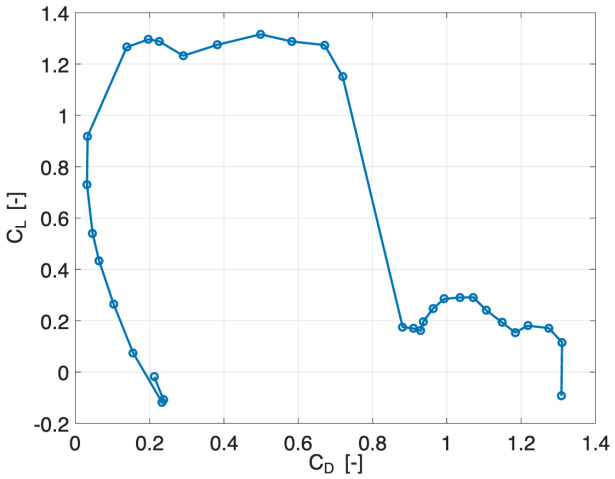

Figure 6.7: Wind-tunnel lift-drag polar over the full angle range, $\alpha \in [-10°, 90°]$

To better visualize the measurements in the more reliable configuration, the first setup results (Fig. 6.5a) are shown separately. In this range the model position is fixed and only α changes, and the downstream sting is farther from the wing, reducing support interference.

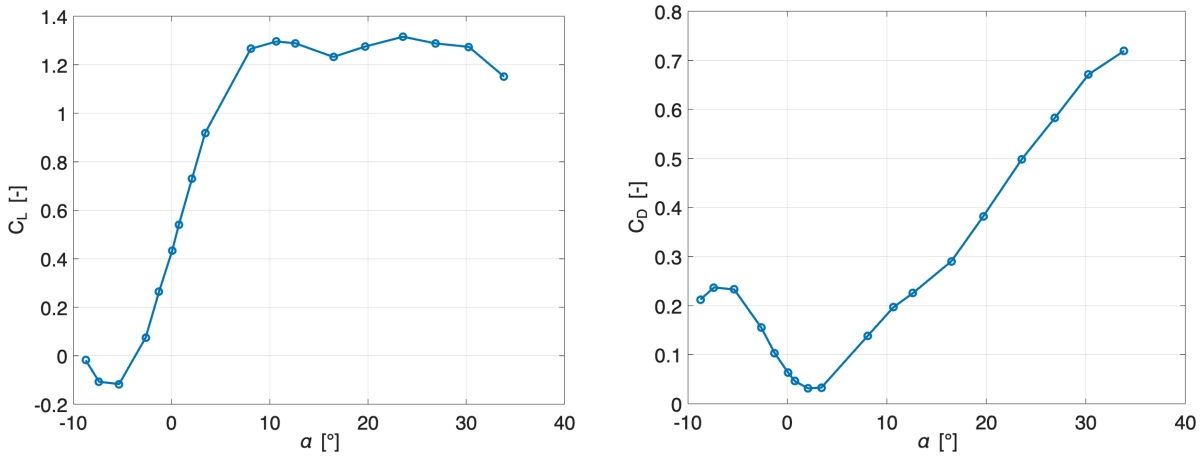

(a) C_L vs. α (b) C_D vs. α

Figure 6.8: Wind-tunnel results over the optimized angle range, $\alpha \in [-10°, 35°]$

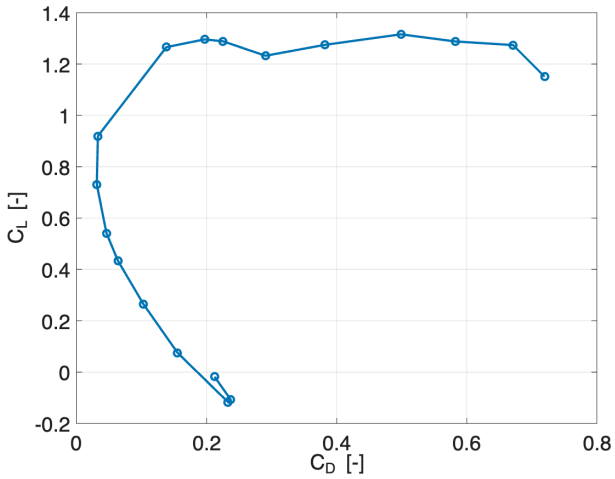

Figure 6.9: Wind-tunnel lift-drag polar over the optimized angle range, $\alpha \in [-10°, 35°]$

For reference, the wind-tunnel polar is also overlaid on Lilienthal's plate using Smeaton's normalization ($D = k\,S\,V^2$, $k = 0.13\,\mathrm{kgf}/[\mathrm{m}^2\,(\mathrm{m/s})^2]$ as adopted by Lilienthal), despite the different measurement methods (steady tunnel vs. rotational apparatus).

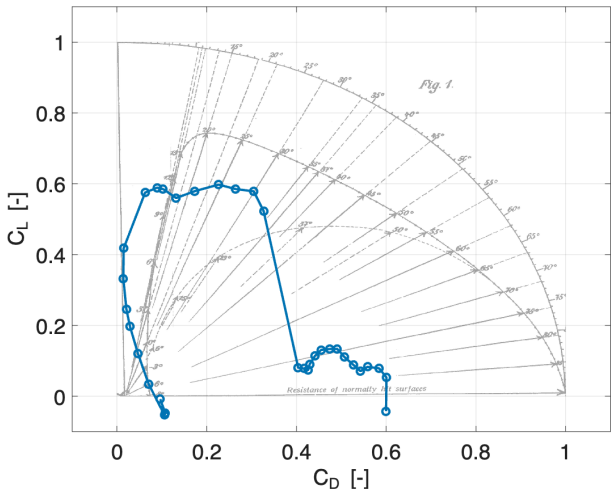

Figure 6.10: Comparison of wind-tunnel results with Lilienthal's data

7 | CFD Simulations of the *Rundlaufapparat* Wings

7.1. Objectives and scope

The wings and conditions of Lilienthal's *Rundlaufapparat* are challenging: very thin cambered wings at low velocities, where multiple separations are likely and the achievable accuracy is limited. In addition, because the device is rotational, after roughly half a turn each wing travels through disturbed flow produced by the preceding wake, as Lilienthal himself noted [2]. His parallel tests in a wind apparatus removed the rotational effect but introduced strong oscillations due to unsteady inflow.

This chapter presents steady RANS simulations aimed at characterizing the low-Ma, low-Re flow (kept close to the experimental range), identifying separation and reattachment features, and clarifying flow behavior relevant to the apparatus measurements. A further objective is to obtain aerodynamic polars of the studied airfoil and of a finite-span wing (reproducing one of Lilienthal's) for comparison with the whirling-arm measurements (see Sec. 5.2) and with the scaled-model wind-tunnel tests (see Ch. 6).

To approximate the real apparatus regime while acknowledging that the simulations are steady and non-rotational, the 2D setup includes a grid and operating-condition analysis to verify accuracy and to ensure a close representation of the actual flow behavior. Sensitivity to velocity is addressed within this framework by varying Ma (and thus Re) in a narrow band around Lilienthal's conditions. The 3D simulations are run at the same $(\alpha, \mathrm{Ma}, \mathrm{Re})$ range used in the experiments to isolate finite-span and tip effects that 2D cannot capture (tip vortex, induced downwash, spanwise lift variation).

7.2. Governing equations and turbulence closures

7.2.1. RANS formulation

Reynolds-averaged Navier-Stokes (RANS) equations are solved in steady form. With Reynolds decomposition $u_i = \overline{u}_i + u'_i$, the steady, incompressible, momentum equation in kinematic form reads

$$\overline{u}_j \frac{\partial \overline{u}_i}{\partial x_j} = -\frac{1}{\rho}\frac{\partial \overline{p}}{\partial x_i} + \nu \frac{\partial^2 \overline{u}_i}{\partial x_j \partial x_j} - \frac{\partial}{\partial x_j}\left(\overline{u'_i u'_j}\right), \tag{7.1}$$

where $\overline{u'_i u'_j}$ are the Reynolds stresses that require modeling. Alternative but equivalent forms appear in the literature depending on whether the equation is written with μ or ν, whether body forces are included, and whether the isotropic Reynolds-stress part is absorbed into a modified pressure p^* [37].

In eddy-viscosity closures, the Boussinesq hypothesis models the deviatoric part of the Reynolds stress as

$$-\overline{u'_i u'_j} = 2\nu_t \overline{S}_{ij} - \frac{2}{3} k_{\text{turb}} \delta_{ij}, \qquad \overline{S}_{ij} = \frac{1}{2}\left(\frac{\partial \overline{u}_i}{\partial x_j} + \frac{\partial \overline{u}_j}{\partial x_i}\right), \tag{7.2}$$

with the turbulent kinematic viscosity ν_t provided by a turbulence model [37].

Known limitations in separated, low-Re flows. For thin airfoils at low Ma–Re with separation bubbles (typically laminar at these low Re) and strong adverse-pressure gradients, steady eddy-viscosity RANS may mispredict separation onset, extent and reattachment, and can under-resolve unsteadiness that affects C_p plateaus and, especially, the drag C_D. Model-form uncertainty is significant in transitional regimes [38, 39]. Results are interpreted with these limitations in mind.

7.2.2. Turbulence models

The Reynolds stresses require closure; the following models are considered as options for the simulations.

Spalart-Allmaras (SA)

A one-equation eddy-viscosity model that transports a modified viscosity $\tilde{\nu}$; widely used for external aerodynamics for attached and mildly separated boundary layers [40]. The SA-neg variant (2012) adds a protected negative branch for $\tilde{\nu}$ with adjusted production, destruction, and diffusion terms to improve robustness near separation [41].

k-ω

Two-equation models transporting k and ω [42]. In practice, the Menter variants are employed: BSL blends k-ω (near wall) with k-ε (freestream), while SST adds a shear-stress limiter and a cross-diffusion term to improve behavior in adverse-pressure-gradient separation [43]. These models also favor wall-resolved grids ($y^+ \approx 1$) and can be sensitive to the choice of freestream ω; SST is generally more separation-tolerant than BSL.

Reynolds-Stress Model (RSM)

A second-moment closure solving transport equations for the six components of $\overline{u_i' u_j'}$ (plus ϵ or ω), enabling anisotropy, curvature/rotation effects, and rapid-distortion phenomena beyond the Boussinesq hypothesis [44]. RSM can improve predictions where turbulence anisotropy matters (strong curvature or complex separation), but it is more sensitive to mesh and boundary conditions and is computationally costlier and stiffer to converge.

Model choice

The Spalart-Allmaras model, in particular the SA-neg variant, is adopted for both the 2D and 3D simulations due to robustness and lower computational cost. In 2D checks, k-ω (Menter BSL) and an RSM variant produced force coefficients within a few percent of SA-neg; details are reported in Section 7.3.7. Given the small differences in this regime and the significantly higher cost/complexity of k-ω and RSM, SA-neg is the preferred baseline.

7.3. Numerical setup

The airfoil and wing configurations used in the simulations are defined in Section 6.1.

7.3.1. Flow solver

The computations are performed with the DLR–TAU code, solving the steady Reynolds-averaged Navier-Stokes equations in two and three dimensions [45]. Inviscid terms are discretized by a central scheme with scalar dissipation; viscous terms use a second-order formulation. Spatial accuracy is second order; time marching employs an explicit three-stage Runge-Kutta scheme with a fine-grid CFL adapted per grid (2D/3D) and angle of attack α. A multigrid acceleration is used with a four-level W-cycle in every simulation. The turbulence closure is Spalart-Allmaras (SA), specifically the SA-neg variant [41]. Freestream turbulence was set to an intensity of 2% and an eddy-viscosity

ratio $\mu_t/\mu_\ell = 10$ (capped at 100), a choice representative of low-disturbance inflow and providing a stable initialization of the SA working variable.

Convergence is monitored using the density residual and the aerodynamic coefficients (C_L, C_D, C_M). The density residual (the global ℓ_2 norm of the discrete density/continuity equation, normalized by its initial value) is reduced below 10^{-10} for the 2D simulations and below 10^{-7} for the 3D simulations. In addition, the coefficients are required to be steady: over the last 1000 iterations, their relative change must remain below 10^{-7} for all simulations. If either criterion is not met, iterations are continued until both are satisfied. Monitoring the aerodynamic coefficients ensures that numerical convergence also corresponds to a steady aerodynamic state around the airfoil/wing.

This setup is used for all angles of attack studied.

7.3.2. Reference frames and coefficient definitions

A right-handed Cartesian system is used: x is aligned with the incoming flow (streamwise), z lies in the airfoil section and is normal to the chord line, and y is spanwise (out of plane in 2D). Unless stated otherwise, positive moments are nose-up.

Chord and origin. The chord line is the straight segment joining leading and trailing edges (LE-TE). The moment reference point is taken at mid-chord on this line. This choice does not affect C_L or C_D and is reported because C_M depends on the reference location. If needed, moments about another reference x_{ref2} (measured from LE) follow

$$C_\mathrm{M}(\mathrm{ref2}) \;=\; C_\mathrm{M}(\mathrm{ref1}) \;+\; C_\mathrm{L}\,\frac{x_{\mathrm{ref1}} - x_{\mathrm{ref2}}}{c}, \tag{7.3}$$

with positive C_M defined nose-up.

Reference quantities (2D). For 2D runs, the solver's coefficients are referenced to an area consistent with the mesh scale. The reference area is set to

$$S_{\mathrm{ref,2D}} = c \times s_{\mathrm{ref}},$$

with an artificial span $s_{\mathrm{ref}} = 1\,\mathrm{mm}$ (matching the geometry scale). Thus, for $c = 400\,\mathrm{mm} = 0.4\,\mathrm{m}$,

$$S_{\mathrm{ref,2D}} = 0.4\,\mathrm{m} \times 0.001\,\mathrm{m} = 0.0004\,\mathrm{m}^2.$$

Reference quantities (3D). For 3D runs, the reference area S_{ref} and reference chord c_{ref} match the wing geometry reported in Section 6.1.

7.3.3. Limitations of 2D steady RANS

Steady eddy-viscosity RANS has known limitations for separated and turbulent flows; the present case (very thin airfoils at low Ma–Re with frequent separation) falls in this category. Separation and transition physics are inherently three-dimensional; constraining the solution to 2D suppresses spanwise instabilities, stall cells, and vortex dislocations that, in reality, govern bubble growth/shrinkage and reattachment. Consequences include: (i) possible misprediction of separation onset and extent, (ii) missing unsteady "breathing" of separation bubbles, (iii) biased drag, since C_{D} is sensitive to pressure recovery across separated regions and to the (model-dependent) transition location. In contrast, C_{L} and C_{M} are typically less sensitive over attached or mildly separated regimes. These aspects are documented for separated and transitional flows in standard references and reviews [38, 39, 43].

7.3.4. Computational domain and mesh

Hybrid unstructured grids are generated with the commercial software CENTAUR™. The outer boundary is an O-type circular farfield of radius $100\,c$ (unstructured interior with O-type outer contour), which minimizes blockage and reflections for the present low-Mach cases.

Near the airfoil, a structured boundary-layer (BL) stack of anisotropic quadrilateral layers (stretched normal to the wall) is used to resolve the wall region:

$$N_{\text{BL}} = 55, \qquad \Delta y_1 = 5 \times 10^{-6}\ \text{m}, \qquad \text{growth factor} \quad g_{\text{BL}} = 1.125.$$

The wall-unit coordinate is defined as $y^+ = y\,u_\tau/\nu$ with $u_\tau = \sqrt{\tau_w/\rho}$. The target is $y^+ \leq 1$ for all tested α and it is checked during the simulations [46]; Δy_1 was pre-estimated from standard skin-friction correlations and then reduced to ensure $y^+ \leq 1$ across the operating range [42]. The nominal BL stack thickness follows the geometric series

$$\Delta_{\text{BL}} \;=\; \Delta y_1 \,\frac{1 - g_{\text{BL}}^{N_{\text{BL}}}}{1 - g_{\text{BL}}} \;\approx\; 2.6 \times 10^{-2}\,\text{m} \;\; (\approx 0.065\,c\,),$$

sufficient to cover the viscous sublayer and the outer boundary layer, and to blend smoothly into the outer mesh.

A wake-refinement region starts slightly upstream of the leading edge and expands downstream. The region has a trapezoidal shape designed to enclose and better resolve the shear layer and wake; its layout is shown in Figure 7.1a. The region axis is aligned with the expected wake direction and, for higher angles ($\alpha \geq 30°$), the region is rotated and slightly enlarged to remain aligned with the flow. This increases the cell count moderately at high α, but it improves wake resolution in cases where steady RANS already carries greater uncertainty due to extensive separation; results in these conditions should therefore be interpreted with additional caution. The target triangle length scale inside the wake strip is $7.5 \times 10^{-3}\,c$, with smooth expansion away from the BL and wake.

Outside the BL and the wake region, unstructured triangle sizes increase smoothly toward the farfield. For most operating points the mesh contains $\approx 2.04 \times 10^5$ cells; at the highest angles of attack the count increases modestly due to the enlarged wake refinement. For the $\alpha = 90°$ case, an additional outer refinement zone (target triangle size $= 3 \times 10^{-2}\,c$), similar in shape and aligned with the flow, brings the total to $\approx 2.42 \times 10^5$ cells.

For the 2D case a grid-convergence study at $\alpha = 0°$ is carried out and discussed in Section 7.3.8.

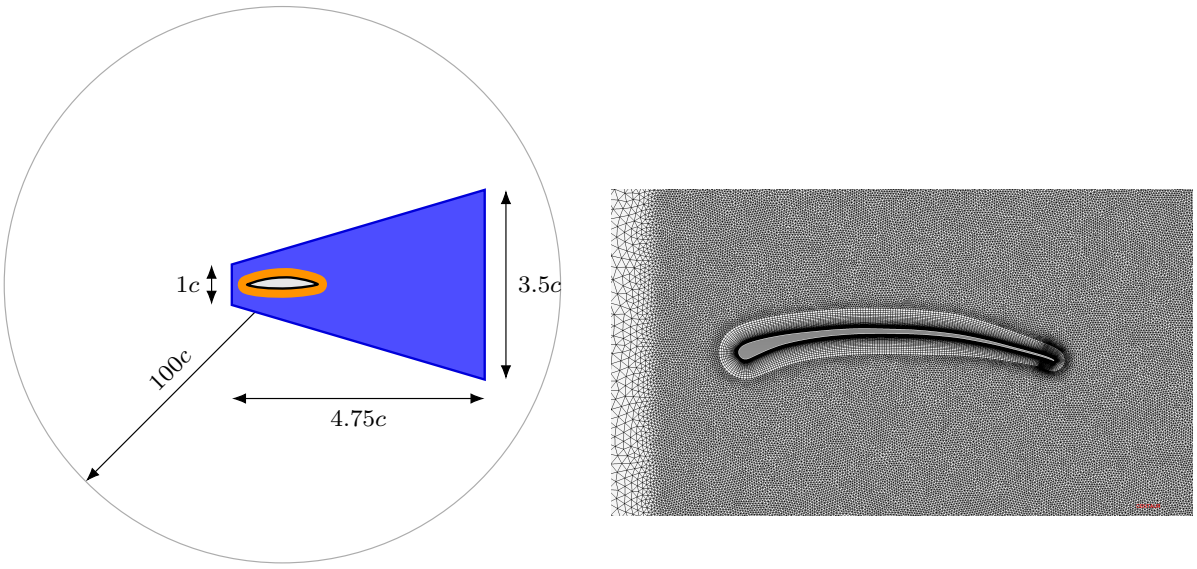

(a) Domain with refinement regions

(b) Zoom of the mesh close to the airfoil

Figure 7.1: Two-dimensional grid structure

7.3.5. Boundary and operating conditions

The setup targets Lilienthal's operating regime. The freestream is set to Ma = 0.035 and Re $= 3.25 \times 10^5$, with chord $c = 0.400\,\text{m}$, which gives $U_\infty \approx 12\,\text{m/s}$ (since $U_\infty = Ma\,a_\infty$

with $a_\infty \approx \sqrt{\gamma R T_\infty}$ at $T_\infty = 293.15\,\mathrm{K} = 20\,^\circ\mathrm{C}$).

In the simulations, Ma, Re, and T_∞ are prescribed; p_∞, ρ_∞, and ν_∞ follow from these choices (ideal-gas relation and the selected viscosity model). For reference, values used are $T_\infty = 293.15\,\mathrm{K}$, $\rho_\infty = 1.2271\,\mathrm{kg/m^3}$, and the implied $p_\infty \approx 103.24\,\mathrm{kPa}$; $\nu_\infty \approx 1.478 \times 10^{-5}\,\mathrm{m^2/s}$ is consistent with $\mathrm{Re} = U_\infty c/\nu_\infty$.

An O-type subsonic farfield is imposed on the circular outer boundary at radius $100\,c$. The farfield prescribes $(\mathrm{Ma}, \alpha, T_\infty)$; the target Re is matched by the pair (U_∞, ν_∞) implied by (Ma, T_∞) and the viscosity model. The airfoil surface is a viscous no-slip, adiabatic wall.

The angle of attack α is varied according to the case list below, following the range tested by Lilienthal with the whirling-arm apparatus, with a denser sampling near typical aerodynamic angles where steady RANS is more reliable ($\alpha \in [-10^\circ, 10^\circ]$):

$$\alpha \in \{-15^\circ, -12^\circ, -10^\circ, -7^\circ, -5^\circ, -3^\circ, -1^\circ, 0^\circ, 1^\circ, 3^\circ, 5^\circ,$$
$$7^\circ, 10^\circ, 12^\circ, 15^\circ, 20^\circ, 30^\circ, 40^\circ, 45^\circ, 60^\circ, 90^\circ\}.$$

7.3.6. Velocity/Mach-number sensitivity

The present regime (very low Ma and moderate Re) can be numerically and physically delicate for steady RANS: low-Mach effects impact numerics, and small changes in U_∞ (thus Ma and Re) can alter separation-bubble size, pressure recovery, and transition location; these effects primarily affect C_D, while C_L and C_M show smaller variation [47, 48]. To quantify this, several (Ma, Re) combinations near Lilienthal's range are compared at $\alpha = 0^\circ$; the final choice $\mathrm{Ma} = 0.035$, $\mathrm{Re} = 3.25 \times 10^5$ is then adopted for the study.

$U_\infty \approx$	Ma	Re	C_L	C_D	C_M
6 m/s	0.017	1.5795×10^5	0.99213	0.02599	0.03633
12 m/s	0.035	3.2500×10^5	1.01965	0.02223	0.03789
17 m/s	0.050	4.6456×10^5	1.03237	0.02044	0.03887
26 m/s	0.075	6.9683×10^5	1.10738	0.01511	0.04293
34 m/s	0.100	9.2911×10^5	1.12283	0.01378	0.04368
69 m/s	0.200	1.8582×10^6	1.15244	0.01233	0.04471

Table 7.1: Sensitivity to Ma and Re at $\alpha = 0^\circ$

As Ma and Re increase, C_L increases moderately while C_D decreases substantially.

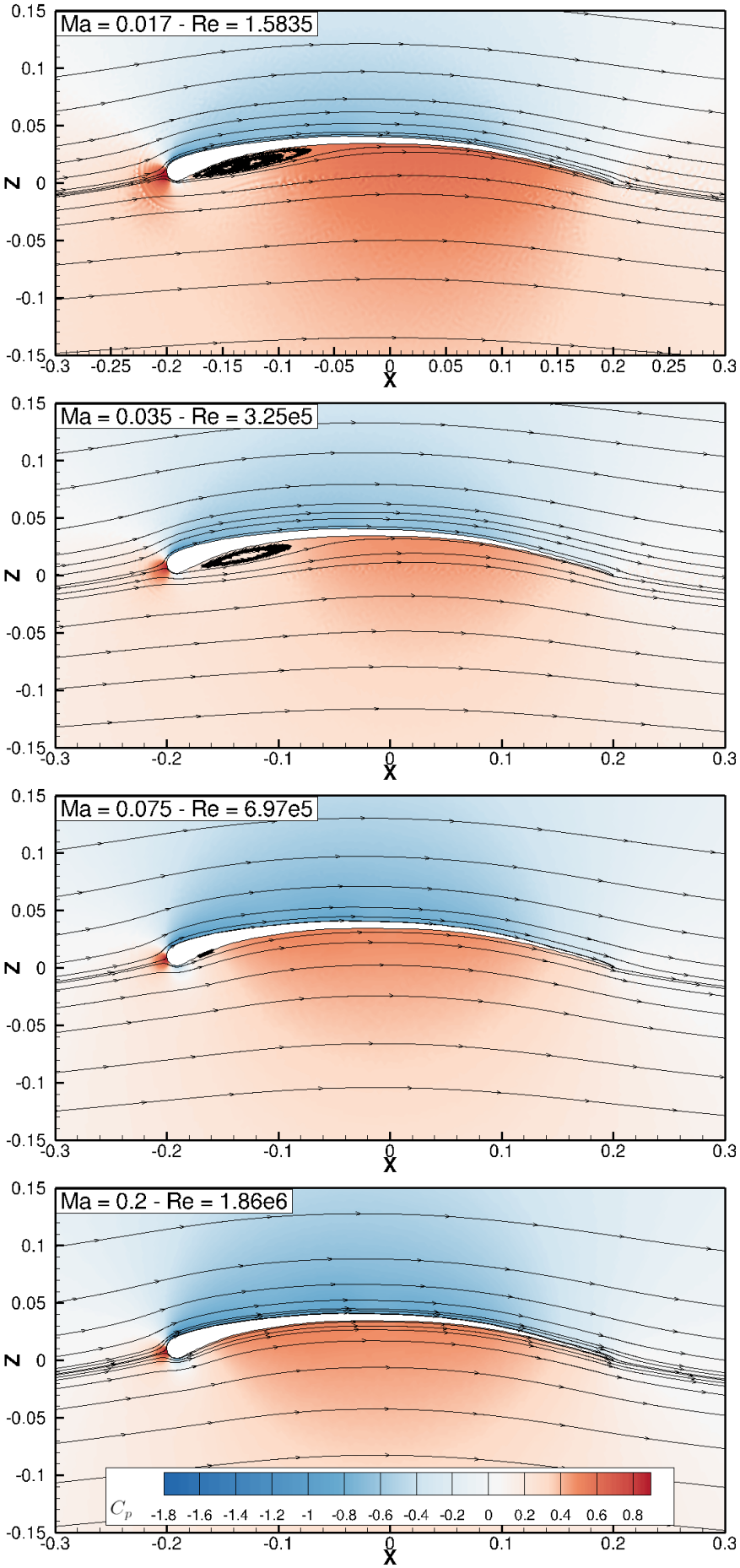

Figure 7.2: C_p at $\alpha = 0°$ for different (Ma, Re) showing bubble/separation reduction

Across Table 7.1, C_L increases by $\approx 16\%$ and C_D decreases by $\approx 53\%$. The trend is consistent with thinner boundary layers, smaller separation bubbles, and improved pressure recovery at higher Re, while compressibility effects remain limited in the subsonic range ($\mathrm{Ma} \lesssim 0.3$). The drag reduction stems from reduced separation, earlier transition, and a smaller bubble recirculation region (see Fig. 7.2). Since the goal is to reproduce Lilienthal's conditions, $\mathrm{Ma} = 0.035$ and $\mathrm{Re} = 3.25 \times 10^5$ are retained for all production runs. Absolute accuracy, especially in C_D, is not expected in steady 2D RANS, but the chosen operating point keeps the coefficients within a plausible range for comparison with the apparatus data and represents the flow around the airfoil more realistically.

7.3.7. Turbulence model sensitivity

Three RANS models are compared on the same 2D grid: Spalart-Allmaras (SA-neg), k-ω (Menter BSL), and a Reynolds-stress model (RSM). Two angles are tested, $\alpha = 0°$ and $5°$, representing a mildly separated case and an attached one. The stopping criterion is a density residual of 10^{-9} for k-ω and RSM, and 10^{-10} for SA.

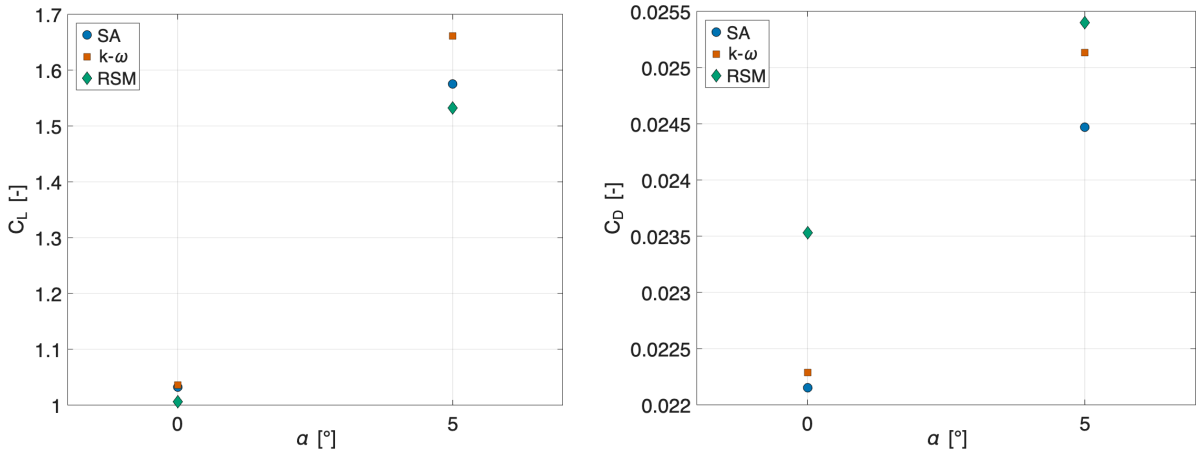

(a) C_L vs. α (b) C_D vs. α

Figure 7.3: C_L and C_D at $\alpha = 0°, 5°$ for three turbulence models: SA, k-ω, RSM

Relative to SA, the differences are:

- $\alpha = 0°$:
  k-ω: $\Delta C_L = +0.33\%$, $\Delta C_D = +0.63\%$;
  RSM: $\Delta C_L = -2.54\%$, $\Delta C_D = +6.23\%$.
- $\alpha = 5°$:
  k-ω: $\Delta C_L = +5.47\%$, $\Delta C_D = +2.71\%$;

RSM: $\Delta C_L = -2.68\%$, $\Delta C_D = +3.80\%$.

SA-neg yields the lowest C_D; this behavior is common in 2D RANS in presence of flow separation, where the separation location and turbulence production are model-sensitive. The differences, however, remain small in this regime. k-ω (BSL) produces slightly higher C_L in both cases, while RSM is probably the more complete model but substantially more expensive and slower to converge, without a clear accuracy advantage here. Given these points, SA-neg is adopted for the remainder of the study.

7.3.8. Grid convergence

In line with CFD verification practice, strict grid independence is not assumed for RANS [46]; instead, discretization effects are quantified via systematic mesh refinement and results are judged "converged within tolerance" [49].

Here, grid studies are performed at $\alpha = 0°$ for the same Ma and Re used elsewhere. The abscissa of the plots in Figure 7.4 reports the total number of grid nodes, N_{nodes}, to allow direct comparison across meshes. To vary the mesh size, successive refinements are introduced as follows:

- the first grid ($N_{\text{nodes}} \approx 2 \times 10^4$), being the coarsest, does not include a refined wake region;
- from the second grid ($N_{\text{nodes}} \approx 3.5 \times 10^4$) up to the seventh ($N_{\text{nodes}} \approx 2.4 \times 10^5$) a refined wake region is added and refined step by step (see Fig. 7.1);
- from the eighth grid onward, a wider rectangular region around the wake is also included; this configuration is carried through up to the finest grid ($N_{\text{nodes}} \approx 1 \times 10^6$), with increased refinements for both regions.

A practical acceptance criterion is defined with respect to the finest SA solution ($N_{\text{nodes}} \approx 1 \times 10^6$), requiring the coefficients on the selected mesh to satisfy:

$$\text{lift: } \pm 2\% \text{ around } C_L^{\text{fine}}, \qquad \text{drag: } \pm 5\% \text{ around } C_D^{\text{fine}}.$$

The tighter band for the C_L reflects its lower grid sensitivity at $\alpha = 0°$; a wider band is allowed for C_D due to its stronger dependence on near-wall resolution and numerical dissipation.

At the end of this study, the mesh with approximately 2.04×10^5 nodes is selected. It lies within both acceptance bands, reproduces the flow features with adequate fidelity (no visible under-resolution in the surface pressure and wake), and avoids the steep increase in

CPU time observed on the next-finer grids.

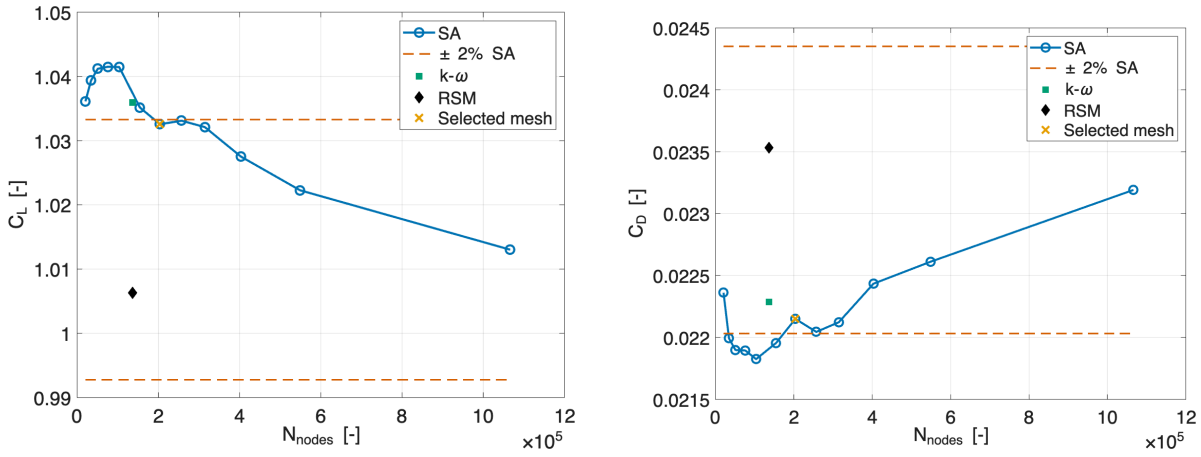

(a) C_L vs. number of nodes

(b) C_D vs. number of nodes

Figure 7.4: Grid convergence assessment in 2D RANS at $\alpha = 0°$

The figure also includes single-point results at $\alpha = 0°$ from k-ω and RSM. Both fall within the same acceptance bands, indicating that, at these conditions, the turbulence-model choice is a secondary effect relative to grid resolution. Although the RSM solution obtained on a much coarser grid ($N_{\text{nodes}} \approx 1.4 \times 10^5$) lies very close to the finest-grid SA values for both C_L and C_D, adopting RSM is not justified: the model incurs substantially higher CPU cost per iteration, the coarse discretization remains under-resolved in the near-wall/wake regions, and the solver converged to density-residual levels of 10^{-9} (SA reached 10^{-10}). Within the chosen acceptance bands, these extra costs and the weaker residual reduction do not provide additional benefit.

GCI convergence. Another way to assess grid convergence is through a three-grid GCI check [49]. Selecting a coarse-medium-fine triplet with $N_{\text{nodes}} = (2.06 \times 10^4, 2.04 \times 10^5, 1.07 \times 10^6)$ and using the 2D mapping $h \propto N_{\text{nodes}}^{-1/2}$ gives refinement ratios $r_{32} = h_1/h_2 \approx 3.15$ and $r_{21} = h_2/h_3 \approx 2.29$. By definition, GCI_{21} estimates the fractional discretization uncertainty of the fine-grid solution (with a safety factor of 1.25). Values of 0.54% (C_L) and 1.43% (C_D) indicate that the fine-grid SA solution is within ≈ 1-1.5% of the grid-converged value; since the medium-fine difference is below the ±2% (lift) and ±5% (drag) acceptance bands, the medium mesh ($N_{\text{nodes}} \approx 2.04 \times 10^5$) delivers the target accuracy at substantially lower cost and is therefore selected.

7.3.9. Results: flow features

These 2D simulations are used to read the flow physics at Lilienthal-like conditions ($V \approx 12\,\mathrm{m/s}$, $\mathrm{Re} \approx 3.25 \times 10^5$, $\mathrm{Ma} \approx 0.035$) around a very thin, cambered profile. Lilienthal tested many shapes, all thin and nearly parabolic to try to "replicate birdflight" [2]. Also, he tested different cambers; the airfoil tested in the CFD simulations has a camber of $f/c = 1/12 \approx 8.3\%$; this high camber airfoil produced the best results in Lilienthal's tests, yielding a large C_{L0}, but also steepens the pressure recovery, promoting earlier separation. Six angles of attack $\alpha \in [-7°, 20°]$ are shown. Angles beyond 20° are omitted because, in steady 2D RANS (SA without transition modeling), post-stall predictions become qualitative and simply grow the same separated topology. The same rationale applies for angles lower than $\alpha = -7°$.

Figure 7.5 shows the normalized speed field $|\vec{u}|/U_\infty$, with streamlines to indicate flow direction and highlight the main features.
At $\alpha = -7°$, the lower surface behaves as the suction side. A large pressure-side separation forms immediately after the rounded LE and produces a broad recirculation region below the airfoil with $|\vec{u}|/U_\infty \approx 0.2$-$0.4$. This follows from the high curvature and adverse pressure gradient ($dp/ds > 0$ along the surface) encountered as the flow turns around the nose at negative incidence.
As α increases, the lower-side bubble shrinks. At $\alpha = 0°$ the flow becomes almost attached; a short separation bubble forms on the lower surface immediately behind the LE and reattaches around mid-chord. Over the airfoil the flow is almost attached, with a presence of a small separation pocket at the TE.
At $\alpha = 3°$ the bubble is largely suppressed; the boundary layer remains attached over most of the chord and the wake becomes very thin. This angle of attack is near the best-attached condition in the series. Up to $\alpha \approx 5°$ (not shown) the flow topology remains similar; mostly attached with minimal TE separation.
By $\alpha = 7°$ the LE suction peak is stronger and the downstream adverse pressure gradient on the upper (suction) side thickens the BL; a weak TE separation initiates, with streamlines lifting from the surface at $x/c \approx 0.7$-0.8.
At $\alpha = 12°$ the shear layer lifts off earlier on the suction side, the dominant separated region expands from mid-chord, and a recirculation bubble starts forming at the TE. The wake thickens markedly, consistent with rising drag, while lift can still increase because of the strong LE suction. In fact this angle shows the highest C_{L} for these simulations (see Sec. 7.3.10).
At $\alpha = 20°$ the airfoil is in deep stall conditions. The shear layer separates at the LE and does not reattach over the chord. A primary LE-anchored recirculation lobe covers

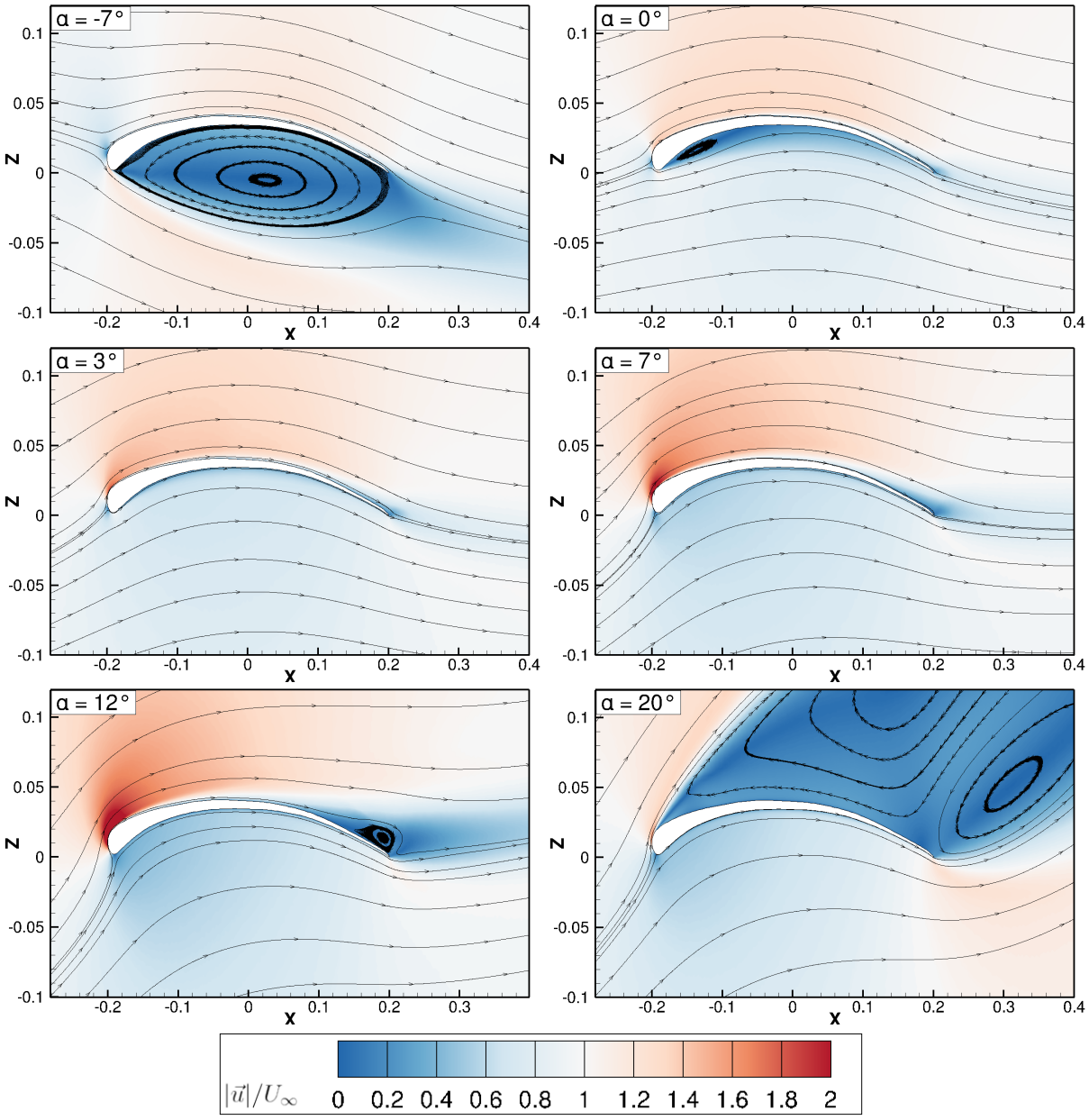

Figure 7.5: $|\vec{u}|/U_\infty$ and streamlines at various α

most of the suction side with a near-stagnant core ($|\,\vec{u}\,|/U_\infty \ll 1$); a secondary TE bubble, already present at lower α, persists beneath the main shear layer and grows in size.

As a vorticity-based complement to the $|\,\vec{u}\,|/U_\infty$ maps, the signed, non-dimensional vorticity normal to the (x, z) plane is:

$$\omega^\star = \omega_y \frac{c}{U_\infty}, \qquad \omega_y = \frac{\partial u}{\partial z} - \frac{\partial w}{\partial x} \tag{7.4}$$

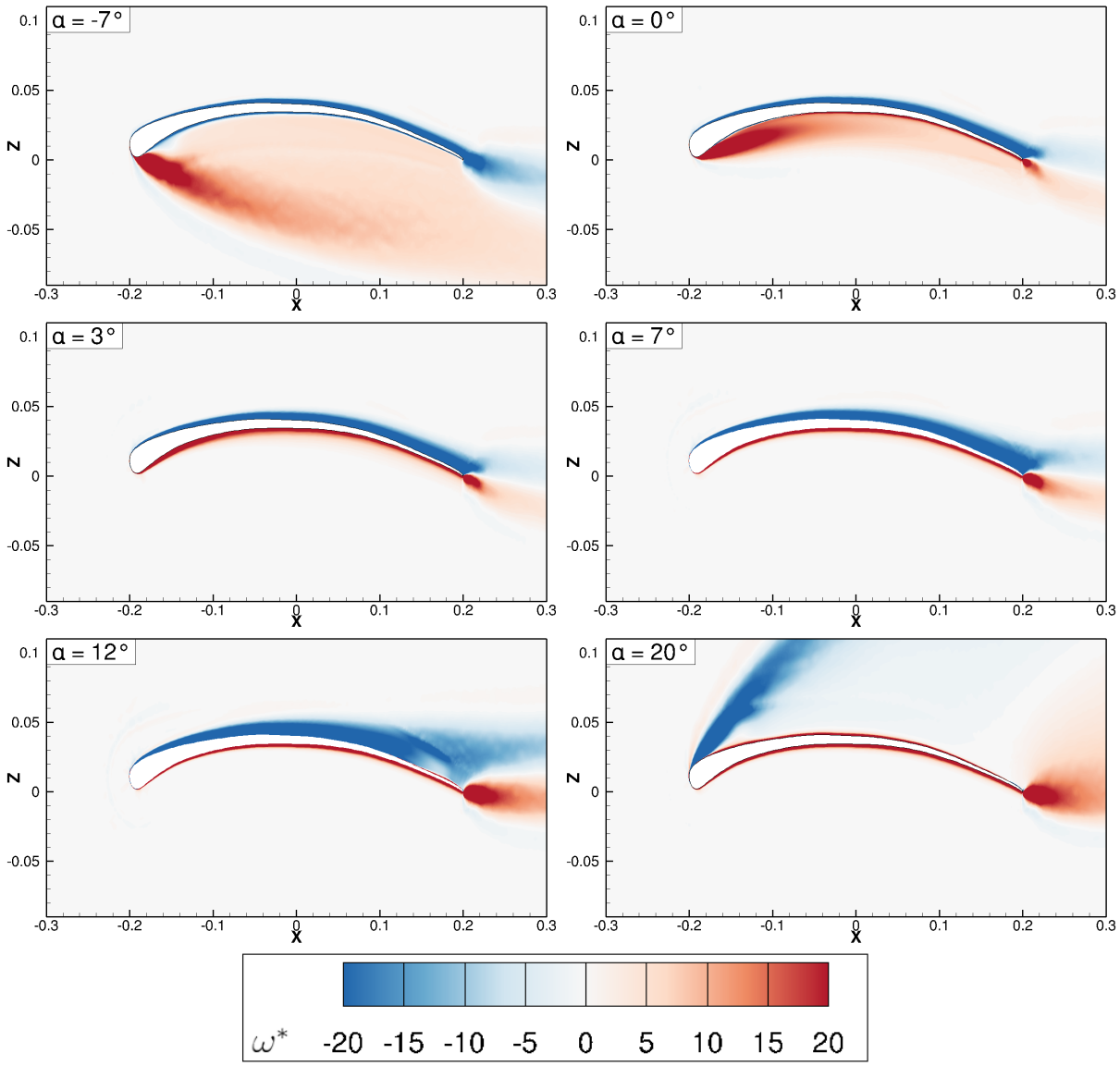

Figure 7.6: Non-dimensional vorticity $\omega^\star = \omega_y c/U_\infty$ at different α. A diverging blue-red colormap is centered at 0 with symmetric limits $\omega^\star \in [-20, 20]$

with $u \equiv U_x = \vec{u}\cdot\hat{\imath}$ and $w \equiv U_z = \vec{u}\cdot\hat{k}$. Large $|\,\omega^\star\,|$ highlights shear layer presence (BLs, separated shear layers, wake). This scaling makes cases comparable across incidences. Positive/negative values mark clockwise/counterclockwise rotation in the (x, z) plane.

Figure 7.6 organizes the shear features already hinted by Figure 7.5.
At $\alpha = -7°$ a strong sheet of one sign runs along the lower surface and spreads downstream with the pressure-side separation, while a thinner opposite-signed sheet forms on the upper side. A broad region of $\omega^\star$ core below the airfoil matches the large recirculation seen in $|\,\vec{u}\,|/U_\infty$.

At $\alpha = 0°$ both boundary layers become thinner. A small near-nose pocket on the lower surface closes around mid-chord ($x/c \approx 0.5$) and continues as a thin BL that evolves into the wake. The wake is narrower, consistent with the more attached flow at this incidence.
At $\alpha = 3°$ the BL sheets are nearly symmetric and compact along most of the chord; the wake stays slender and no separation is evident. This is the cleanest attached case and aligns with the highest value of L/D in the polars (see Fig. 7.8).
At $\alpha = 7°$ the suction-side sheet intensifies and thickens toward the TE. A TE separation is visible just upstream of the trailing edge.
At $\alpha = 12°$ the suction-side shear layer lifts earlier and remains energetic along mid-chord. A TE recirculation bubble is clear. The wake widens, consistent with the drag rise while lift is still high.
At $\alpha = 20°$ a deep stall pattern is reached. A strong LE-anchored sheet peels off and does not reattach. A large separated lobe covers most of the suction side. Unlike the attached cases, the BL does not maintain the usual opposite-sign pattern on the two sides of the airfoil. The persistent TE bubble is still visible and larger than at 12°.

7.3.10. Results: aerodynamic coefficients and polars

Figures 7.7–7.8 report the aerodynamic coefficients at $\mathrm{Re} = 3.25 \times 10^5$ and $\mathrm{Ma} = 0.035$ for the thin, cambered section tested by Lilienthal, computed with 2D RANS over the full incidence range. The panel with $\alpha \in [-15°, 90°]$ shows the overall trends, while the zoom on $\alpha \in [-15°, 15°]$ focuses on the aerodynamically useful range.

Results beyond $\alpha \approx 15°$ are less trustworthy in steady 2D RANS: the absence of transition modeling and the intrinsically 3D nature of turbulence lead to qualitative trends that mainly show the growth of separation and wake thickness. In the attached regime, C_D is generally underpredicted in 2D (fully-turbulent SA), whereas the C_L trends are more robust and comparable with the *Rundlaufapparat* measurements normalized with the modern definition $q = \frac{1}{2}\rho V^2$ (see Section 5.2.5).

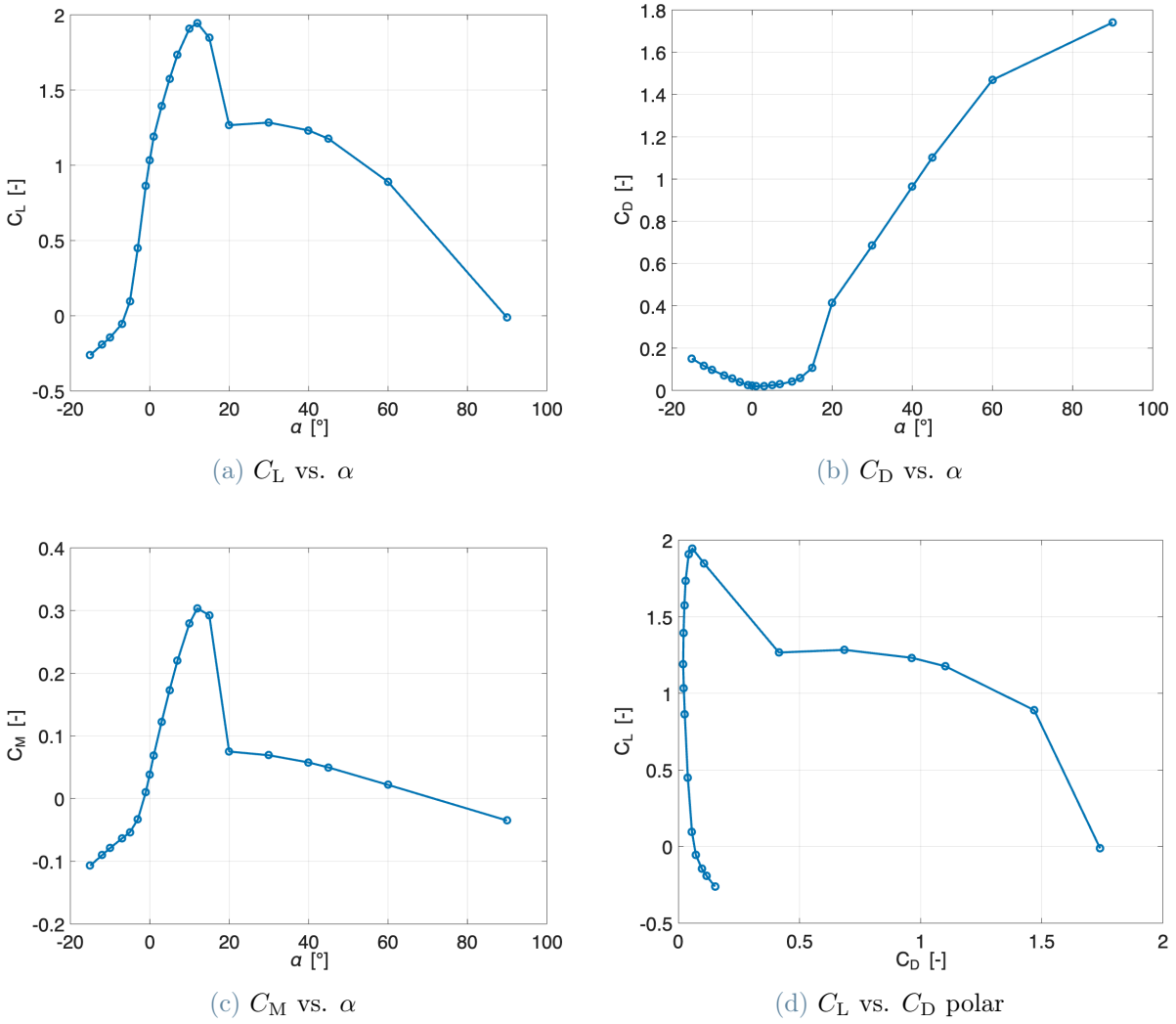

(a) C_L vs. α

(b) C_D vs. α

(c) C_M vs. α

(d) C_L vs. C_D polar

Figure 7.7: Aerodynamic coefficients from 2D RANS over the full angle range $\alpha \in [-15°, 90°]$ at $\mathrm{Re} = 3.25 \times 10^5$, $\mathrm{Ma} = 0.035$

The results for $\alpha \in [-15°, 15°]$ are shown separately in Figure 7.8 to present the polars in a classical aerodynamic range and to interpret the forces generated by Lilienthal's section. In this range the $C_\mathrm{L}(\alpha)$ curve is nearly linear from about $-5°$ to $7°$. By linear interpolation of the points at $-7°$ and $-5°$, the zero-lift angle is $\alpha_{\mathrm{L}=0} \approx -6.3°$, consistent with the high camber. Lift peaks at $C_{\mathrm{L,max}} = 1.9457$ at $\alpha = 12°$; past this angle C_L decreases and C_D rises sharply, in agreement with the separation patterns discussed in Section 7.3.9. The minimum drag is $C_{\mathrm{D,min}} = 0.0193$ at $\alpha = 1°$. Detailed drag levels in attached conditions are less reliable in steady 2D RANS without transition and 3D effects and tend to be underpredicted; as a result, direct numerical agreement with Lilienthal's results is unlikely without 3D and transition modeling. By contrast, the C_L values fall in a range comparable to the *Rundlaufapparat* results when normalized with $q = \frac{1}{2}\rho V^2$ (Section 5.2.5). The

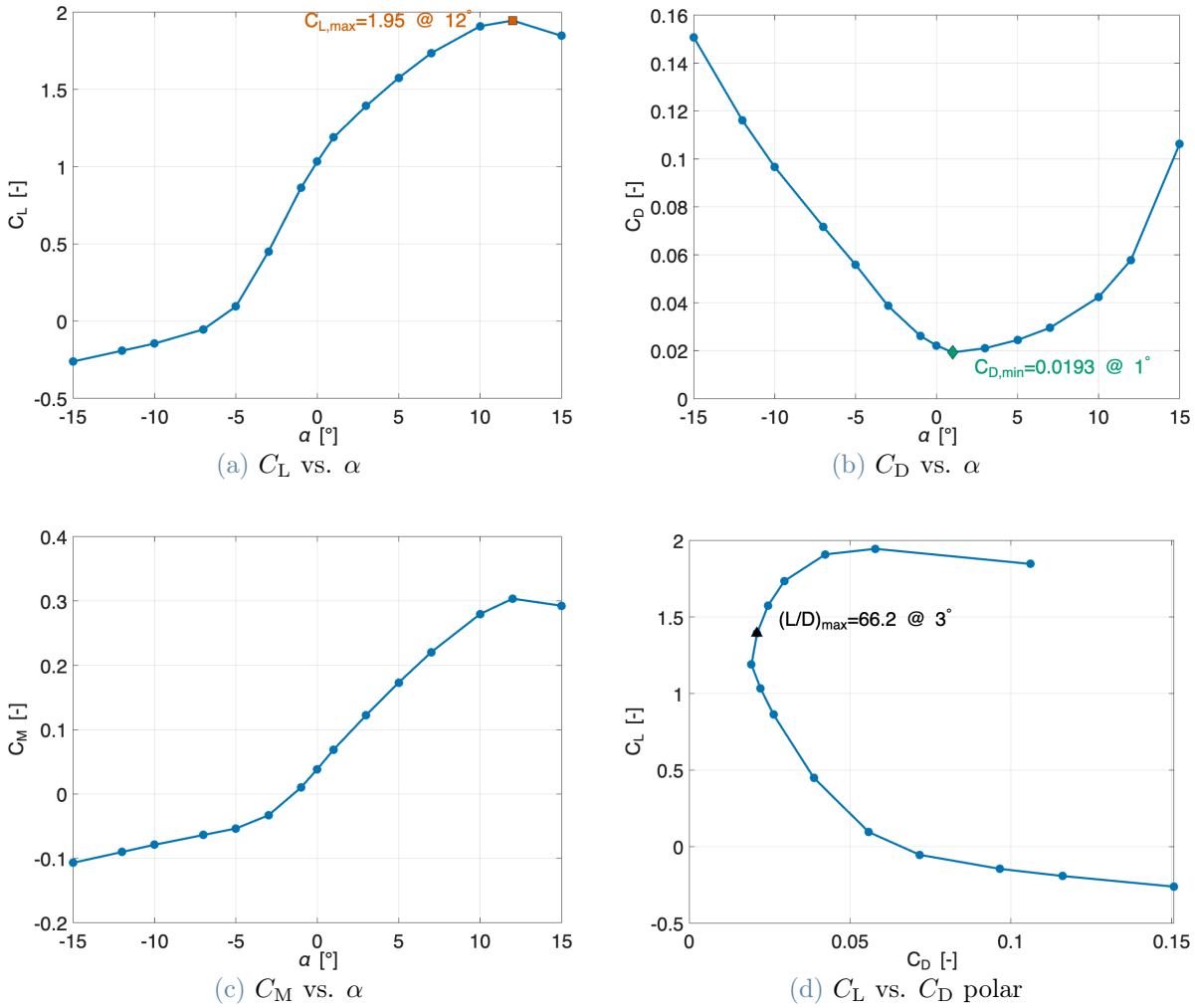

(a) C_L vs. α (b) C_D vs. α

(c) C_M vs. α (d) C_L vs. C_D polar

Figure 7.8: Aerodynamic coefficients in the classical pre-stall range $\alpha \in [-15°, 15°]$

pitching moment is approximately linear from $\alpha \approx -5°$ to $\alpha \approx 12°$ and then decreases in magnitude after stall, reflecting the center-of-pressure shift and tracking the lift behavior.

7.4. 3D simulations

7.4.1. Computational domain and mesh

Hybrid unstructured grids are generated with the commercial software CENTAUR™. As in the 2D case, the outer boundary is an O-type (circular) farfield of radius $100\,c$ (unstructured interior with O-type outer contour).

Near the wing, a structured boundary-layer (BL) stack of anisotropic hexahedral layers is

used to resolve the wall region:

$$N_{\mathrm{BL}} = 25, \qquad \Delta y_1 = 7.5 \times 10^{-6}\ \mathrm{m}, \qquad \text{growth factor} \quad g_{\mathrm{BL}} = 1.25.$$

The target is $y^+ \leq 1$ for all tested α [46]. In 3D, maintaining $y^+ < 1$ everywhere is more challenging; therefore a maximum $y^+ \approx 1.2$ is accepted in some cases (small effect on C_f and τ_w; acceptable for SA wall-resolved). Consequently, the first-layer height and the BL growth factor are larger than in 2D.

Given the higher computational cost than in 2D, no dedicated wake refinement and no formal grid-convergence study are performed. To retain good near-wall resolution, a fine surface mesh is used ($N_{\mathrm{nodes,surface}} \approx 4.1 \times 10^4$), for a total of $N_{\mathrm{nodes}} \approx 1.49 \times 10^6$ in the full grid.

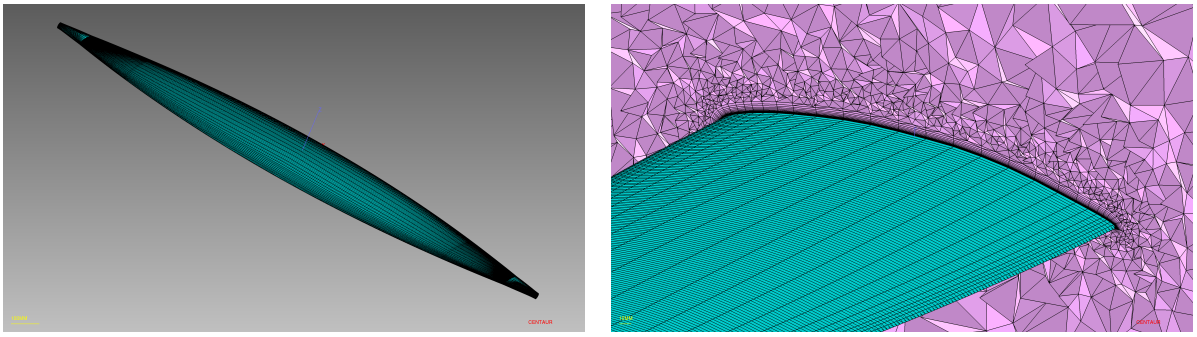

(a) Surface mesh (b) BL and domain mesh-cut at mid-span

Figure 7.9: Three-dimensional grid structure

7.4.2. Boundary and operating conditions

The setup targets Lilienthal's operating regime. The free stream is set to Ma = 0.035 and Re = 3.25×10^5. For reference, $T_\infty = 293.15\,\mathrm{K}$ and $\rho_\infty = 1.2271\,\mathrm{kg/m^3}$ imply $p_\infty \approx 103.24\,\mathrm{kPa}$; the resulting $\nu_\infty \approx 1.478 \times 10^{-5}\,\mathrm{m^2/s}$ is consistent with $\mathrm{Re} = U_\infty c/\nu_\infty$. An O-type subsonic farfield is imposed on the circular outer boundary at radius $100\,c$. The farfield prescribes $(\mathrm{Ma}, \alpha, T_\infty)$; the target Re is matched by the pair (U_∞, ν_∞) implied by (Ma, T_∞) and the viscosity model. The wing surface is a viscous, no-slip, adiabatic wall.

The angle of attack α is varied according to the case list below, following the range tested by Lilienthal with the whirling-arm apparatus, with a denser sampling near typical

aerodynamic angles, where steady RANS is more reliable ($\alpha \in [-10°, 15°]$):

$$\alpha \in \{-15°, -12°, -10°, -7°, -5°, -3°, 0°, 2°, 3°, 5°, \\ 7°, 10°, 12°, 15°, 20°, 30°, 40°, 45°, 60°, 90°\}.$$

7.4.3. Results

The 3D simulations, still subject to the usual RANS limitations, capture flow separation and turbulence more realistically as inherently three-dimensional effects. As a result, the C_L values are a little lower than in 2D ($C_{L,max} = 1.60$ in 3D vs. $C_{L,max} = 1.95$ in 2D) due to finite-span downwash and spanwise relief of the suction peak near stall. The difference in the C_D is even higher ($C_{D,min} = 0.0866$ in 3D vs. $C_{D,min} = 0.0193$ in 2D). Because both 2D and 3D cases use SA (fully turbulent, no transition), profile drag at low Re is often underpredicted; the extra drag in 3D comes primarily from induced drag, $C_{D,i} = C_L^2/(\pi\, AR\, e)$, and tip losses. Any increase in profile drag from 3D effects (spanwise flow, tip-region thickening) is secondary.

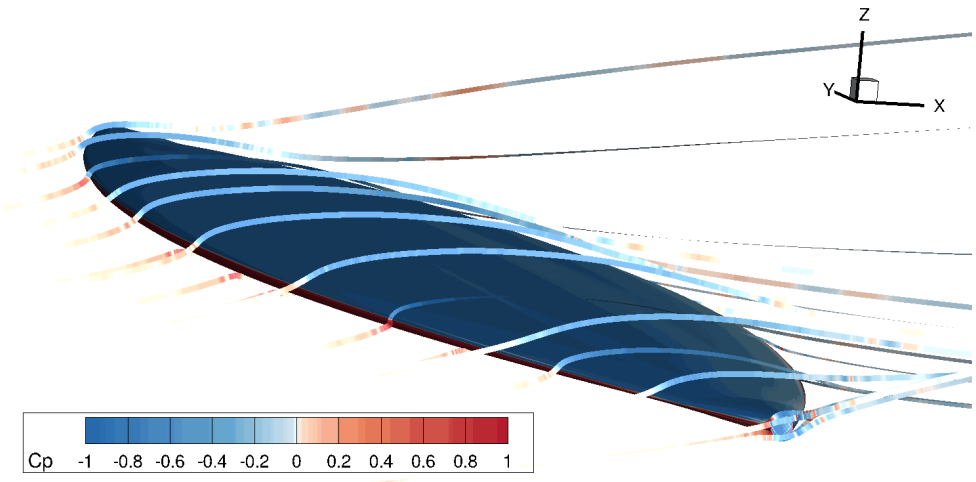

Figure 7.10: Pressure coefficient C_p on the wing with streamtraces at $\alpha = 7°$

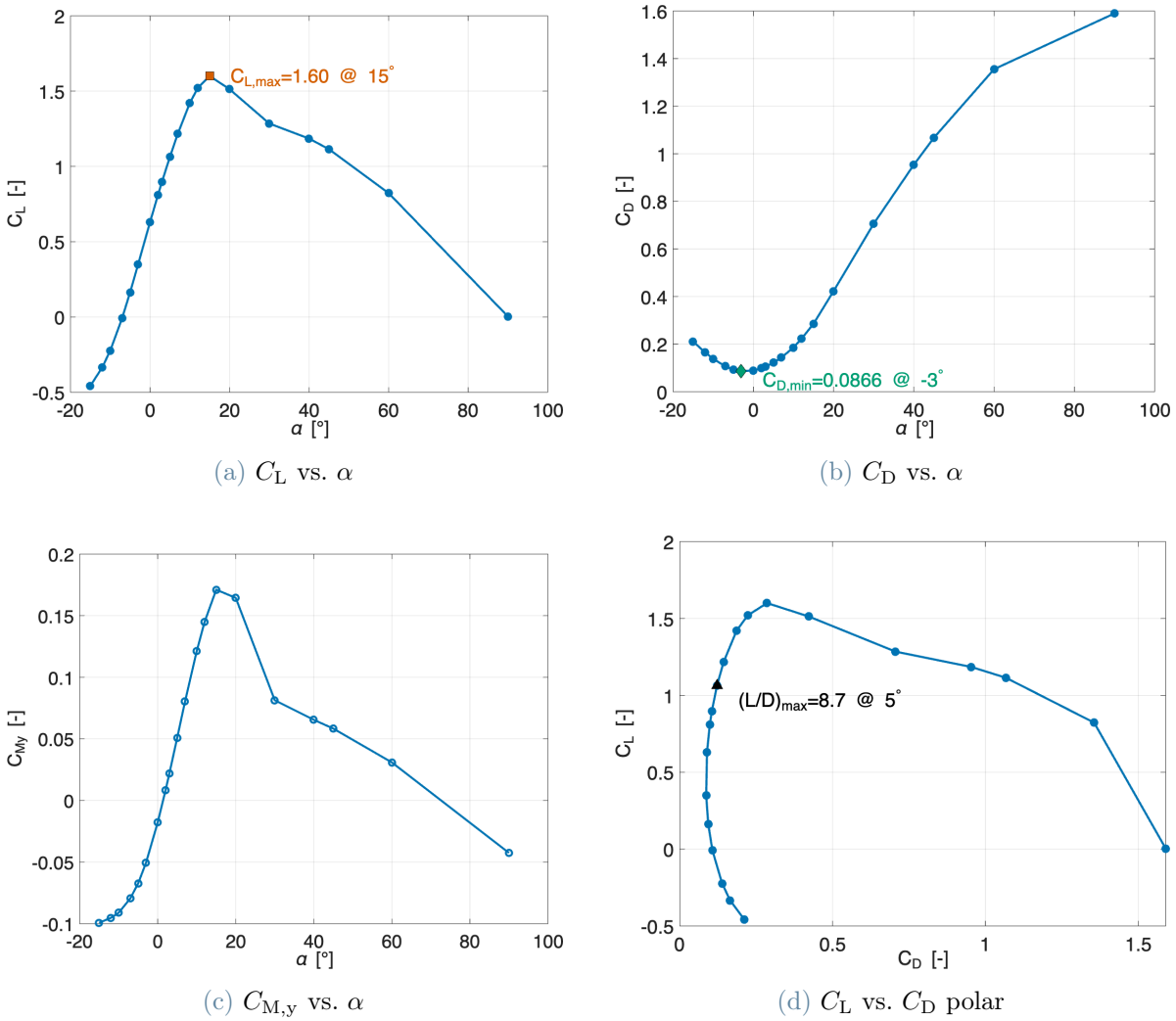

(a) C_L vs. α

(b) C_D vs. α

(c) $C_{\mathrm{M,y}}$ vs. α

(d) C_L vs. C_D polar

Figure 7.11: Aerodynamic coefficients from 3D RANS simulations

7.5. Comparison with *Rundlaufapparat* results

3D simulations enable a direct comparison with the tests on the *Rundlaufapparat*, both Lilienthal's original measurements and those obtained from the modern reconstruction. Figure 7.12 overlays the 3D RANS results and the whirling-arm device measurements (see Sec. 5.2.5, baseline formulation without friction) on Plate IV of Lilienthal's results [2]. All coefficients are presented using Smeaton's normalization $D = k\,S\,V^2$, with the value of k adopted by Lilienthal ($k = 0.13\,\mathrm{kgf/[m^2\,(m/s)^2]}$ and converted to $\mathrm{N/[m^2\,(m/s)^2]}$ when needed).

The simulations tend to underestimate drag, consistent with the known limitations of RANS in separated and turbulent regimes. By contrast, lift agrees well, with the three

curves yielding similar $C_L(\alpha)$. The values measured at $\alpha = 90°$ do not coincide; this is most likely because Lilienthal did not evaluate this angle of attack from direct force measurements, but applied Smeaton's equation (Eq. 4.17), thereby implicitly enforcing $C_D = 1$ and $C_L = 0$ at 90° across his plates.

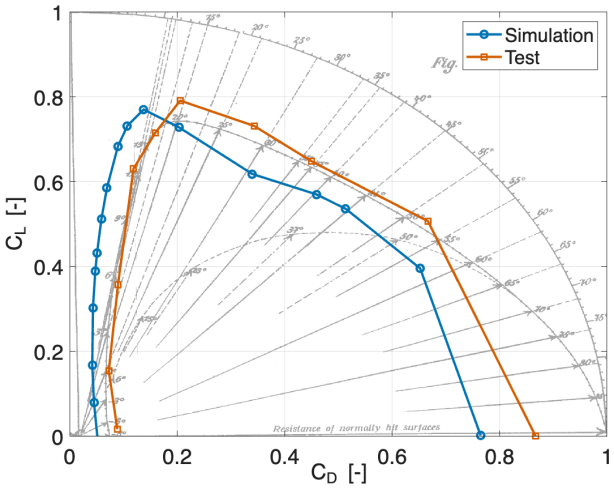

Figure 7.12: 3D simulations and *Rundlaufapparat* tests compared with Lilienthal's results via Smeaton normalization ($D = k\,S\,V^2$, $k = 0.13$)

The test results of the whirling-arm device are also reported using the classical definitions of C_L and C_D (based on dynamic pressure $q = \frac{1}{2}\rho V^2$), as already shown in Section 5.2.5, enabling direct comparison with the CFD coefficients without adopting Smeaton's formula. For consistency, a single air density value is assumed for the test data, $\rho = 1.20\,\mathrm{kg/m^3}$, matching the value used for the results in Section 5.2.5 and for the model analysis in Section 5.3.

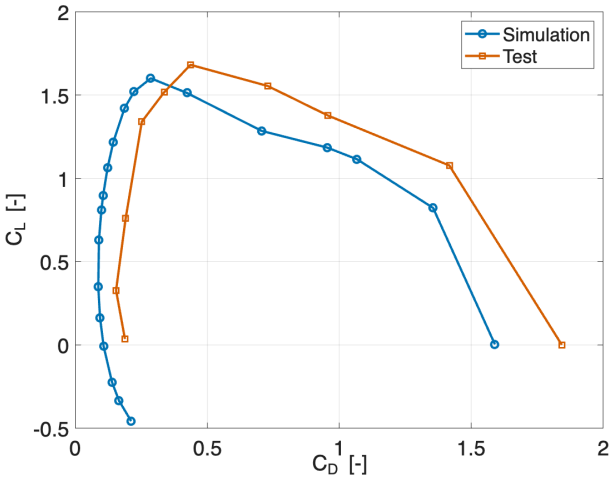

Figure 7.13: Comparison of 3D simulations and modern *Rundlaufapparat* tests using classical aerodynamic coefficients

7.6. Global comparison of lift-drag polars

All the results from the modern *Rundlaufapparat* tests (Sec. 5.2.5), the wind-tunnel measurements (Sec. 6.4), and the 3D RANS simulations (Sec. 7.4) are overlaid on Lilienthal's whirling-arm results [2, Pl. IV]. The datasets agree on the pre-stall trend, the angle of $C_{\mathrm{L,max}}$ and stall onset, and the occurrence of the minimum drag $C_{\mathrm{D,min}}$ at small positive incidence. The main discrepancies are: lower absolute magnitudes in the wind-tunnel data (lower Re, open-jet/support losses), systematically lower C_{D} in the 3D RANS simulations, and the 90° case, where Lilienthal imposed Smeaton's equation (see Eq. 4.17) rather than direct force measurements.

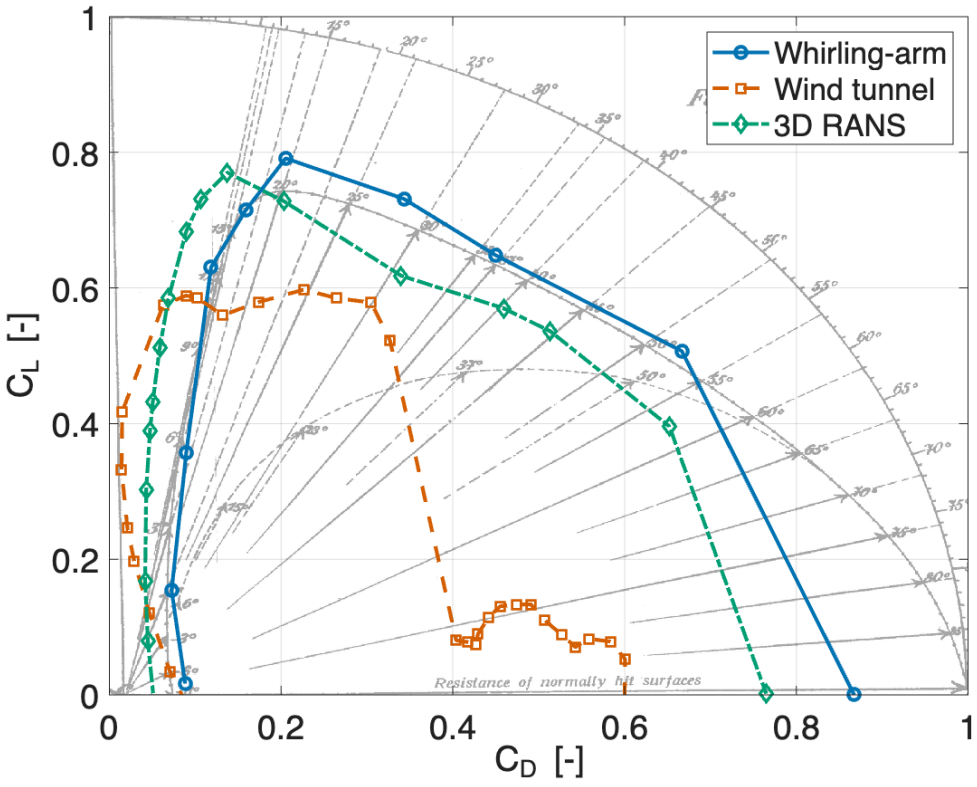

Figure 7.14: Global lift-drag polar: modern whirling-arm tests, wind-tunnel tests, and 3D RANS overlaid on Lilienthal's Plate IV (Smeaton normalization $D = kSV^2$, $k = 0.13$)

8 | Conclusions

This work revisits Otto Lilienthal's whirling-arm experiments and treats the *Rundlaufapparat* as a quantitative bridge between early rotating tests and modern aerodynamic practice. His investigations inaugurated the systematic measurements of wing aerodynamics and the early engineering of flight: by linking geometry, incidence, and force through controlled tests, he helped establish concepts that still frame today's understanding of lift and drag. Building on a faithful reconstruction of the *Rundlaufapparat*, this study clarifies the device's kinematics and measurement chain, how Lilienthal operated it and defined the forces, and how the flow develops over cambered wings under Lilienthal-like operating conditions. To support the interpretation of the results, rotating-arm measurements are compared with RANS simulations and wind-tunnel data, so that historical procedure, modern analysis, and flow physics converge into a single, coherent picture. The modern reimplementation confirms that Lilienthal's framework remains intelligible and testable.

At DLR in Göttingen, the apparatus was reconstructed as faithfully as practicable to Lilienthal's intent while exposing the details required for calibration and repeatability. The device response was mapped across applied masses, with and without wings, and across angles of attack, and the measured kinematics were linked to the force data. On this basis, the study characterizes the drop dynamics, quantifies the accelerating segment, and verifies the presence of a steady or quasi-steady window, which is essential for reliable force measurements. The study also determines the number of turns required for repeatable results, quantifies loss mechanisms, and evaluates the sensitivity of the results to these variables. A MATLAB model of the apparatus reproduces the measured kinematics, supports parameter identification on arms-only and wings-on runs, and validates the force definition protocol applied to the measurements.

From the reconstructed apparatus, a measurement campaign was carried out following Lilienthal's procedure. Known masses and recorded drop histories were converted into forces and coefficient ratios through a consistent processing workflow that accounts for alternative coefficient definitions and friction treatments. Arms-only tests at multiple loads yield a drag-plus-friction curve as a function of mean tangential speed (or, equivalently,

drop time) over $V \in [1.5, 12]\,\mathrm{m/s}$, reproducing the relationship at the core of Lilienthal's analysis. For the wings-on configuration, the work ranged from load characterization, with applied mass $m \in [5, 20]\,\mathrm{kg}$, to a dedicated campaign constructing the C_L vs. C_D polar in Lilienthal's sense. Alternative historical coefficient formulations attributed to Lilienthal were derived and checked against the data, clarifying where definitions differ and which adaptations he may have applied. The resulting $C_\mathrm{L}(\alpha)$ and $C_\mathrm{D}(\alpha)$ curves align with wind-tunnel and CFD trends. An uncertainty analysis quantifies contributions from timing, calibration, and loss identification. Overall, the campaign shows that Lilienthal's method, despite being subject to limitations and potential errors, is operationally reproducible and quantitatively consistent when implemented with modern instrumentation and definitions, and its principal inferences remain valid.

Historical coefficient conventions were evaluated on the same datasets to separate definition effects from measurement effects. Applying the Smeaton coefficient (in its different historical values), normalizing by the drag at 90°, and using the modern dynamic-pressure definition change absolute magnitudes but preserves the trends with angle of attack and the lift-to-drag ratio. When Lilienthal's historical method is followed step by step, the resulting effective Smeaton coefficient k is close to the constant reported by Smeaton and adopted by Lilienthal, yielding $k = 0.11276\,\mathrm{kgf}/[\mathrm{m}^2(\mathrm{m/s})^2]$, although it is not equivalent to the modern dynamic-pressure scaling. Lilienthal's method is therefore coherent within its historical context: it converts masses to forces and comparative coefficients consistently, even if the numbers are not directly comparable with modern definitions. In practice, this provides a straightforward mapping from historical to modern terms without altering the underlying physics.

Beyond the rotating-arm tests, complementary studies were performed to resolve the flow and assess the scope of Lilienthal's findings. An open-jet wind-tunnel campaign at DLR RTG on a scaled reproduction of a Lilienthal wing provided independent force measurements; in parallel, 2D and 3D RANS simulations were used to visualize and interpret the flow physics over the same operating range tested by Lilienthal ($\mathrm{Ma} = 0.035$, $\mathrm{Re} = 3.25 \times 10^5$). Both studies covered the incidence range used by Lilienthal, enabling comparison with both present and historical rotating-arm data. Across methods the observations are consistent: a large leading-edge separation bubble is present at slightly negative incidence ($\alpha \approx -10°$) and weakens as α increases toward positive angles; attached flow persists only over a narrow low-incidence band ($3° \leq \alpha \leq 7°$), after which trailing-edge separation develops and thickens; at higher incidence, leading-edge separation forms without reattachment before the trailing edge. Stall in the wind-tunnel and CFD occurs near $\alpha \approx 12°$, whereas the rotating-arm shows lift continuing to increase up to $\alpha = 20°$, reflecting

the different operating conditions (rotating apparatus versus straight-flow conditions in CFD and in the wind tunnel), rather than a contradiction in the underlying physics. Uncertainties for the wind-tunnel and CFD studies are reported to bound the comparisons and to indicate where differences are expected.

Future developments

The following developments would consolidate the present findings, extend the parameter space, and strengthen the bridge between historical and modern aerodynamics:

- Repeat apparatus tests outdoors, as in Lilienthal's original setting, and extend the load set to map sensitivity across operating conditions.
- Systematically vary wing geometry and materials (camber, thickness) under the same protocol to quantify their influence and to cover the full set of Lilienthal's Plates.
- Separate and quantify loss components (rope-disk contact, bearings, aerodynamic drag) with targeted identification tests.
- Use transition-sensitive and time-accurate simulations (URANS, DES/LES) to resolve separation and unsteady features.
- Perform rotating-frame CFD with sliding-mesh or overset (Chimera) grids to replicate the arm kinematics and compute loads directly.
- Conduct higher-precision wind-tunnel campaigns in a closed-section facility to reduce open-jet effects; a full-scale, single-sided mold is already available for testing, and a two-sided mold can be produced to tighten tolerances.

Bibliography

[1] Otto Lilienthal. *Der Vogelflug als Grundlage der Fliegekunst: ein Beitrag zur Systematik der Flugtechnik*. R. Gaertners Verlagsbuchhandlung; Hermann Heyfelder, Berlin, Germany, 1889. doi:https://doi.org/10.3931/e-rara-24491. Erste Auflage (first edition); public-domain scan by ETH-Bibliothek.

[2] Otto Lilienthal. *Birdflight as the Basis of Aviation*. Longmans, Green, and Co., London, UK, 1911. Translated by A. W. Isenthal.

[3] Markus Raffel and Bernd Lukasch. *The Flying Man: Otto Lilienthal–History, Flights and Photographs*. Springer Biographies. Springer, Cham, Switzerland, 2022. ISBN 978-3030950323. doi:https://doi.org/10.1007/978-3-030-95033-0.

[4] Royal Aeronautical Society. The Royal Aeronautical Society: The early years, 2016. URL https://www.aerosociety.com/news/the-royal-aeronautical-society-part-1-the-early-years/. On Wenham and Browning's 1871 wind tunnel.

[5] NASA Glenn Research Center. Wright 1901 Wind Tunnel, 2024. URL https://www.grc.nasa.gov/www/k-12/airplane/wrights/tunnel.html.

[6] Société de la Tour Eiffel. Eiffel Aerodynamics Laboratory, 2025. URL https://gustaveeiffel.com/en/ouvrages/eiffel-aerodynamics-laboratory/.

[7] John A. D. Ackroyd. Sir George Cayley: The Invention of the Aeroplane near Scarborough at the Time of Trafalgar. *Journal of Aeronautical History*, pp. 130–181, 2011. URL https://www.aerosociety.com/media/4862/sir-george-cayley-the-invention-of-the-aeroplane-near-scarborough-at-the-time-of-trafalgar.pdf. Paper No. 2011/6.

[8] John D. Anderson, Jr. *A History of Aerodynamics: And Its Impact on Flying Machines*. Number 8 in Cambridge Aerospace Series. Cambridge University Press, Cambridge, UK, 1997. ISBN 978-0521454353. doi:https://doi.org/10.1017/CBO9780511607158.

[9] Otto-Lilienthal-Museum. Bildarchiv / image archive, 2025. URL https://lilienthal-museum.museumnet.eu/bilder. Image archive; cite Archiv-ID in captions.

[10] James R. Hansen, editor. *The Wind and Beyond: A Documentary Journey into the History of Aerodynamics in America. Volume 1: The Ascent of the Airplane*. Number SP-2003-4409 in The NASA History Series. National Aeronautics and Space Administration, NASA History Office, Office of External Relations, Washington, DC, USA, 2003. ISBN 978-0756743147. URL https://www.nasa.gov/wp-content/uploads/2023/03/sp-4409-vol1.pdf. With D. Bryan Taylor, Jeremy Kinney, and J. Lawrence Lee.

[11] Werner Heinzerling and Helmuth Trischler, editors. *Otto Lilienthal: Flugpionier – Ingenieur – Unternehmer. Dokumente und Objekte*. Deutsches Museum, München, Germany, 1991. ISBN 978-3924183158. URL https://worldcat.org/isbn/9783924183158. Exhibition catalog; Deutsches Museum, 8 May 1991–10 Jan 1992.

[12] Otto-Lilienthal-Museum. Nachlass Lilienthal — Korrespondenzen Otto Lilienthal, 2025. URL https://lilienthal-museum.museumnet.eu/nachlass-lilienthal/korrespondenzen-otto-lilienthal. Document archive; correspondence overview and item list.

[13] Otto Lilienthal. The Flying Man: The Carrying Capacity of Arched Surfaces in Sailing Flight. *Aeronautics*, vol. 1, no. 7, pp. 92–96, April 1894. URL https://invention.psychology.msstate.edu/i/Lilienthal/library/Prog_Lilienthal_Flying.html. Translated from Zeitschrift für Luftschiffahrt und Physik der Atmosphäre (Nov. 1893).

[14] John D. Anderson, Jr. *Fundamentals of Aerodynamics*. McGraw-Hill Education, New York, NY, USA, 5th edition, 2010. ISBN 978-0073398105. URL https://worldcat.org/isbn/9780073398105.

[15] Robert N. McCullough. The Wright Stuff: The Mathematics of the Wright Brothers. In *Following in the Footsteps of the Wright Brothers: Their Sites and Stories (Symposium)*, Dayton, OH, USA, September 2001. Wright State University Libraries, Special Collections & Archives. URL https://corescholar.libraries.wright.edu/following/symposium/program/11/. Presented September 28, 2001.

[16] Markus Raffel, Felix Wienke, and Andreas Dillmann. Flying Qualities of Otto Lilienthal's Large Biplane. *Journal of Aircraft*, vol. 58, no. 2, pp. 413–419, 2021. doi:https://doi.org/10.2514/1.C036022.

[17] Markus Raffel, Felix Wienke, Clemens Schwarz, and Andreas Dillmann. Flight Controls of Otto Lilienthal's Experimental Monoplane from 1895. *Journal of Aircraft*, vol. 59, no. 6, pp. 1616–1625, 2022. doi:https://doi.org/10.2514/1.C037047.

[18] Felix Krimm, Markus R. Ritter, Markus Raffel, Andreas Dillmann, Bernd Lukasch, Peter Busse, and Andreas Hempfer. Otto Lilienthal's Propulsion System for Power Aided

Gliding Flight From 1893–1896. In *AIAA Aviation Forum and ASCEND 2025*, Las Vegas, NV, USA, July 2025. ISBN 978-162410738-2. doi:https://doi.org/10.2514/6.2025-3114. Co-located with AIAA ASCEND 2025.

[19] Markus Raffel, Bernd Lukasch, Peter Busse, Markus Ritter, Thimo von Hören, and Andreas Dillmann. Otto Lilienthal's Ornithopters from 1893 and 1896. In *AIAA SCITECH 2024 Forum*, Orlando, FL, USA, January 2024. ISBN 978-1-62410-711-5. doi:https://doi.org/10.2514/6.2024-2001. Paper 2024-2001.

[20] John Smeaton. An Experimental Enquiry Concerning the Natural Powers of Water and Wind to Turn Mills and Other Machines, Depending on a Circular Motion. *Philosophical Transactions of the Royal Society of London*, vol. 51, pp. 100–174, 1759. doi:https://doi.org/10.1098/rstl.1759.0019.

[21] Library of Congress, Prints and Photographs Division. Prints & Photographs Online Catalog (PPOC). Online catalog, 2025. URL https://www.loc.gov/pictures/. Public domain items; cite specific digital ID in captions.

[22] National Museum of the United States Air Force. Museum Fact Sheets. Official website, 2025. URL https://www.nationalmuseum.af.mil/Visit/Museum-Exhibits/Fact-Sheets/. General fact sheets; match the specific page in captions.

[23] Encyclopaedia Britannica. John Smeaton. Encyclopaedia Britannica, 2025. URL https://www.britannica.com/biography/John-Smeaton.

[24] International Organization for Standardization. Standard Atmosphere. International Standard ISO 2533:1975, ISO, Geneva, Switzerland, 1975. URL https://www.iso.org/standard/7472.html. Amendment 1: 1985; Amendment 2: 1997.

[25] NASA Glenn Research Center. Shape Effects on Drag, 2025. URL https://www.grc.nasa.gov/www/k-12/VirtualAero/BottleRocket/airplane/shaped3.html.

[26] Russell C. Hibbeler. *Engineering Mechanics: Statics*. Pearson, Harlow, UK, 14th edition, 2016. ISBN 978-1292089331.

[27] NOAA, NASA, and USAF. U.S. Standard Atmosphere, 1976. Technical Report NOAA-S/T 76-1562, National Oceanic and Atmospheric Administration; National Aeronautics and Space Administration; U.S. Air Force, Washington, DC, USA, 1976. URL https://www.ngdc.noaa.gov/stp/space-weather/online-publications/miscellaneous/us-standard-atmosphere-1976/us-standard-atmosphere_st76-1562_noaa.pdf.

[28] *PSC-360 Hall-Effect End-of-Shaft Rotary Position Sensor (Datasheet)*. Piher Sensing Systems, 2024. Analog ratiometric; IP67/IP69K.

[29] Abraham Savitzky and Marcel J. E. Golay. Smoothing and Differentiation of Data by Simplified Least Squares Procedures. *Analytical Chemistry*, vol. 36, no. 8, pp. 1627–1639, 1964. doi:https://doi.org/10.1021/ac60214a047.

[30] Richard G. Budynas and J. Keith Nisbett. *Shigley's Mechanical Engineering Design*, chapter 17: Flexible Mechanical Elements. McGraw-Hill, New York, NY, USA, 10th edition, 2015. ISBN 978-0073398204. URL https://worldcat.org/isbn/9780073398204.

[31] Frank P. Bowden and David Tabor. *The Friction and Lubrication of Solids*. Oxford Classic Texts in the Physical Sciences. Oxford University Press, Oxford, UK, 2001. ISBN 978-0198507772. doi:https://doi.org/10.1093/oso/9780198507772.001.0001.

[32] Thomas J. Mueller, editor. *Low Reynolds Number Aerodynamics: Proceedings of the Conference Notre Dame, Indiana, USA, 5–7 June 1989*, volume 54 of *Lecture Notes in Engineering*. Springer, Berlin, Germany, 1989. doi:https://doi.org/10.1007/978-3-642-84010-4.

[33] Joint Committee for Guides in Metrology (JCGM). Evaluation of Measurement Data – Guide to the Expression of Uncertainty in Measurement. Technical Report JCGM 100:2008, BIPM, IEC, IFCC, ILAC, ISO, IUPAC, IUPAP, OIML, Sèvres, France, 2008. URL https://www.bipm.org/documents/20126/2071204/JCGM_100_2008_E.pdf.

[34] Till Schwermer, Kai Richter, and Markus Raffel. Development of a Rotor Test Facility for the Investigation of Dynamic Stall. In *New Results in Numerical and Experimental Fluid Mechanics X*, volume 132 of *Notes on Numerical Fluid Mechanics and Multidisciplinary Design*, pages 663–673. Springer, Cham, Switzerland, 2016. doi:https://doi.org/10.1007/978-3-319-27279-5_58.

[35] Jewel B. Barlow, William H. Rae, Jr., and Alan Pope. *Low-Speed Wind Tunnel Testing*. John Wiley & Sons, New York, NY, USA, 3rd edition, 1999. ISBN 978-0471557746. URL https://www.wiley.com/en-us/Low%2BSpeed%2BWind%2BTunnel%2BTesting%2C%2B3rd%2BEdition-p-9780471557746.

[36] *Multicomponent Dynamometer, Type 9257B*. Kistler Group, Winterthur, Switzerland, 2018. Datasheet. Quartz three-component dynamometer for measuring the three orthogonal components of a force.

[37] Stephen B. Pope. *Turbulent Flows*. Cambridge University Press, Cambridge, UK, 2000. ISBN 9780521598866. doi:https://doi.org/10.1017/CBO9780511840531.

[38] Philippe R. Spalart. Strategies for Turbulence Modelling and Simulations. *In-*

ternational Journal of Heat and Fluid Flow, vol. 21, no. 3, pp. 252–263, 2000. doi:https://doi.org/10.1016/S0142-727X(00)00007-2.

[39] Christopher L. Rumsey. Turbulence Modeling Verification and Validation (Invited). In *52nd AIAA Aerospace Sciences Meeting*, National Harbor, MD, USA, 2014. doi:https://doi.org/10.2514/6.2014-0201.

[40] Philippe R. Spalart and Serge R. Allmaras. A One-Equation Turbulence Model for Aerodynamic Flows. In *30th AIAA Aerospace Sciences Meeting*, Reno, NV, USA, January 1992. doi:https://doi.org/10.2514/6.1992-439. AIAA Paper 1992-0439.

[41] Steven R. Allmaras, Forrester T. Johnson, and Philippe R. Spalart. Modifications and Clarifications for the Implementation of the Spalart–Allmaras Turbulence Model. In *Proceedings of the Seventh International Conference on Computational Fluid Dynamics (ICCFD7)*, Big Island, Hawaii, USA, July 2012. URL https://www.iccfd.org/iccfd7/assets/pdf/papers/ICCFD7-1902_paper.pdf. Paper ICCFD7-1902.

[42] David C. Wilcox. *Turbulence Modeling for CFD*. DCW Industries, La Cañada, CA, USA, 3rd edition, 2006. ISBN 978-1-928729-08-2. URL https://worldcat.org/oclc/77138203.

[43] Florian R. Menter. Two-Equation Eddy-Viscosity Turbulence Models for Engineering Applications. *AIAA Journal*, vol. 32, no. 8, pp. 1598–1605, 1994. doi:https://doi.org/10.2514/3.12149.

[44] Brian E. Launder, Gordon J. Reece, and Wolfgang Rodi. Progress in the Development of a Reynolds-Stress Turbulence Closure. *Journal of Fluid Mechanics*, vol. 68, no. 3, pp. 537–566, 1975. doi:https://doi.org/10.1017/S0022112075001814.

[45] Dieter Schwamborn, Anthony D. Gardner, Heiko von Geyr, Andreas Krumbein, Heinrich Lüdeke, and Arne Stürmer. Development of the TAU-Code for Aerospace Applications. In *50th NAL International Conference on Aerospace Science and Technology (ICAST)*, Bangalore, India, June 2008. URL https://elib.dlr.de/55519/1/INCAST_Schwamborn.pdf. DLR eLib ID: 55519.

[46] Christopher L. Rumsey. Turbulence Modeling Resource: Verification and Validation. NASA Technical Memorandum NASA/TM–2011-215989, NASA Langley Research Center, Hampton, VA, USA, 2011. URL https://turbmodels.larc.nasa.gov/.

[47] Eitan Turkel. Preconditioning Techniques in Computational Fluid Dynamics. *Annual Review of Fluid Mechanics*, vol. 31, no. 1, pp. 385–416, 1999. doi:https://doi.org/10.1146/annurev.fluid.31.1.385.

[48] Hervé Guillard and Christine Viozat. On the Behaviour of Upwind Schemes in the Low Mach Number Limit. *Computers & Fluids*, vol. 28, no. 1, pp. 63–86, 1999. doi:https://doi.org/10.1016/S0045-7930(98)00017-6.

[49] Ibrahim B. Celik, Ugo Ghia, Patrick J. Roache, Carlos J. Freitas, Hugh W. Coleman, and Peter E. Raad. Procedure for Estimation and Reporting of Uncertainty Due to Discretization in CFD Applications. *Journal of Fluids Engineering*, vol. 130, no. 7, pp. 078001, 2008. doi:https://doi.org/10.1115/1.2960953.

A | CAD Drawings

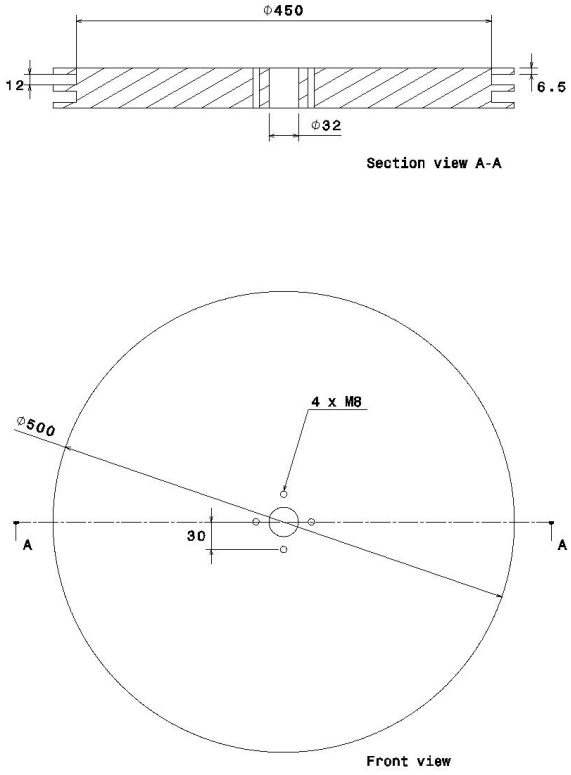

Figure A.1: Drum CAD

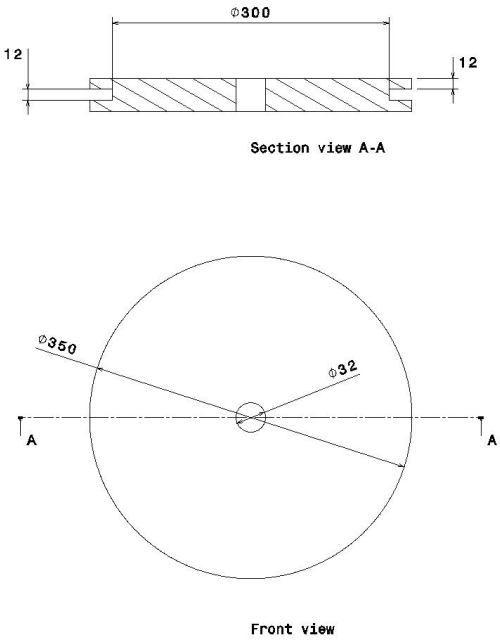

Figure A.2: Pulley CAD

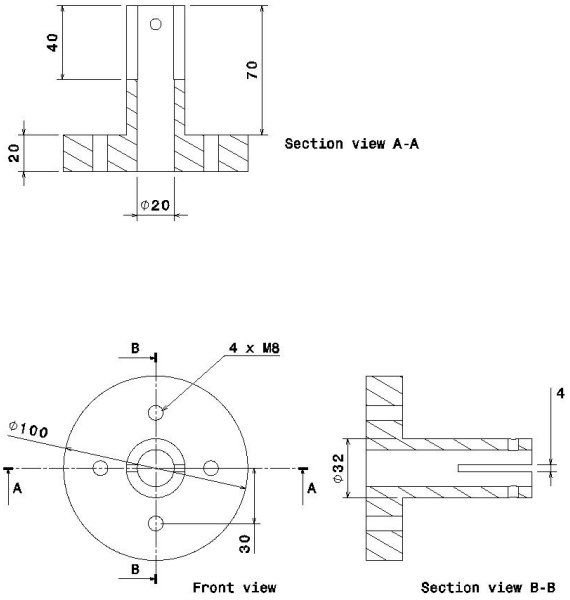

Figure A.3: Flanged spigot adapter CAD

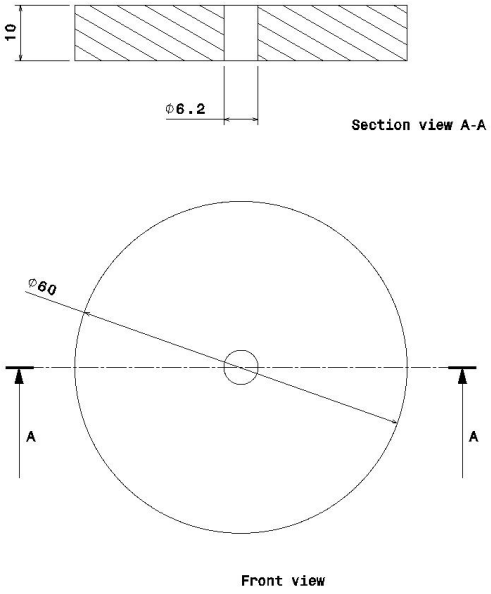

Figure A.4: Sensor disk CAD

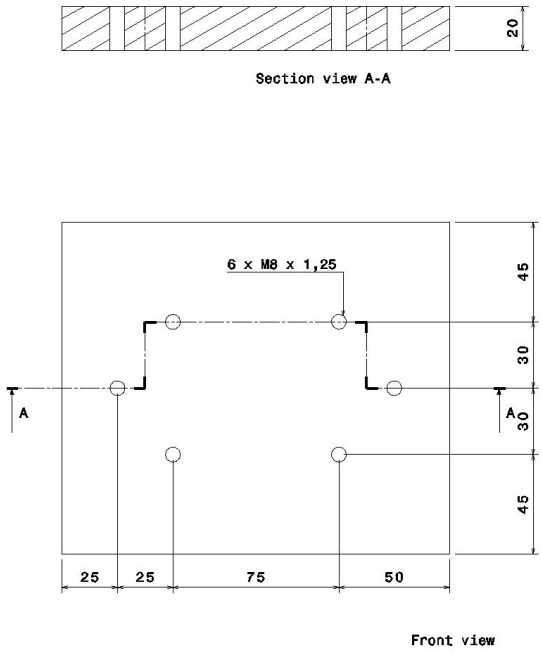

Figure A.5: Plate CAD

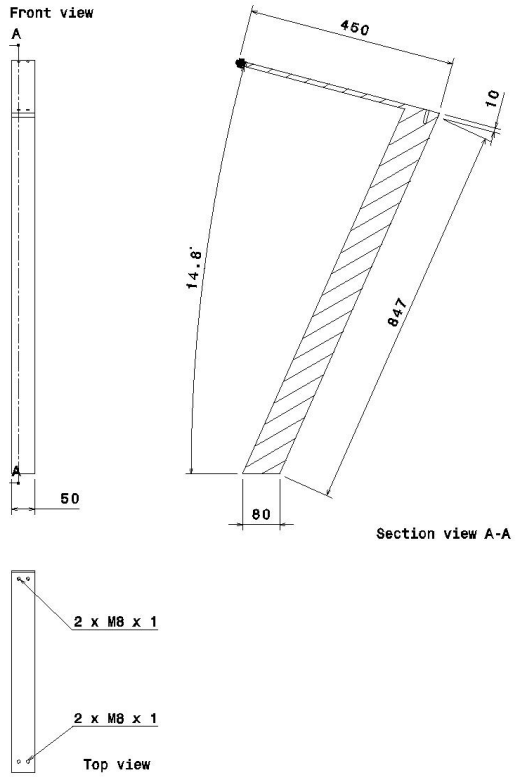

Figure A.6: Sting CAD

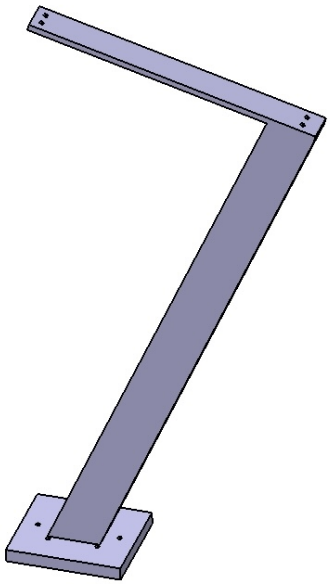

Figure A.7: Sting + Plate CAD

B | Algorithm

Algorithm B.1 Calibration of the transmission ratio $\hat{x}$

Inputs: set of tests $\mathcal{T}$; for each test j: preprocessed sensor angle $\theta_{\mathrm{s},j}(t)$ (after Sec. 5.1.5, a time window $[t_{\mathrm{in},j},\, t_{\mathrm{end},j}]$, and a base angle $B_j \in \{180°,\, 360°\}$. Optional geometric guess x_0.

Per–test increments. For each $j \in \mathcal{T}$:

Compute $\Delta\theta_{\mathrm{s},j} = \theta_{\mathrm{s},j}(t_{\mathrm{end},j}) - \theta_{\mathrm{s},j}(t_{\mathrm{in},j})$; enforce a consistent (positive) rotation direction.

Global robust fit. Build a search grid $\mathcal{X}$ around x_0 (e.g., $\mathcal{X} = [0.8\,x_0,\, 1.2\,x_0]$ with fine step).

for each $x \in \mathcal{X}$ **do**

  for each test j **do**

    Choose the nearest integer number of base turns:

$$k_j(x) \leftarrow \mathrm{round}\left(\frac{x\,\Delta\theta_{\mathrm{s},j}}{B_j}\right).$$

    Residual (overshoot) for test j:

$$e_j(x) \leftarrow x\,\Delta\theta_{\mathrm{s},j} - B_j\,k_j(x).$$

  end for

  Robust cost (Huber loss with threshold δ):

$$J(x) \leftarrow \sum_{j\in\mathcal{T}} \rho_\delta\big(e_j(x)\big), \quad \rho_\delta(e) = \begin{cases} \frac{1}{2}e^2, & |e| \le \delta, \\ \delta(|e| - \frac{1}{2}\delta), & |e| > \delta. \end{cases}$$

end for

Estimate. $\hat{x} \leftarrow \arg\min_{x\in\mathcal{X}} J(x)$.

Reporting. For each j, compute $\alpha_j = \hat{x}\,\Delta\theta_{\mathrm{s},j}$, $\alpha_{j,\mathrm{round}} = B_j\,k_j(\hat{x})$, and overshoot $e_j(\hat{x}) = \alpha_j - \alpha_{j,\mathrm{round}}$. Report $\hat{x}$, $\{k_j(\hat{x})\}$, and overshoot statistics (median, MAD); optionally group by mass.

C | Geometry and Data

Quantity	Value	Unit	Note
Tip radius R	3.50	m	Wing CG radius
Drum radius $r_{\text{drum,inner}}$	0.225	m	Rope on small central disk
Arm length L_{arms}	3.50	m	Tip lever arm
Arm diameter d_{arms}	0.022	m	Circular rod assumption
Wing area S_{wing}	0.50	m^2	Historical wing
Wing mass m_{wing}	0.50	kg	Per wing (two wings total)
$C_{D,\text{rod}}$	1.00	–	Slender cylinder, low-Re estimate
$C_{D,\text{wing}}$	variable	–	Assumed at test α
Cable diameter d_{cable}	0.002	m	Steel cables
$C_{D,\text{cable}}$	1.00	–	Circular cylinder
Air density ρ_{air}	1.18	kg/m^3	Indoor, $\sim 20°\text{C}$

Table C.1: Key constants used in the simulation code

Quantity	Value	Unit	Note
Hanging masses m_1, m_2	variable	kg	Per side
Pulley wrap θ_{wrap}	60	°	On small pulley groove
Friction $\mu_{\text{rope-wood}}$	0.20	–	Capstan factor $k_{\text{cap}} = e^{-\mu\theta}$
Bushing friction μ_{bearing}	0.10	–	Metal–wood estimate
Radius ratio i_{ratio}	1.50	–	$r_{\text{drum,inner}}/r_{\text{pulley,inner}}$

Table C.2: Drive and friction parameters used in the simulation

Inertias — definitions

$$I_{\text{disk}} = \sum_j \tfrac{1}{2}\,\rho_{\text{wood}}\,\pi\,t_j\left(r_{o,j}^4 - r_i^4\right), \tag{C.1}$$

$$I_{\text{shaft}} = \tfrac{1}{2}\,\rho_{\text{Al}}\,\pi\,L_{\text{shaft}}\,\left(r_o^4 - r_i^4\right), \tag{C.2}$$

$$I_{\text{pulley,tot}} = \sum_j \tfrac{1}{2}\,\rho_{\text{wood}}\,\pi\,t_{\text{pul}}\left(r_{o,j}^4 - r_{\text{in}}^4\right), \tag{C.3}$$

$$I_{\text{arms,rad}} = \tfrac{1}{3}\,m_{\text{arm,rad}}\,L_{\text{arms}}^2, \qquad I_{\text{arms,cen}} = m_{\text{arm,ver}}\,d_{\text{cen}}^2 + \tfrac{1}{2}m_{\text{arm,ver}}\,r_{\text{arm}}^2, \tag{C.4}$$

$$I_{\text{arms,end}} = m_{\text{arm,ver}}\,L_{\text{arms}}^2 + \tfrac{1}{2}m_{\text{arm,ver}}\,r_{\text{arm}}^2, \tag{C.5}$$

$$I_{\text{arms,tot}} = 4\,I_{\text{arms,rad}} + 2\,I_{\text{arms,cen}} + 2\,I_{\text{arms,end}}, \tag{C.6}$$

$$I_{\text{wing,tot}} = 2\big(m_{\text{wing}}L_{\text{arms}}^2 + \tfrac{1}{12}m_{\text{wing}}\left(b_{\text{wing}}^2 + c_{\text{wing}}^2\right)\big), \tag{C.7}$$

$$I_{\text{cables}} = \sum_i \rho_{\text{c}}\,A_i\,\gamma_i\,\tfrac{(b_i^3 - a_i^3)}{3}\,n_i, \quad \gamma_i = \sqrt{1 + \left(\tfrac{\Delta z_i}{b_i - a_i}\right)^2}, \tag{C.8}$$

$$J_{\text{masses}} = (m_1 + m_2)\,r_{\text{drum,inner}}^2, \tag{C.9}$$

$$J_{\text{rigid}} = I_{\text{disk}} + I_{\text{shaft}} + I_{\text{arms,tot}} + I_{\text{pulley,tot}}\,i_{\text{ratio}}^2 + I_{\text{wing,tot}} + I_{\text{cables}}, \tag{C.10}$$

$$k_{\text{cap}} = e^{-\mu_{\text{rope-wood}}\theta_{\text{wrap}}}, \quad K_{\text{bush}} = \mu_{\text{bearing}}\,r_{\text{pulley,inner}}\,i_{\text{ratio}}\,C_{\text{wrap}}, \tag{C.11}$$

$$J_{\text{eff}} = J_{\text{rigid}} + k_{\text{cap}}\,J_{\text{masses}} - (m_1 + m_2)\,K_{\text{bush}}\,r_{\text{drum,inner}}. \tag{C.12}$$

Quadratic drag factors — definitions

$$D_{\text{rad}} = \tfrac{1}{8}\,\rho_{\text{air}}\,C_{D,\text{rod}}\,d_{\text{arms}}\,L_{\text{arms}}^4, \tag{C.13}$$

$$D_{\text{cen}} = \tfrac{1}{2}\,\rho_{\text{air}}\,C_{D,\text{rod}}\,d_{\text{arms}}\,h_{\text{arms}}\,d_{\text{cen}}^3, \quad D_{\text{end}} = \tfrac{1}{2}\,\rho_{\text{air}}\,C_{D,\text{rod}}\,d_{\text{arms}}\,h_{\text{arms}}\,L_{\text{arms}}^3, \tag{C.14}$$

$$D_{\text{arms}} = 4\,D_{\text{rad}} + 2\,(D_{\text{cen}} + D_{\text{end}}), \tag{C.15}$$

$$D_{\text{wing,tot}} = \rho_{\text{air}}\,S_{\text{wing}}\,L_{\text{arms}}^3\,C_{D,\text{wing}}, \tag{C.16}$$

$$D_{\text{cables}} = \sum_i \rho_{\text{air}}\,C_{D,\text{cable}}\,d_i\,\gamma_i\,k_i\,\tfrac{(b_i^4 - a_i^4)}{8}\,n_i, \tag{C.17}$$

$$D_{\text{total}} = D_{\text{arms}} + D_{\text{wing,tot}} + D_{\text{cables}}. \tag{C.18}$$

D | Simulation Code

Listing D.1: Whirling-arm ODE with stop at ground

```
function [t, theta, omega, z] = simulate_whirling(tmax, Jhat, Dtot,
    tau_g, r_drum, h)
% SIMULATE_WHIRLING  Minimal whirling-arm ODE (grouped form, start from
    rest).
%
% USAGE:
%   [t, theta, omega, z] = simulate_whirling(tmax, Jhat, Dtot, tau_g,
    r_drum, h)
%
% STATE (returned as vectors sampled at t):
%   t       [s]     time
%   theta   [rad]   rotation angle
%   omega   [rad/s] angular speed
%   z       [m]     remaining drop height (z=0 => masses reach ground)
%
% INPUTS:
%   tmax    [s]     max integration time
%   Jhat    [kg m^2]    effective inertia  \hat{J}
%   Dtot    [N m s^2 / rad^2]  quadratic drag coeff  D_tot
%   tau_g   [N m]     gravity drive torque  \tau_g
%   r_drum  [m]       inner drum radius  r_d
%   h       [m]       initial drop height (z(0)=h)
%
% DYNAMICS (grouped form, no sign changes):
%   theta' = omega
%   omega' = (tau_g - Dtot * omega*|omega|) / Jhat
%   z'     = - r_drum * omega
%
% Starts from rest: theta(0)=0, omega(0)=0, z(0)=h.
% Integration stops when z(t)=0.

x0   = [0; 0; h];    % [theta; omega; z]
rhs  = @(t,x) [ x(2); ...
                (tau_g - Dtot * x(2) * abs(x(2))) / Jhat; ...
```

```
32                -r_drum * x(2) ];
33
34 opts = odeset('Events', @stop_when_ground);
35 [t, X] = ode45(rhs, [0 tmax], x0, opts);
36
37 theta = X(:,1);
38 omega = X(:,2);
39 z     = X(:,3);
40
41   function [value, isterminal, direction] = stop_when_ground(~, x)
42     value = x(3);       % z
43     isterminal = 1;     % stop integration
44     direction  = -1;    % crossing from + to 0
45   end
46 end
```

List of Figures

2.1 Otto Lilienthal portrait, 1894. Photographer: A. Regis. Otto-Lilienthal-Museum Bildarchiv, Archiv-ID 18009 [9] 5
2.2 Lilienthal's Plate IV showing whirling-arm apparatus results [2, Pl. IV] . . 6
2.3 Otto Lilienthal in flight with the *Normalsegelapparat*, Fliegeberg (Berlin–Lichterfelde), 1894. Photo: Alex Krajewsky. Otto-Lilienthal-Museum Bildarchiv, Archiv-ID 12226 [9] 7
2.4 Streamline sketches around a flat plate and a curved surface [2, Fig. 39, Ch. 25] 8
2.5 *Rundlaufapparat* vs. wind apparatus used by Lilienthal to measure lift and drag [2, Fig. 23, Ch. 19; Figs. 54–56, Ch. 23] 9
2.6 Lilienthal's Plates illustrating the wind effect [2, Pls. V–VI] 9
2.7 Otto Lilienthal with the *Normalsegelapparat*, 29 June 1895. Photo: Richard Neuhauss. Otto-Lilienthal-Museum Bildarchiv, Archiv-ID 12134 [9]. 10
2.8 Other inventions associated with Lilienthal's workshop 11
2.9 Drawing of the large *Rundlaufapparat* (diameter 7 m), 1888. Otto-Lilienthal-Museum Bildarchiv, Archiv-ID 00109 [9] 12
2.10 Wright brothers' first powered flight, 17 December 1903, Kitty Hawk. Library of Congress, digital ID LC-DIG-ppprs-00626 [21] 13
2.11 Wright brothers' 1901 wind tunnel (replica). National Museum of the U.S. Air Force [22] 13

3.1 *Rundlaufapparat* 21
3.2 *Rundlaufapparat*: front view (left) and side view (right) 22
3.3 Central drum overview 24
3.4 Pulleys overview 26
3.5 Driving system of the *Rundlaufapparat* 27
3.6 Arm frame assembly 29

3.7 Arms: geometry and cable layout. **(a)** Front view: rectangular arm frame with in-plane cables (red) and out-of-plane cables (blue). **(b)** Top view: cables originate from two steel lugs connected to the shaft center and run to mid-span and tip. 29
3.8 Test wing 30
3.9 Wing shape adopted by Lilienthal in his experiments [2, Fig. 47, Ch. 28] . 30
3.10 Historical airfoil tested by Lilienthal [2, Fig. 48, Ch. 28] 31
3.11 Counterweight lever system 32
3.12 Lift balance 33

4.1 Otto Lilienthal, *Skizze und Berechnungen zu Versuchen am großen Rundlaufapparat* (Sketches and calculations for experiments on the large whirling apparatus), 12 Aug. 1888; pencil and ink on paper, $21.0 \times 33.0\,\mathrm{cm}$; 14 pages (4 bifolia); Otto-Lilienthal-Museum Bildarchiv, Archiv-ID 00119; copy after Deutsches Museum, HS 626, BN 46906 [11] 36
4.2 Apparatus operation and applied torques. Driving torque $\tau_{\mathrm{drive}} = 2\,m\,g\,r$; resisting (drag) torque $\tau_{\mathrm{drag}} = 2\,D\,R$ 38
4.3 Counterbalanced lift lever. Left end: counterweight m_{bal}. Right end: rotating system m_{sys}, added mass in lift balance m_{L} and the two wings that produce lift 44

5.1 Velocity measurement setup 48
5.2 PSC-360 calibration 49
5.3 Sensor angle processing 52
5.4 $V(t)$ for three runs at $(10\,\mathrm{kg}, 12°)$ 53
5.5 $V(t)$ at $\alpha = 0°$ for one representative run at each mass (10, 15, 20 kg) . . . 54
5.6 $V(t)$ at $m = 10\,\mathrm{kg}$ for one representative run at each α (0°, 12°, 30°) 54
5.7 Per-test transmission ratios $x_{\mathrm{tr},j}$ with ideal x_0 and calibrated $\hat{x}$ 55
5.8 Comparison of $V(t)$ reconstructed with ideal x_0 and calibrated $\hat{x}$ 56
5.9 Measured vs. simulated $V(t)$ for four representative cases 61
5.10 Otto Lilienthal, *Meßkurve zum Eigenwiderstand des Rundlaufapparats* (Measurement curve of the inherent resistance of the whirling-arm apparatus), 1874. Pencil on paper, $21.0 \times 33.0\,\mathrm{cm}$; 8 pages. Otto-Lilienthal-Museum Bildarchiv, Archiv-ID 00112; copy after Deutsches Museum, HS 6262, BN 2517. [9] 63
5.11 Arms-only baseline of the whirling-arm apparatus 66
5.12 Effect of driving mass at $\alpha = 0°$ 68
5.13 Comparison with Lilienthal's Plate IV [2] under different normalizations . . 69

5.14 Polars $C_{\mathrm{L}}(\alpha)$ and $C_{\mathrm{D}}(\alpha)$ 70
5.15 Comparison of drag formulations 72
5.16 Uncertainty – polar curve C_{L} vs. C_{D} 77
5.17 Uncertainty – $C_{\mathrm{L}}(\alpha)$ and $C_{\mathrm{D}}(\alpha)$ 77
5.18 Representative time history $V_{\mathrm{sim}}(t)$ with the three scalar metrics: $\overline{V}$, V_{rms}, and V_{max} 79
5.19 Comparison with Lilienthal's results showing the effect of the different velocity bases 80
5.20 Comparison with Lilienthal's results showing the effect of different drum radii 81

6.1 Selected airfoil for wind-tunnel tests and simulations [2, Fig. 52, Ch. 28] . . 83
6.2 Wing model with airfoil highlight at mid-span in CATIA 84
6.3 Half-scale upper-surface mold; eight PLA blocks with mold-release layer applied 85
6.4 Half-scale model for wind-tunnel tests 86
6.5 Wind-tunnel test setup: balance, plate, sting, and wing 87
6.6 Wind-tunnel results over the full angle range, $\alpha \in [-10^\circ, 90^\circ]$ 90
6.7 Wind-tunnel lift-drag polar over the full angle range, $\alpha \in [-10^\circ, 90^\circ]$ 91
6.8 Wind-tunnel results over the optimized angle range, $\alpha \in [-10^\circ, 35^\circ]$ 91
6.9 Wind-tunnel lift-drag polar over the optimized angle range, $\alpha \in [-10^\circ, 35^\circ]$ 92
6.10 Comparison of wind-tunnel results with Lilienthal's data 92

7.1 Two-dimensional grid structure 98
7.2 C_{p} at $\alpha = 0^\circ$ for different $(\mathrm{Ma}, \mathrm{Re})$ showing bubble/separation reduction . 100
7.3 C_{L} and C_{D} at $\alpha = 0^\circ, 5^\circ$ for three turbulence models: SA, k-ω, RSM 101
7.4 Grid convergence assessment in 2D RANS at $\alpha = 0^\circ$ 103
7.5 $|\vec{u}|/U_\infty$ and streamlines at various α 105
7.6 Non-dimensional vorticity $\omega^\star = \omega_y c/U_\infty$ at different α. A diverging blue-red colormap is centered at 0 with symmetric limits $\omega^\star \in [-20, 20]$ 106
7.7 Aerodynamic coefficients from 2D RANS over the full angle range $\alpha \in [-15^\circ, 90^\circ]$ at $\mathrm{Re} = 3.25 \times 10^5$, $\mathrm{Ma} = 0.035$ 108
7.8 Aerodynamic coefficients in the classical pre-stall range $\alpha \in [-15^\circ, 15^\circ]$ . . 109
7.9 Three-dimensional grid structure 110
7.10 Pressure coefficient C_{p} on the wing with streamtraces at $\alpha = 7^\circ$ 111
7.11 Aerodynamic coefficients from 3D RANS simulations 112
7.12 3D simulations and *Rundlaufapparat* tests compared with Lilienthal's results via Smeaton normalization ($D = k\,S\,V^2$, $k = 0.13$) 113

7.13 Comparison of 3D simulations and modern *Rundlaufapparat* tests using classical aerodynamic coefficients 113
7.14 Global lift-drag polar: modern whirling-arm tests, wind-tunnel tests, and 3D RANS overlaid on Lilienthal's Plate IV (Smeaton normalization $D = kSV^2$, $k = 0.13$) 114

A.1 Drum CAD 125
A.2 Pulley CAD 125
A.3 Flanged spigot adapter CAD 126
A.4 Sensor disk CAD 126
A.5 Plate CAD 127
A.6 Sting CAD 127
A.7 Sting + Plate CAD 127

List of Tables

2.1 Representative values of the Smeaton coefficient k and of the modern normalization $\frac{1}{2}\rho$ 19

3.1 Structural component index 23

4.1 Symbols used in the measurement model 35

5.1 Mean results per driving mass at $\alpha = 0°$ 67
5.2 Input quantities and distributions for uncertainty propagation 74

7.1 Sensitivity to Ma and Re at $\alpha = 0°$ 99

C.1 Key constants used in the simulation code 131
C.2 Drive and friction parameters used in the simulation 131

List of Symbols

Variable	Description	Unit
A	Axial force	N
AR	Aspect ratio (wing)	–
a, a_∞	Speed of sound; freestream value	$\mathrm{m\,s^{-1}}$
B	Commanded base rotation per drop	$^\circ$
Δ_{BL}	Total BL-stack thickness	m
b	Span (wing)	m
C_{A}	Axial-force coefficient	–
C_{D}	Drag coefficient	–
$C_{\mathrm{D},90^\circ}$	Drag coefficient at 90°	–
C_f	Skin-friction coefficient	–
C_{L}	Lift coefficient	–
C_{L_α}	Lift-curve slope	$\mathrm{rad^{-1}}$
C_{M}, $C_{\mathrm{M},y}$	Pitching-moment coefficients: generic; about spanwise axis y (nose-up positive)	–
C_{N}	Normal-force coefficient	–
C_p	Pressure coefficient	–
C_{wrap}	Wrap-geometry factor	–
c, c_{ref}	Chord length; reference chord (3D runs)	m
c_ℓ, c_d	Section lift / drag coefficients	–
D	Drag	N
D'	Drag per unit span	$\mathrm{N\,m^{-1}}$
D_{tot}	Total drag-torque factor	$\mathrm{N\,m\,s^2}$
D_{wing}	Wing contribution to drag-torque factor	$\mathrm{N\,m\,s^2}$
d	Diameter	m

Continued on next page

Variable	Description	Unit
d_0	Drum diameter (Lilienthal case)	m
e	Oswald efficiency factor	–
e_v, e_s	Water-vapour partial and saturation pressure	Pa
F	Force	N
f	Calibration gain	–
g	Gravitational acceleration	$\mathrm{m\,s^{-2}}$
g_BL	Boundary-layer growth factor (BL stack)	–
h	Drop height of the driving weights	m
I	Component inertia	$\mathrm{kg\,m^2}$
i_ratio	Radius ratio, drum over pulley	–
J	Effective inertia (system)	$\mathrm{kg\,m^2}$
k, k_meas, k_mod	Smeaton coefficient: nominal; measured (from 90° runs); modernized value	$\mathrm{N\,m^{-2}\,(m/s)^{-2}}$
k_cap	Capstan attenuation factor	–
k_turb	Turbulent kinetic energy (turbulence models)	$\mathrm{m^2\,s^{-2}}$
L	Lift	N
L'	Lift per unit span	$\mathrm{N\,m^{-1}}$
L_arm	Length of the arms	m
ℓ	Characteristic length	m
ℓ_tr	Transverse-rod length	m
M	Pitching moment	$\mathrm{N\,m}$
Ma	Mach number	–
m	Hanging mass	kg
m'	Empty-run mass yielding V_w	kg
m_f	Friction-equivalent mass (Coulomb equivalent)	kg
$m_\mathrm{eq,empty}$	Tip-equivalent empty mass, $m'(r/R)$	kg
N	Normal force	N
N_BL	Number of boundary-layer layers	–
N_nodes	Total grid nodes (mesh size)	–
n, n_0	Number of turns; reference number of turns (Lilienthal case)	–

Continued on next page

Variable	Description	Unit
n_{pulley}	Number of pulleys/sides	–
p, p_t, p_∞	Static, total, and freestream pressure	Pa
q	Dynamic pressure	Pa
R	Apparatus rotational radius	m
R_d, R_v	Gas constants (dry air, water vapour)	$\mathrm{J\,kg^{-1}\,K^{-1}}$
Re	Reynolds number	–
RH	Relative humidity	%
r	Radial coordinate / radius	m
r_{drum}	Drive-drum winding radius	m
r_{lev}	Lift-lever arm (each side)	m
r_0	Drum radius (Lilienthal case)	m
S	Reference area	$\mathrm{m^2}$
$\overline{S}_{ij}$	Mean strain-rate tensor	$\mathrm{s^{-1}}$
s_{eq}	Equivalent slip	–
T, T_∞, T_c	Absolute / freestream temperature; air temperature (Celsius)	K / °C
T_{in}, T_{out}	Rope tension at pulley inlet / outlet	N
t	Thickness	m
t_{a}	Time for n turns (empty / arms only)	s
t_{in}, t_{end}	Start / end time of traction window	s
t_{inner}, t_{outer}	Inner / outer disk thickness	m
t_{w}	Time for n turns with wings	s
U_∞	Wind-tunnel freestream speed	$\mathrm{m\,s^{-1}}$
$u(\,\cdot\,)$	Standard uncertainty of a quantity	$[\,\cdot\,]$
$\overline{u}_i$	Reynolds-averaged velocity component	$\mathrm{m\,s^{-1}}$
$\vec{u}$	Velocity vector in the airfoil plane	$\mathrm{m\,s^{-1}}$
u_i'	Fluctuating velocity component	$\mathrm{m\,s^{-1}}$
u_τ	Friction velocity	$\mathrm{m\,s^{-1}}$
V	Speed (magnitude)	$\mathrm{m\,s^{-1}}$
$\overline{V}$	Mean speed over the drop window	$\mathrm{m\,s^{-1}}$
V_{a}	Tip speed in empty (arms-only) run with m	$\mathrm{m\,s^{-1}}$

Continued on next page

Variable	Description	Unit
$V_{\max}$	Maximum speed during the window	$\mathrm{m\,s^{-1}}$
V_{rms}	Root-mean-square speed over the window	$\mathrm{m\,s^{-1}}$
V_{sig}, V_{ref}	Sensor output and reference voltages	V
V_{w}	Tip speed in wings-on paired run	$\mathrm{m\,s^{-1}}$
w	Camber height (max rise of surface above chord)	m
x_0, x_{tr}, $\hat{x}$	Transmission ratio: ideal; measured (per test); calibrated global	–
y	Spanwise coordinate	m
y^+	Wall-unit coordinate $y\,u_\tau/\nu$	–
Δy_1	First wall-normal cell height (BL stack)	m
z	Vertical coordinate	m
z_{drop}	Remaining drop height (state variable)	m
α	Angle of attack	rad / °
α_{bal}, α_{wing}	Balance angle; chord-based wing angle	rad / °
$\alpha_{\mathrm{L=0}}$	Zero-lift angle	rad / °
δ_{ij}	Kronecker delta	–
γ	Ratio of specific heats	–
η	Voltage ratio	–
θ, $\theta_{\max}$	Rotational angle; maximum angular excursion	rad / °
θ_{wrap}	Rope wrap angle on pulley	rad
μ, μ_t	Dynamic and turbulent dynamic viscosity	$\mathrm{Pa\,s}$
μ_{b}, μ_{rope}	Dry-friction coefficient (bushing); rope–pulley friction coefficient	–
ν, ν_t, ν_∞	Kinematic viscosity; turbulent kinematic viscosity; freestream value	$\mathrm{m^2\,s^{-1}}$
ρ, ρ_∞	Density; freestream density	$\mathrm{kg\,m^{-3}}$
τ_c	Time constant of closed form	s
τ_{drive}, τ_{drag}, τ_{friction}, τ_g	Drive torque; aerodynamic resisting torque; equivalent resisting torque (friction); gravity drive torque	$\mathrm{N\,m}$
ω, ω_∞	Angular speed; asymptotic angular speed	$\mathrm{rad\,s^{-1}}$
ω_y	Vorticity component normal to the section plane	$\mathrm{s^{-1}}$
$\omega^\star$	Non-dimensional vorticity	–